International journal
for science, technics and
innovations for the industry

# MTM
# MACHINES TECHNOLOGIES MATERIALS

ISSN PRINT 1313-0226
ISSN WEB 1314-507X
Issue 7 / 2018
YEAR XII

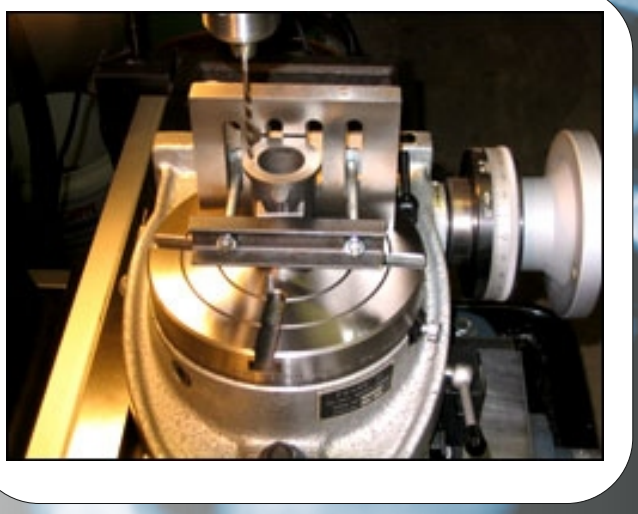

Published by
Scientific technical
Union of Mechanical Engineering

# MACHINES. TECHNOLOGIES. MATERIALS

## INTERNATIONAL SCIENTIFIC JOURNAL

PUBLISHER

**SCIENTIFIC TECHNICAL UNION OF MECHANICAL ENGINEERING "INDUSTRY 4.0"**

108, Rakovski Str., 1000 Sofia, Bulgaria
tel. (+359 2) 987 72 90,
tel./fax (+359 2) 986 22 40,
office@stumejournals.com
www.stumejournals.com

**ISSN PRINT 1313-0226, ISSN WEB 1314-507X, YEAR XII, ISSUE 7 / 2018**



### EDITOR-IN-CHIEF

**Prof. D.Sc. DHC Georgi Popov**,
President of Bulgarian Scientific and Technical Union of Mechanical Engineering

### EDITORIAL BOARD

| MEMBERS | SCIENTIFIC COMPETENCE |
|---|---|
| Prof. Dimitar Damyanov | Automatisation of production |
| Prof. Dimitar Karaivanov | Mechanics of machines |
| Prof. Dimitar Stavrev | Technologies and materials |
| Prof. Dimitar Yonchev | National and industrial security |
| Prof. Galina Nikolcheva | Machines tools and technologies |
| Prof. Hristo Shehtov | Automatisation of production |
| Prof. Idilija Bachkova | Automatisation of production |
| Prof. Ivan Kralov | Mechanics of machines |
| Prof. Ivan Parshorov | Technologies and materials |
| Prof. Ivan Yanchev | Machines and technologies |
| Prof. Ivo Malakov | Automatisation of production |
| Prof. Kiril Angelov | Industrial Management |
| Prof. Lilo Kunchev | Transport Equipment and Technology |
| Prof. Lubomir Dimitrov | Machines and technologies |
| Prof. Miho Mihov | Agricultural machinery |
| Prof. Miroslav Denchev | Ergonomics and design |
| Prof. Mladen Velev | Economics and Marketing |
| Prof. Nikolay Diulgerov | Technologies and materials |
| Prof. Ognyan Andreev | Production management |
| Prof. Petar Kolev | Transport Equipment and Technology |
| Prof. Roman Zahariev | Robotics |
| Prof. Sasho Guergov | Robotic systems and technology |
| Prof. Tsanka Dikova | Technologies and materials |
| Prof. Vitan Galabov | Mechanics of machines |

# MACHINES. TECHNOLOGIES. MATERIALS

## INTERNATIONAL SCIENTIFIC JOURNAL

**ISSN PRINT 1313-0226, ISSN WEB 1314-507X, YEAR XII, ISSUE 7 / 2018**



| EDITORIAL BOARD FOREIGN MEMBERS | | | |
|---|---|---|---|
| Prof. Adel Mahmoud | IQ | Prof. Marian Tolnay | SK |
| Prof. Ahmet Ertas | TR | Prof. Mark Easton | AU |
| Prof. Andonaq Londo | AL | Prof. Mart Tamre | EE |
| Prof. Andrei Firsov | RU | Prof. Maryam Ehteshamzade | IR |
| Prof. Andrzej Golabczak | PL | Prof. Michael Evan Goodsite | DK |
| Prof. Anita Jansone | LV | Prof. Mihail Aurel Titu | RO |
| Prof. Aude Billard | CH | Prof. Movlazade Vagif Zahid | AZ |
| Prof. Bojan Dolšak | SI | Prof. Natasa Naprstkova | CZ |
| Prof. Christian Marxt | LI | Prof. Oana Dodun | RO |
| Prof. Dale Carnegie | NZ | Prof. Oleg Sharkov | RU |
| Prof. Emilia Abadjieva | BG | Prof. Páll Jensson | IS |
| Prof. Ernest Nazarian | AM | Prof. Patrick Anderson | NL |
| Prof. Esam Husein | KW | Prof. Paul Heuschling | LU |
| Prof. Ewa Gunnarsson | SW | Prof. Pavel Kovac | RS |
| Prof. Filipe Samuel Silva | PT | Prof. Per Skjerpe | NO |
| Prof. Francisco Martinez Perez | CU | Prof. Péter Korondi | HU |
| Prof. Franz Haas | AT | Prof. Peter Kostal | SK |
| Prof. Genadii Bagliuk | UA | Prof. Juan Alberto Montano | MX |
| Prof. Georg Frey | DE | Prof. Raul Turmanidze | GE |
| Prof. Gregory Gurevich | IL | Prof. Renato Goulart | BR |
| Prof. Haydar Odinaev | TJ | Prof. Roumen Petrov | BE |
| Prof. Hiroyuki Moriyama | JP | Prof. Rubén Darío Vásquez Salazar | CO |
| Prof. Dr. Ilir Doci | Ko | Prof. Safet Isić | BA |
| Prof. Iryna Charniak | BY | Prof. Sean Leen | IE |
| Prof. Ivan Svarc | CZ | Prof. ShI Xiaowei | CN |
| Prof. Ivica Veza | HR | Prof. Shoirdzan Karimov | UZ |
| Prof. Jae-Young Kim | KR | Prof. Sreten Savićević | ME |
| Prof. Jerzy Jedzejewski | PL | Prof. Stefan Dimov | UK |
| Prof. Jean-Emmanuel Broquin | FR | Prof. Svetlana Gubenko | UA |
| Prof. Jordi Romeu Garbi | ES | Prof. Sveto Cvetkovski | MK |
| Prof. Jukka Tuhkuri | FI | Prof. Tamaz Megrelidze | GE |
| Prof. Katia Vutova | BG | Prof. Tashtanbay Sartov | KG |
| Prof. Kazimieras Juzėnas | LT | Prof. Teimuraz Kochadze | GE |
| Prof. Krasimir Marchev | USA | Prof. Thorsten Schmidt | DE |
| Prof. Krzysztof Rokosz | PL | Prof. Tonci Mikac | HR |
| Prof. Leon Kukielka | PL | Prof. Vasile Cartofeanu | MD |
| Prof. Mahmoud El Gammal | EG | Prof. Yasar Pancar | TR |
| Prof. Manolakos Dimitrios | GR | Prof. Yurij Kuznetsov | UA |
| Prof. Marat Ibatov | KZ | Prof. Wei Hua Ho | ZA |
| Prof. Marco Bocciolone | IT | Prof. Wu Kaiming | CN |

# C O N T E N T S

## MACHINES

**PRINTING PARAMETERS EFFECT ON SURFACE CHARACTERISTICS OF 3D PRINTED PLA MATERIALS**
Kovan V., Tezel T., Topal E.S., Camurlu H.E. ..... 266

**REFINING THE PROCESS OF DESIGNING AN ELECTRICAL RESISTANCE HEATER FOR VACUUM FURNACE IN NON-STATIONARY PROCESS**
PhD E. Angelova ..... 270

## TECHNOLOGIES

**DEVELOPMENT AND IMPROVEMENT OF TECHNOLOGIES FOR PRODUCING STRUCTURAL MATERIALS WITH ULTRAFINE-GRAINED STRUCTURE BY SEVERE PLASTIC DEFORMATION**
c.t.s., associate professor Lezhnev S.; d.t.s., professor Naizabekov A.; PhD Panin E., PhD Arbuz A. ..... 273

**DESIGN AND ANALYTICAL APPROACH TO UNIFORM MATERIAL STRUCTURE OF INJECTION MOLDING PARTS**
Berenika Hausnerová, Jakub Huba ..... 277

**TO THE PROBLEMS OF FLUORESCENCE EXCITATION SPECTRUMS**
Prof. Gomidze N., M.Sc. of Radio-Physics Shainidze J., M.Sc. of Radio-Physics Shengelia G. PhD. Student of Physics Turmanidze R. ... 279

**WIND POTENTIAL ANALYSIS FOR HAKKARI CENTRAL REGION**
Emrah Harmanci, Sedat Yayla ..... 283

## MATERIALS

**PRODUCTION PROCESS OF POWDER PERMEABLE MATERIALS MADE OF SPHERICAL BRONZE POWDERS BY PRESSING**
Prof., Dr. Eng., Cor. Member of NAS of Belarus Ilyushchanka A., PhD of Eng., Doc. Kusin R.A., Head of the Lab. Charniak I.N., Res. Kusin A.R., Res. Zhehzdryn D.I. ..... 287

**INVESTIGATION OF HARDENING PROCESSES OF CORROSION-RESISTANT COATINGS DEPOSITED BY A FLUX-CORED WIRE WITH NITRIDE-BORIDE ALLOYING**
Prof. Dr. Econ. Kuznetsova O., Prof. Dr. Eng. Eremin E., Cand. Eng. Makarov V., graduate student Losev A., graduate student Borodihin S. ..... 291

**REGULARITIES OF ELECTRON-BEAM TECHNOLOGY INFLUENCE ON OPERATING CHARACTERISTICS OF OPTICAL ELEMENTS WITH NANO-DIMENSIONAL OXIDE COATINGS**
DScTech, Yatcenko I. V. ..... 294

**INVESTIGATION OF THE EFFECT OF DIAMETERS OF POLYACRYLONITRILE NANO FIBER WITH CARBON NANOTUBE ON MECHANICAL PROPERTIES**
Assist.Prof.Dr..Gürol Ö., Assoc.Prof.Dr..Kevser D. ..... 298

**TUNGSTEN AND MOLYBDENUM CARBIDES OBTAINING BY ELECTROLYSIS OF SALT MELTS**
Prof., D.Sc. Malyshev V., Prof., D.Sc. Kushchevska N., Prof., D.Sc. Bagliuk G., Ph.Dr. Shakhnin D., Ph.Dr. Paprotskaya O., M.Sc. Kurovskyi V. ..... 302

# PRINTING PARAMETERS EFFECT ON SURFACE CHARACTERISTICS OF 3D PRINTED PLA MATERIALS

Kovan V., Tezel T., Topal E.S., Camurlu H.E.
Department of Mechanical Engineering, Engineering Faculty - Akdeniz University, Turkey

kovan@akdeniz.edu.tr, tugcetezel@akdeniz.edu.tr, estopal@akdeniz.edu.tr, ecamurlu@akdeniz.edu.tr

***Abstract:*** *Three-dimensional (3D) printing technologies are the most promising method in the production of functional parts. Although 3D printing technology includes various methods, fused deposition modelling (FDM) is the most widely used one. In FDM, generally polylactic acid (PLA) filaments are used to fabricate 3D geometry by stacking individual layers. In fact, FDM is a complicated process with numerous parameters that affect printing quality. Printing parameters such as printing orientation, layer thickness, printing orientation angle, filling ratio, filament feed rate, etc. have significant impact on the quality and performance of FDM printed parts. Since the mechanical properties are very important for functional parts, the effect of these parameters on the mechanical properties of the PLA specimens has been extensively studied. However, there is no sufficient data in the surface characterization literature of these parameters. In this study, the effect of layer thickness and printing temperature on the surface properties of PLA specimens printed using FDM was investigated.*

**Keywords**: PLA, FDM, 3D PRINTING, SURFACE CHARACTERISTIC

## *1. Introduction*

Surface roughness or roughness is a surface component that can be measured with deviations in the normal direction of an actual surface. If these deviations are large, the surface is rough; if it is small, the surface is characterized as smooth. Roughness determines the performance of the part because it plays a significant role in determining how the parts interact with the environment. Another important issue is that the roughness on the surface forms the starting regions for the cracks.

In terms of the surfaces of the engineering materials, roughness is thought to be detrimental to the performance of the part. In tribology, rough surfaces commonly have higher friction coefficients than smooth surfaces and wear faster. For this reason, the surface structure is closely related to the friction and wear properties of the surface. Adjusting the roughness values during manufacture can be difficult and expensive. Thus, manufacturing at roughly controllable level may be desirable. For example, a glossy surface may come shiny and be slippery to the finger (TouchPad). For this reason, a controlled roughness is required. Otherwise, controlled roughness may be required. For instance, the controlled roughness has the effect of improving the adhesion strength.

Kovan et al. pointed out that the strength of the adhesive bond connection between the 3D printed parts is affected by the surface roughness. It has been determined that layer thickness and printing orientation in 3D printed parts have significant effects on adhesion strength. In the case of low layer thicknesses, the layer produced on the side edge has the highest adhesive strength, whereas in the high layer thickness, the horizontal layer has the highest adhesive strength [1]. Another example is the cylinder bore where the minimum roughness is required so that the oil can be held on the surface.

Three-dimensional printing is a production method that uses only digital technology to produce pieces, as opposed to machining methods such as turning, milling, drilling, etc., in which the material is cut out. Although the focus of 3D printing technologies has been developed primarily for prototype purposes, it has become possible to fabricate metallic structures, artificial bones and a much wider variety of functional parts, with increased emphasis on mechanical properties [2, 3]. PLA is the most widely used material and Fused Deposition Modelling (FDM) is the most widely used technology in this production method which is also called additive manufacturing. FDM has many advantages, such as the use of cheap materials, the lack of expensive equipment, and the ability to create complex geometry. However, FDM has limitations, such as roughness on the surfaces. Methods that will remove these constraints and achieve better surface quality have been studied by many researchers.

Ko and Lee designed a 5-axis machine tool that can make the final cut to improve the low surface quality caused by the 3d printing method. Thus, it has been verified that the surface roughness of the manufactured work pieces can be improved by the final cut [4].

Griguras and Kramar examined the hybrid production process of 3D printing and milling. To enhance the surface quality of the part, the outer surface of the parts produced by 3D printing is milled. Optimization of the technological parameters of hybrid production is made according to minimum production time, minimum surface roughness and minimum material usage. By using a larger nozzle size, the production time is shortened and obtained the same surface quality. [5].

Dewey and Ulutan researched the use of $CO_2$ laser polishing as an adjunct post-treatment to FDM-produced PLA parts to improve the surface features of the products. In their study, instead of reducing the layer thickness in 3D printing, the total processing time could be reduced without sacrificing surface quality. In addition, larger layer thicknesses and lasers have shown that the surface could be processed rapidly [6].

Maidin et al. have tried to improve the surface characteristics of the FDM specimen by applying ultrasonic vibration in their work. As a result of the study, it was found that the best surface quality was obtained with a 21 kHz frequency applied during FDM production [7].

These hybrid processes, which combine machining, laser and ultrasonic processes with FDM processes, result in better surface quality. However, in all of these methods, machinery and production costs significantly increase. For this reason, the effect of the printing parameters on the surface properties of the different printing parameters has been investigated by many researchers, as it is known that the printing parameters affect the surface properties of the 3D printed parts.

Chaidas et al. searched the surface roughness of PLA models fabricated by 3D printing technique. It is found that surface roughness decreased with increasing material melting temperature [8].

In You's study, aimed to optimize the printing parameters of the PLA material used in the 3D printer. In the study, the printing temperature, printing speed and infill ratio were examined at 195-215 °C, 10-70 mm/s and 10-100%, respectively. It was reported that the print quality is the same at almost every printing temperature. In addition, it was determined that the surface roughness is directly proportional to the printing speed and inversely proportional to the infill ratio. [9].

Buj-Corral et al. produced implants with a 3D printer using PLA, a biocompatible polymer, for both prosthetic and support applications. In their studies examining the effect of implant supports and pressure variables, it was stated that the support structure is the main parameter affecting the roughness parameters of the solubility. In order to obtain low roughness values, it is recommended to select a high support structure [10].

Ramli et al. investigated the surface roughness and accuracy of open-source 3D printers, named Mendel Max and Kossel Mini. Spherical, cubical and cylindrical models were produced from PLA and ABS materials using different layer thicknesses and filling ratios on both machines. As a result, when the surface qualities of the models obtained in both machines were compared, it was determined that the surface quality of PLA is better than ABS. In addition, it was reported that the surface properties were better when the layer thickness was 0.178 and the infill ratio was 20% [11].

Valerga et al. stated that 3D printing has some limiting characteristics, and that one of them has a surface quality of the product. In their work, they examined two important production parameters, the effect of printing speed and the extrusion temperature on the surface quality. As a result of this study, it was found that the increment in extrusion temperature of PLA leads to poor surface quality, but the increasing in printing speed improves the surface features [12].

Altan et al. researched the effects of 3D printing parameters on surface roughness and tensile strength. PLA samples are manufactured at different layer thicknesses, printing temperatures and printing speeds. It has been found that the most effective parameters affecting surface roughness are layer thickness and print speed. As the layer thickness decreases, lower surface roughness values are obtained [13].

Hafsa et al. carried out the dimensional accuracy and surface roughness of precision casting models of ABS and PLA produced by 3d printers with different layer thicknesses. The results show that the surface quality of the ABS model produced by reducing the layer thickness is better than the other models. In addition, it has been reported that PLA models give a greater cast model product and the surface quality enhances with increasing layer thickness [14].

These studies exhibit the difference in the outcomes attained by using various printing parameters. The investigations reveal that the surface properties of FDM-fabricated parts are inferior to those of injection moulded parts. 3D printing parameters that will enhance the surface qualities of FDM-manufactured parts is expected to be very useful in engineering applications.

According to our literature research, there is no scientific study which shows the relationship between the printing parameters of the parts produced by FDM and the surface roughness, taking into account the printing layer thickness and extrusion temperature. In this work, PLA samples were manufactured using fused deposition technique (FDM). The influence of the extruder temperature and the layer thickness on the surface roughness were investigated depending on the printing orientation.

## *2. Material and Methods*

In the FDM production technique, the most commonly used filament material is PLA, which is a biopolymer. Environmentally and user-friendly, this material is derived from organic materials such as corn, sugar. These properties, as well as their mechanical properties, make it widely preferred in FDM systems.

In this work, surface roughness measurement specimens were manufactured using a Zmorph printer with PLA material of 1.75 mm diameter produced by Frosch. The 3D printer is capable of producing a model with dimensions of 250x235x165 mm with a positioning accuracy of 14 µm for X and Y axes and 0,625 µm for Z axis.

Three different layer thicknesses (0.1 mm, 0.2 mm and 0.4 mm) and three different printing temperatures (190 °C, 210 °C and 230 °C) were used in the production of test samples. With specially prepared 3D printing codes, for all samples; 3 shells were used around the sample and on the upper and lower surface, and the inside of the sample was printed using the specified printing angles (-45°/+45°) and 35% infill ratio. The PLA material was extruded at a speed of 60 mm/s onto a 65 °C heated printing bed. In Figure 1, different printing orientations are shown according to ASTM F2921 terminology. In this study, all samples were manufactured in the same printing orientation (upright position). However, investigating the effect of other printing orientations (flatwise and edgewise) on surface roughness will be extremely useful for engineering applications.

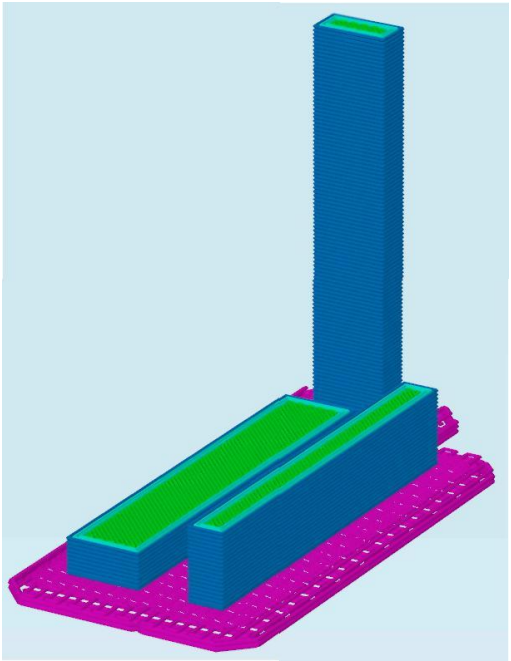

***Fig. 1.*** *Three different printing orientation (flatwise, edgewise and upright) according to ASTM F2921 terminology*

In surface roughness measurements, a profilometer (MahrSurf PS-10, MAHR) was used. Measured parameters for surface roughness evaluation included Ra, Rz and RSm. The measurement results were displayed on an LCD screen and recorded on the computer.

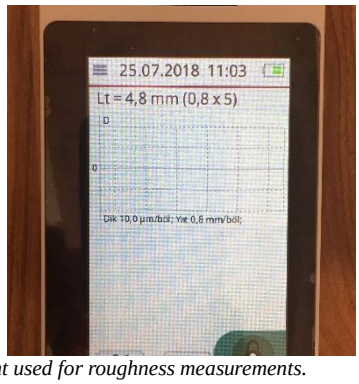


***Fig. 2.*** *Equipment used for roughness measurements.*

## *3. Results and Discussion*

Production time with 3D printer differs according to FDM machines and printing parameters such as layer thickness. Also, depending on the size of printed part, the printing time varies considerably. The effect of the layer thickness can be seen as great

surface feature and resolution after the printing process, but a significant increment in the manufacturing time is observed by decreasing layer thickness. The mean values of the production time of the test samples in this study are 70 min for a layer thickness of 0.1 mm, 40 min for a layer thickness of 0.2 mm and 23 min for a layer thickness of 0.4 mm. Despite the decreasing layer thickness with notable rising in printing time, the changing of printing temperature does not cause a considerable variation in the required printing time.

Optical images of specimens with different layer thickness for 210 °C are shown Figure 3. For the optical results of samples with different layer thicknesses, the peripheral prints are more visible and distinctive at a layer thickness of 0.4 mm. The gaps between the scan and the surrounding prints appear to be the smallest when 0.1mm layer thickness is used. At 0.1 mm layer, the extruder of the FDM creates a more compact scan because it covers less geometric area. Hence, very small gaps occur between the scans or no gaps occur.

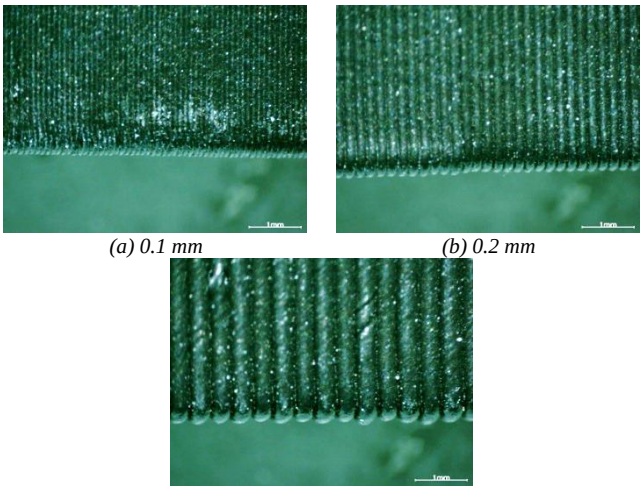

*(a) 0.1 mm* *(b) 0.2 mm*

*(c) 0.4 mm*

***Fig. 3.*** *Optical images of specimens with different layer thickness for 210 °C*

The surface roughness of the samples with different layer thicknesses printed in the upright printing direction is exhibited in Figure 4. As can be seen, in the layer thickness of 0.1 mm, there is almost no effect on the surface roughness of the printing temperature. With increasing layer thickness, the surface roughness values build up at all printing temperatures. In addition, the lowest surface roughness value at a layer thickness of 0.4 mm is obtained at a printing temperature 210 °C. The highest surface roughness values at both 0.2 mm and 0.4 mm layer thicknesses are obtained from samples printed at 230 °C.

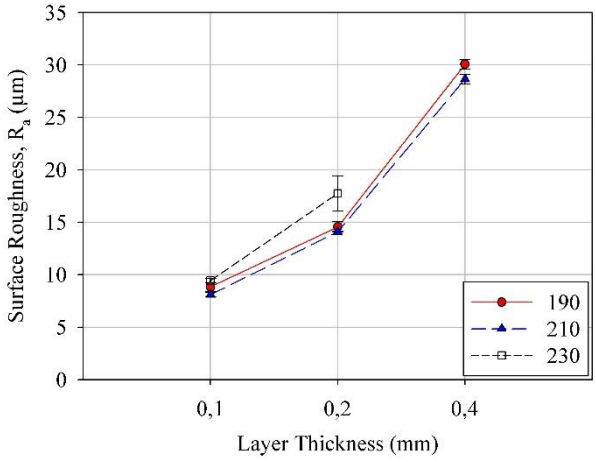


***Fig. 4.*** *Surface roughness for different layer thickness*

Figure 5 presents the surface roughness of samples with different printing temperatures printed in the upright printing orientation. Similar to Figure 4, the effect of the printing temperatures on the surface roughness at all layer thicknesses is quite low. With increasing layer thickness, the surface roughness values rise at all printing temperatures. The best surface quality was acquired at a 210 °C printing temperature and a layer thickness of 0.2 mm. The worst surface properties were obtained from samples having 0.2 mm and 0.4 mm layer thicknesses and which were printed at 230 ° C extrusion temperature.

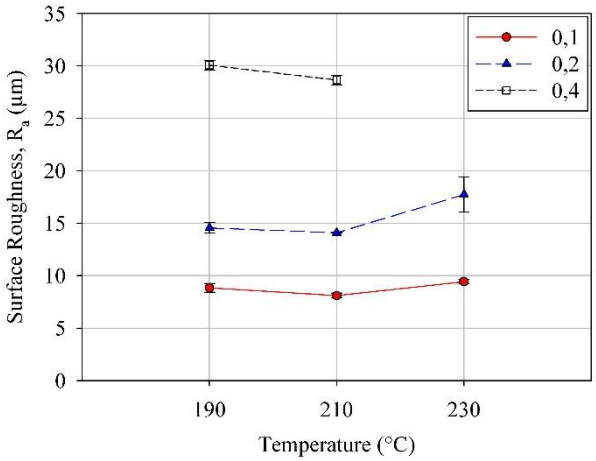


***Fig. 5.*** *Surface roughness for different printing temperatures*

The surface profiles of samples with a 210 °C printing temperature with different layer thicknesses are illustrated in Figure 6. As can clearly be seen, there are significant differences between the surface roughness profiles and values obtained with varying layer thicknesses. The effect of the layer thickness can be clearly understood from the behaviour of the surface profile.

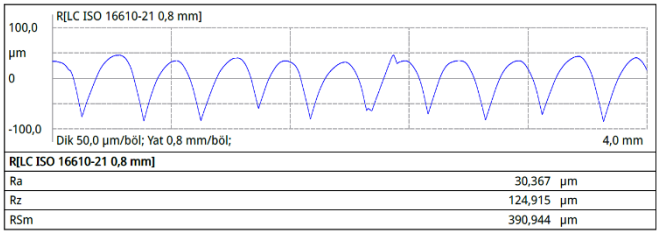


| R[LC ISO 16610-21 0,8 mm] | |
|---|---|
| Ra | 30,367 µm |
| Rz | 124,915 µm |
| RSm | 390,944 µm |

*(a) 0.4 mm*

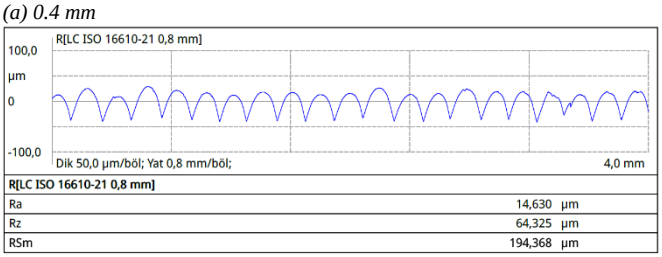


| R[LC ISO 16610-21 0,8 mm] | |
|---|---|
| Ra | 14,630 µm |
| Rz | 64,325 µm |
| RSm | 194,368 µm |

*(b) 0.2 mm*

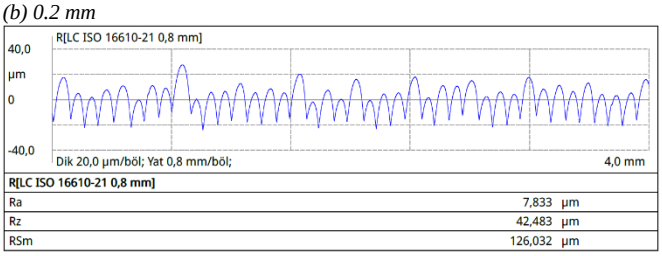


| R[LC ISO 16610-21 0,8 mm] | |
|---|---|
| Ra | 7,833 µm |
| Rz | 42,483 µm |
| RSm | 126,032 µm |

*(c) 0.1 mm*

***Fig. 6.*** *Surface profiles for different layer thickness at 210 °C*

## *4. Conclusions*

The effect of the surface roughness on layer thickness and printing temperature of PLA samples fabricated with FDM was studied. The results showed that the printing parameters have a very important role in surface roughness. Increasing layer thickness at printing temperatures in upright printing direction increases surface roughness values. Between printing temperatures, a lower printing temperature gives a better surface quality.

The application of various printing parameters for different materials will contribute to the development of engineering designs. In this way, the surface characteristics of the parts produced by 3D printers will be better understood.

## *5. Acknowledgment*

This work was supported by The Scientific Research Projects Coordination Unit of Akdeniz University. Project Number: FBA-2018-3470.

## *6. References*

[1] Kovan, V., Altan, G., Topal, E.S. Effect of layer thickness and print orientation on strength of 3D printed and adhesively bonded single lap joints (2017) Journal of Mechanical Science and Technology, 31 (5), pp. 2197-2201.

[2] Murr, L.E., Gaytan, S.M., Medina, F., Martinez, E., Martinez, J.L., Hernandez, D.H., Wicker, R.B. Characterization of Ti–6Al–4V open cellular foams fabricated by additive manufacturing using electron beam melting, (2010) Materials Science and Engineering A, 527(7), pp. 1861-1868.

[3] Vayre, B., Vignat, F., Villeneuve, F. Designing for Additive Manufacturing, Proceedings of the "45th CIRP Conference on Manufacturing Systems", Athens, 16-18.05.2012, University of Patras, Greece, 2012, p. 632-637.

[4] Ko, S., Lee, D. Stiffness optimization of 5-axis machine tool for improving surface roughness of 3D printed products (2017) Journal of Mechanical Science and Technology, 31 (7), pp. 3355-3369.

[5] Grguraš, D., Kramar, D. Optimization of hybrid manufacturing for surface quality, material consumption and productivity improvement (2017) Strojniski Vestnik/Journal of Mechanical Engineering, 63 (10), pp. 567-576.

[6] Dewey, M.P., Ulutan, D. Development of laser polishing as an auxiliary post-process to improve surface quality in fused deposition modeling parts (2017) ASME 2017 12th International Manufacturing Science and Engineering Conference, MSEC 2017 collocated with the JSME/ASME 2017 6th International Conference on Materials and Processing, 2.

[7] Maidin, S., Muhamad, M.K., Pei, E. Feasibility study of ultrasonic frequency application on fdm to improve parts surface finish (2015) Jurnal Teknologi, 77 (32), pp. 27-35.

[8] Chaidas, D., Kitsakis, K., Kechagias, J., Maropoulos, S. The impact of temperature changing on surface roughness of FFF process. (2016) IOP Conference Series: Materials Science and Engineering, 161 (1), art. no. 012033.

[9] You, D.-H. Optimal printing conditions of PLA printing material for 3D printer. (2016) Transactions of the Korean Institute of Electrical Engineers, 65 (5), pp. 825-830.

[10] Buj-Corral, I., Bagheri, A., Domínguez-Fernández, A. Influence of Structure Support Printing Parameters on Surface Finish of PLA Hemispherical Cups for Emulation of Ceramic Hip Prostheses (2018) Procedia CIRP, 68, pp. 347-351.

[11] Ramli, F.R., Faudzie, M.S.M., Nazan, M.A., Alkahari, M.R., Sudin, M.N., Mat, S., Khalil, S.N. Dimensional accuracy and surface roughness of part features manufactured by open source 3D printer (2018) ARPN Journal of Engineering and Applied Sciences, 13 (3), pp. 1139-1144.

[12] Valerga, A.P., Batista, M., Fernández-Vidal, S.R., Gómez-Parra, A., Marcos, M. Preliminary study of the influence of manufacturing parameters in fused deposition modeling (2015) Annals of DAAAM and Proceedings of the International DAAAM Symposium, 2015-January, pp. 1004-1008.

[13] Altan, M., Eryildiz, M., Gumus, B., Kahraman, Y. Effects of process parameters on the quality of PLA products fabricated by fused deposition modeling (FDM): Surface roughness and tensile strength (2018) Materialpruefung/Materials Testing, 60 (5), pp. 471-477.

[14] Hafsa, M.N., Ibrahim, M., Wahab, M.S., Zahid, M.S. Evaluation of FDM pattern with ABS and PLA material. (2014) Applied Mechanics and Materials, 465-466, pp. 55-59.

# REFINING THE PROCESS OF DESIGNING AN ELECTRICAL RESISTANCE HEATER FOR VACUUM FURNACE IN NON-STATIONARY PROCESS

PhD E. Angelova. Faculty of Transport, University of Ruse, Bulgaria
eangelowa@uni-ruse.bg

***Abstract:*** *Designing an electrical resistance heater for vacuum furnace is a result of multiple thermo-technical and electro-technical calculations in order to determine the optimal power. The process of heating must also comply with the technological requirements for temperature differences between the inside and the surface of the processed products. Considering the complicated heat transfer in the furnace, there is no complete methodology for determining the heat conditions of the participants in the heat transfer differentiating in time and space. In this paper it is systemized a sequence of applied mathematical and numerical models as well as geometric dependence for deriving the angular coefficients of radiant interchange in the process of determining the temperature of every participant in the heat transfer in order to refining the process of designing an electrical resistance chamber.*

**KEYWORDS**: *VACUUM, FURNACE, HEATER*

## *1. Introduction*

The main purpose of the vacuumed furnace, as with all other furnaces, is to provide certain temperature condition for implementing a predetermined technological process. Usually, in the terminology, by furnace it is meant the chamber where the products are thermally processed. As a consequence of the specificity in heating in vacuum, most commonly used are the electrical resistance heaters.

When designing a new vacuum chamber the most significant calculations are those related to determining the power of the heater. It has to ensure the necessary optimal speed for heating the product. Usually the diversity of products that are processed in the same furnace impede determining the optimal power since it depends on multiple factors.

Designing an electrical resistance heater for vacuum furnace is a result of multiple thermo-technical and electro-technical calculations in order to determine the optimal power. The process of heating must also comply with the technological requirements for temperature differences between the inside and the surface of the processed products. Considering the complicated heat transfer in the furnace, there is no complete methodology for determining the heat conditions of the participants in the heat transfer differentiating in time and space.

In this paper it is systemized a sequence of applied mathematical and numerical models as well as geometric dependences for deriving the angular coefficients of radiant interchange in the process of determining the temperature of every participant in the heat transfer in order to refining the process of designing an electrical resistance chamber.

## *2. Exposure*

In a vacuum furnace there are available all methods for heat transfer

- radiation – screens, all objects in the chamber
- convection – the water layer of the cooling water
- conduction – between the layers of the wall

and combined heat transfer processes;

-conductive – radiant – electrical conductor, heater, processed product, stand

-conductive – convective - outer layer with ambient environment

A selection has been made from three objects (fig. 1), that covers all kinds of heat transfer that exist between the objects in the chamber.

In [1] it is represented a system of differential equations that with motivated simplifications describe the thermal condition of the objects in the vacuum furnace. In fact, the main problem with conjugated limit equation are two: first – defining the limit conditions and second – finding appropriate method for solution.

***Fig.1*** *Distribution of electrical energy in the system*

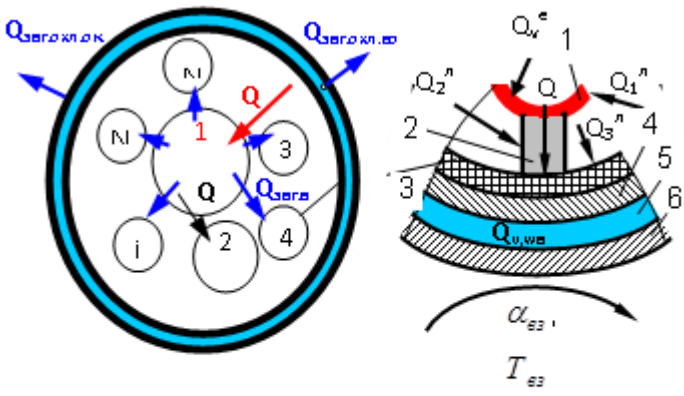


**DESCRIPTION OF THE MODEL**

| № | Differential equations | Conjugated limit equations |
|---|---|---|
| **1.** | $C_1 \frac{\partial T_1}{\partial t} = \frac{Q_1^{\pi}}{F_1^{\wedge}} - q_k + q_v^{en.}$ | |
| **2.** | $C_2 \frac{\partial T_2}{\partial t} = \frac{Q_2^{\pi}}{F_2^{\wedge}} + q_k$ | |
| **3**<br>**4**<br>**i**<br>**6** | $C_i \frac{\partial T_i}{\partial t} = \frac{1}{R}\frac{\partial}{\partial R}\left(\lambda_i R \frac{\partial T_i}{\partial R}\right)$ | $\lambda_3 \frac{\partial T_3}{\partial R} = \frac{Q_3^{\pi}}{F_3} \quad \left\|R = R_3\right.$<br>$\lambda_i \frac{\partial T_i}{\partial R} = \lambda_{i+1} \frac{\partial T_{i+1}}{\partial R} \quad \left\|R = R_i\right.$<br>$\left\|T_i = T_{i+}\right.$ |
| **5** | $C_5 \frac{\partial T_5}{\partial t} = \frac{1}{R}\frac{\partial}{\partial R}\left(\lambda_5 R \frac{\partial T_5}{\partial R}\right) + q_v$ | $\lambda_6 \frac{\partial T_6}{\partial R} = \alpha_{b3}\left(T_{b3} - T_6\right) \quad \left\|R = R_7\right.$ |

$Q^{л}_{1,2,3}$ is calculating using Gebhart method [1]

$$Q^{л}_{k} = A_k \varepsilon_k \delta T_k^4 - \sum_{j=1}^{N} A_j \varepsilon_j \delta T_j^4 G_{jk},$$

$$G_{jk} = F_{j-k}\varepsilon_k + F_{j-1}\rho_1 G_{1k} + F_{j-2}\rho_2 G_{2k} + ....F_{j-k}\rho_k G_{kk} .... + F_{j-N}\rho_N G_{nk}$$

, where

$G_{jk}$ - the share of every object in radiant heat transfer;

$$q_k = \frac{(T_1 - T_3)\lambda_2}{H};$$

$$q_v = \frac{V_{\partial e б}}{V_o} T^*;$$

$F_i$ - area of $i^{-th}$ object;

$R$ - radius;

$q$ - heat stream;

$Q$ - heat quantity;

$F_{j-k}$ - angular coefficient of heat interchange;

$\varepsilon$ - degree of blackness;

$\rho$ - absorption coefficient

$C_i$ -heat capacity;

$\delta$ - Stefan-Boltzmann constant;

$\lambda$ - thermal conductivity coefficient;

$V_{\partial e б}$ - water cooling flow rate;

$V_0$ - water layer volume;

$T^*$ - temperature of incoming cooling water

The share of radiant interchange between objects is represented by a system of algebraic equations that after transformation can be calculating using the Gaussian method

With discrete representation with time and space there are two known main solutions

In[ 2] it is shown a motivation for choice of numerical method for solution of analytical models. It is necessary not only discretization in time for objects in which the heat transfer is accomplished through thermal conductivity, it is necessary to discretization in space. The choice of solution is motivated– known in literature as "obvious scheme". In order to eliminate mistakes by inaccuracy in calculations as well as the risk of inability to continue (getting stuck) in small differences (T – T) it is necessary to set requirements for the values of two intervals – space and time. The influence of the two intervals on the result of calculations is examined in the literature [4,5].

For the flat wall it is introduced generalized criteria for resistance [5] that represent the interdependence of two intervals (1). Accomplishing that requirement make the scheme stable against unavoidable calculation errors.

$$\frac{\rho c \Delta x^2}{\lambda \Delta \tau} \geq 2 \quad \textbf{(1)}$$

By analogy it is deduced the criteria for resistance of cylindrical wall.

$$\frac{c \rho \Delta R^2}{\lambda \Delta \tau} \geq 2 \quad (2)$$

The heat transfer in vacuum furnace is predominantly radiant. For tracking the thermal condition of the objects during heating (cooling), it is necessary to determine the angular coefficients of radiant interchange for every object with the other objects. The methods known in the literature, including the geometric one, calculate the heat transfer only between two objects. The applications for real thermal systems is partial and limited.

The geometric dependencies deduced from the thermos-technical theory for determining the angular coefficients of radiant interchange, in many cases, do not cover the possible situation for two planes as well as does not take into account the impact of other objects as it is in real conditions. They are becoming even less applicable when there are intermediate objects as well as the situations where it is need to take into an account the barriers for heat radiant from its own surfaces.

In [3] it is suggested a geometric approach for determining the angular coefficients for closed thermal system with unlimited number of objects and unspecified alignment among them.

The main goal when designing a vacuum furnace is searching for such a solution for the thermal model so that it can be chosen the optimal values for the main parameters, so that, it can be ensured a high productivity with low energy intensity. An indicator for furnace efficiency is losses. The losses are consequences of forced water cooling of the walls, as well as, cooling through natural convection with air. In order to simplify the solution the dynamic water layer is substituted with stationary one. The total heat content of the dynamic layer can be expressed as a sum the of heat content of two volumes. First ($V^{in.}$) is entered for time $\Delta\tau$ volume of water with temperature $T^{in.}$. For that amount of time, from the first volume $V^0$, that from the beginning of the interval $\Delta\tau$ was with temperature T', is leaving a portion of water with the same volume ($V^{in.}$), but with temperature T'.

At the end of the interval $\Delta\tau$, the rest of the overall volume ($V^0$-$V^{in.}$) is with temperature T'.

The new heat content of the layer corresponds a temperature $T^{cor}$, that is considered homogeneous throughout the overall volume.

$$c\rho V^0 T_{cor.} = c\rho V^{in.} T^{in.} + c\rho (V^0 - V^{ex.}) T' \quad (3)$$

After transformation of $T_{cor.}$ the result is (3).

$T_{cor.}$=W+T', where $W=(T^{in.} - T')\frac{V^{in.}}{V^0}$ - correction value (4)

The proposed approach is experimentally verified with specialized software product. Data has been taken from real heating in vacuum furnace. The result has been compared and overlap and conclusions are published in [6].

## *3. Conclustions*

- The thermal model, represented as a system of differential equations binds all three types of heat transfer – radiant,

conductive and convective that are typical for vacuum furnace

- The solution of the system of equations with the proposed numerical method gives adequate representation of the distribution of thermal field in time and space
- The limit conditions in conductive heat transfer, with chosen time interval, discretize the temperature by volume represented by the method of extreme difference between them.
- For instant thermal condition of the object`s surface in radiant heat transfer, it is represented by a system of equations (linear) using the Gibhart`s method. The solution is calculated using Gauss method
- Dependencies have been deduced and new approach has been suggested for rendering the influence of cooling water

Using the pruposed sequence of mathematical and numerical method garantees to determine the power of the heater that ensure diverse technological requirements with different heat treatments.

## *4.Literature*


1.Trifonov T., E. Angelov, Analytical model of temperature condition of electricity resistant vacuum furnace with non-stationary heat transfer, Scientific papers of University of Ruse, 2002

2..Trifonov T,, E. Angelova, Choice of numerical method for solution of analytical model for non-stationary processes in vacuum furnace, Scientific papers of University of Ruse, 2003.

3.Angelova, E., T. Trifonov, "Geometric Determination of the angle coefficients of mutual irradiation closed heat system", Journal of the Technical University at Plovdiv Fundamental Sciences and Applications", Vol. 13, 2006 Anniversary Scientific Conference'2006, 70-75, Bulgaria.

4.Karlsou. G, D.Eger. Heat transfer hard тел, Science, Moscow, 1964.

5.Zarubin B. Engineering methods for solving heat transfer problems , Moscow, 1983.

6.Angelova E, T. Trifonov, Application of specialized software product for solving heat transfer problems for vacuum furnace, Scientific papers of University of Ruse, 2003.

# DEVELOPMENT AND IMPROVEMENT OF TECHNOLOGIES FOR PRODUCING STRUCTURAL MATERIALS WITH ULTRAFINE-GRAINED STRUCTURE BY SEVERE PLASTIC DEFORMATION

## РАЗВИТИЕ И УСОВЕРШЕНСТВОВАНИЕ ТЕХНОЛОГИЙ ПОЛУЧЕНИЯ КОНСТРУКЦИОННЫХ МАТЕРИАЛОВ С УЛЬТРАМЕЛКОЗЕРНИСТОЙ СТРУКТУРОЙ МЕТОДОМ ИНТЕНСИВНОЙ ПЛАСТИЧЕСКОЙ ДЕФОРМАЦИИ

c.t.s., associate professor Lezhnev S.[1]; d.t.s., professor Naizabekov A.[1]; PhD Panin E.[2], PhD Arbuz A.[2]

[1] Rudny industrial institute, Rudny, Kazakhstan; [2] Karaganda state industrial University, Temirtau, Kazakhstan
e-mail: sergey_legnev@mail.ru

**Abstract**: Paper presents an overall analytical review of recent achievements in the field of development and improvement of technologies for producing structural materials with ultrafine-grained structure by severe plastic deformation. Main modern methods of obtaining ultrafine-grained structure by severe plastic deformation are described. Special attention to combined process “helical rolling - pressing” is devoted.

**Keywords**: severe plastic deformation, ultrafine-grained structure, technology, combined processes.

### *1. Introduction*

The creation of new structural materials with new unique properties remains one of the urgent problems of modern materials science. In practice, it is possible to improve the properties of already existing structural materials by grinding their structure to ultrafine-grained state. At the moment, there are several ways to obtain an ultra-fine structure and one of these methods is a method of severe plastic deformation (SPD), implemented in the entire volume of the deformable workpiece.

The most well-known method for implementing SPD in ferrous and non-ferrous metals is equal-channel angular pressing [1]. This method ensures the production of ultrafine-grained structure in the metal during 6-10 pressing cycles. At the same time, in order to reduce the required number of pressing cycles, to produce a metal with a given grain size over the past decade, a number of dies of different modifications have been developed that ensure the implementation of this method of deformation. But until now, this method has not found application in the real industrial sector because of the lack of deformation in this method, which consists in discreteness, i.e. inability to process products of relatively long length and the need for a large number of processing cycles. And it sets out the economic inexpediency of introduction of this method in production.

### *2. Concept of combined processes*

For the solution of a problem of reception ultrafine-grained materials by methods of severe plastic deformation (SPD) in industrial conditions we had developed a number of the combined technologies of deformation allowing to receive rods of rectangular and round section from ferrous and non-ferrous metals with ultrafine-grained structure. These processes include the following combined processes: "rolling - ECA-pressing" [2-6] (Fig. 1, a), "helical rolling - ECA-pressing" [7] (Fig. 1, b).

The essence of the proposed combined methods of deformation is as follows. Preheated to the temperature of the beginning of deformation (for some non-ferrous metals, an option is possible at room temperature), the workpiece is fed to the rolling rolls, which, due to the forces of contact friction, capture it in the gap of the rolls, and at the exit from it is pushed through the channels of an equal-channel step matrix.

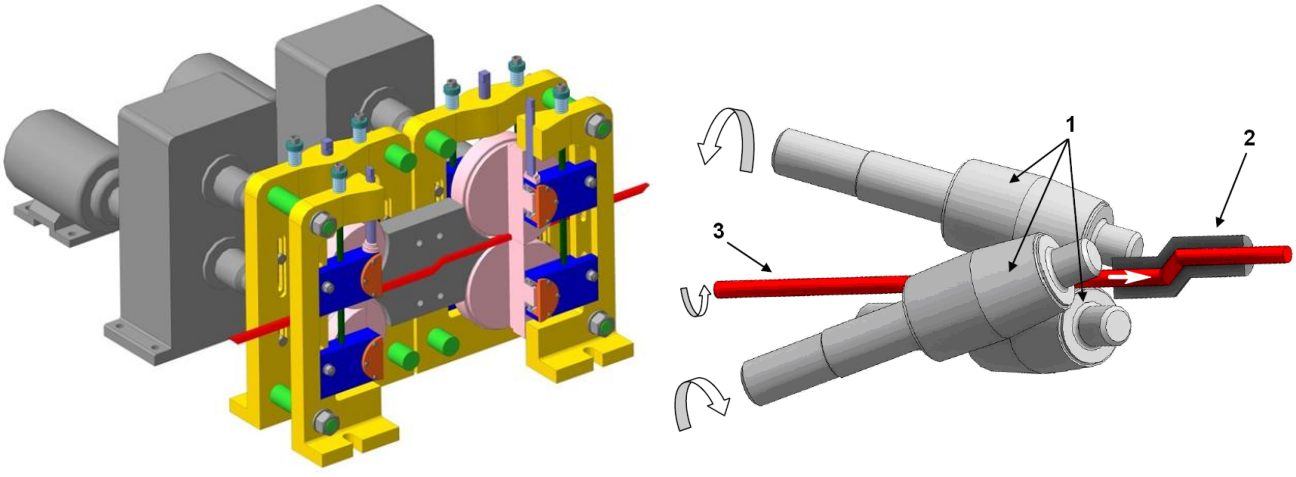


a) b)

1 - conical rolls; 2 - equal-channel step matrix; 3 - workpiece.
Figure 1 – The scheme of the combined process

In this case, the process of pressing in an equal-channel step matrix is realized by using the contact friction forces arising on the surface of the metal contact with rotating rolls.

When implementing the combined process of "rolling - ECA-pressing" after the workpiece is completely out of the matrix channels, it is captured by a second pair of rolls, which are also due to the contact friction forces capture the workpiece and fully pull it out of the matrix. When implementing the same combined process "helical rolling - ECA-pressing" after the workpiece is completely out of the gap of the rolls, the following billet is fed to them, which, passing through the rolls and once in the matrix, pushes the previously deformed billet from the matrix.

The combination of the rolling process (longitudinal and helical) and subsequent pressing in an equal-channel step matrix allows to realize a favorable scheme of the stress-strain state with the implementation of severe plastic deformation in the entire volume of the deformed metal, which creates good conditions for the formation of an ultrafine-grained structure.

As a result of numerous laboratory experiments to study the effect of the proposed methods of deformation on the evolution of the microstructure of various structural materials (ferrous and non-ferrous metals and alloys) and change their properties, it was proved that the combined processes "rolling - ECA-pressing" and "helical rolling - ECA-pressing " have undeniable advantages over conventional equal-channel angular pressing, both in terms of more intense grain crushing and higher mechanical characteristics of the deformable metal in one cycle of deformation, and in terms of the possibility of obtaining long blanks [8, 9].

During one of these studies, we have conducted an experiment on the deformation of workpieces with a diameter of 30 mm and a length of 300 mm of alloy structure steel, grade 40X on the stand implementing a combined process of "helical rolling - ECA-pressing" (Fig. 2), which was assembled on the basis of the rolling mill 10-30, in order to study the influence of the proposed method of deformation on the evolution of the structure of the steel grade.




Figure 2 – The stand implementing the combined process of "helical rolling - ECA-pressing" at the time of the experiment and non-rolled butt-end

For the experiment rods with a diameter of 30 mm and a length of 300 mm (4 pieces) were produced. The rods have heated up to 800 ºC in a tube furnace Nabertherm R120/1000/13 with exposure of 30 minutes. Then, the samples were rolled for 2 passes on a rolling mill 10-30 up to a diameter of 22 mm. At the next stage, ECA-matrix was mounted at the mill and bars were deformed by combined method up to a diameter of 20 mm. All 4 workpieces were rolled by this scheme, while the subsequent billet is pushed from the matrix to the previous one. Then, the matrix was disassembled, the butt-end was extracted, which was leveled in the rolls of the mill at another pass without compression, heated in the furnace to an initial temperature of 800 ºC and processed on a combined installation by the rear, untreated end. The pieces will then be warmed again, replaced installed on the mill matrix, a matrix with a smaller bore diameter and in the same way, cut bars up to a diameter of 18.5 and 17.0 mm. After each passage for conducting metallographic analysis the samples from longitudinal sections of the rod were cut.

## *3. Results and discussion*

The samples were investigated using scanning electron microscope Quanta 200i 3D (FEI company, USA). Photos of typical types of microstructure in the center and on the periphery of the rod after screw rolling, and after the third pass on the combined stand "helical rolling - ECA-pressing" are shown in figure 3.

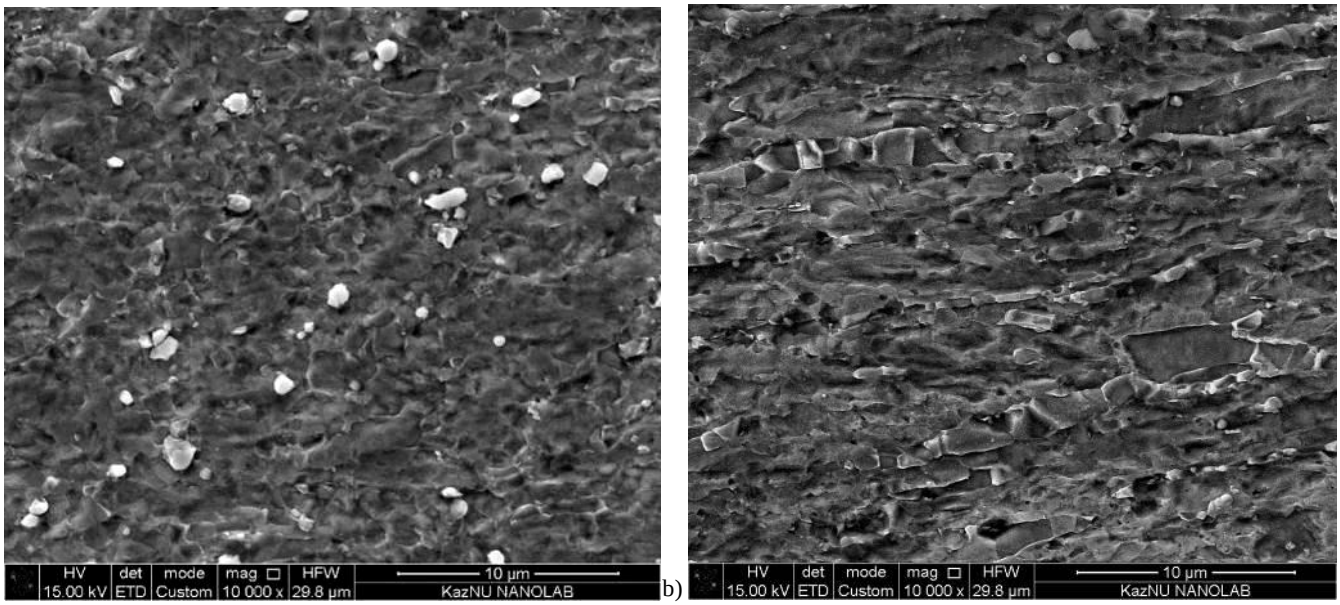

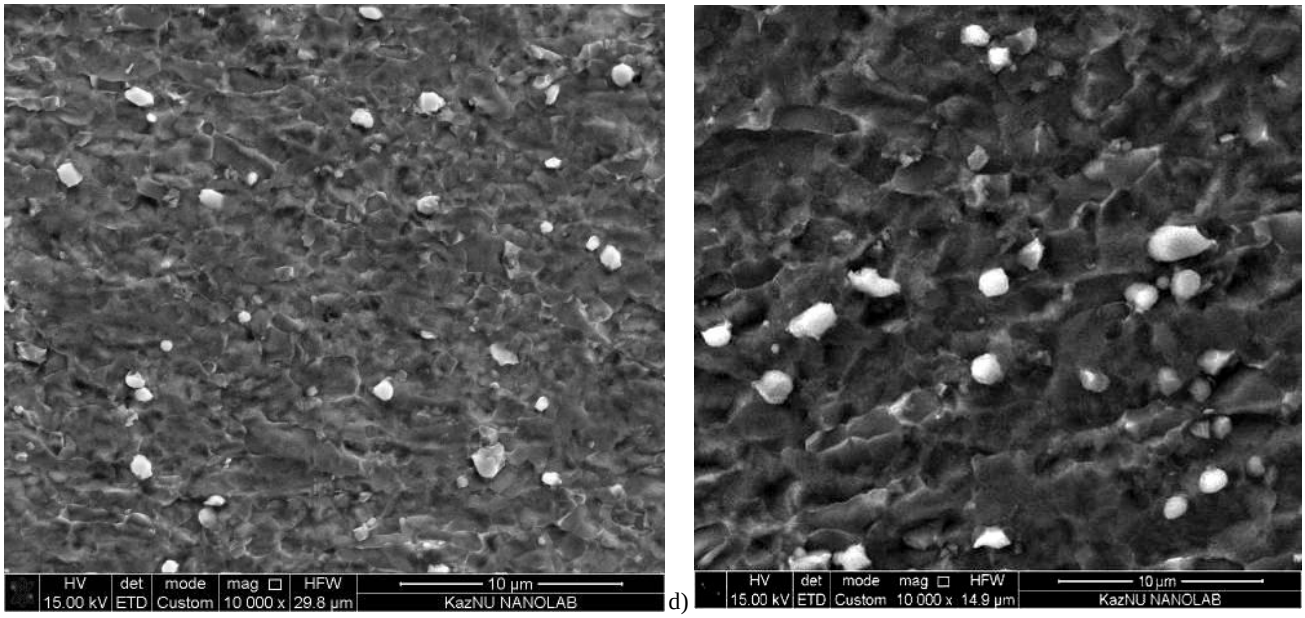


a, b – the periphery and the center of the rod after rolling to a diameter of 22 mm;
c, d – the periphery and the center of the rod after three passes on the combined stand "helical rolling - ECA-pressing"
Figure 3 – Microstructure of steel 40X (X10, 000)

The microstructure of the peripheral zone has a predominantly equiaxed sub-ultrafine-grained nature with grain size about 1 µm. In the central zone there is a structural stripe in the form of elongated grains in the direction of rolling with a size of 5÷10 x 0.9÷1.5 µm and a chain of chromium carbide crystals (white phase). The microstructure obtained after rolling on a helical mill before entering the workpiece into the matrix is typical for this type of deformation and confirms the data presented in [10-11].

The study of samples after three passes on the combined installation "helical rolling - ECA-pressing" (figure 3, c, d) showed a change in the striped texture of the central zone of the bar to a more equiaxed structure with the grain size of the order of 3-6 microns. The peripheral portion of the workpiece retained the ultrafine-grained character.

A typical picture of the transition zone at a distance of 0.5 radius from the center of the rod is shown in figure 4. The transition zone after the second pass still retains traces of the oriented "rolling" structure, although significantly altered. After the third pass, the transition zone has a fine-grained structure with grain size of the order of 1-1.5 microns.

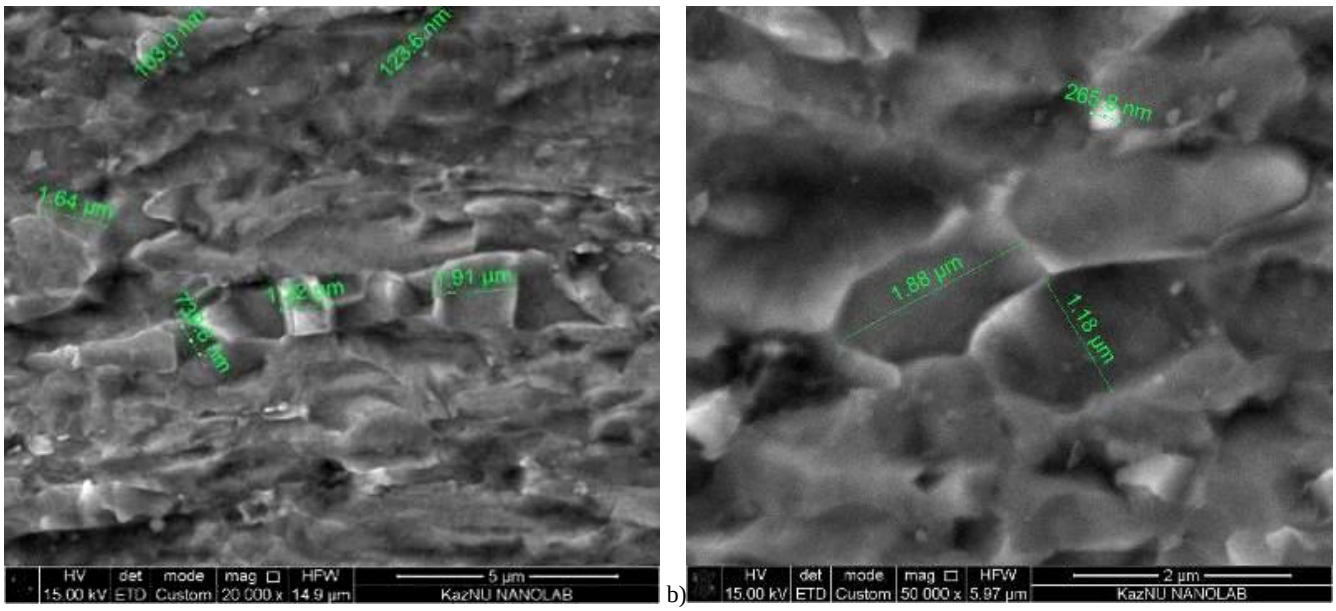


Figure 4 - Microstructure of the transition zone at a distance of 0.5 radius from the center of the bar after the second pass (a) and third pass (b)

According to the results of measurements of the grain size of steel 40X, it can be concluded that the high intensity of shear deformation characteristic of screw rolling and combined process "helical rolling - ECA-pressing", allows to largely grind grain. Moreover, the combined process, due to the greater non-monotonicity of the plastic flow of the metal, grinds the grain to a greater extent, allowing to obtain grain with a minimum average size of up to 1 µm. At the same time, metallographic studies have shown the transformation of the oriented banded structure of the central zone into a more equiaxed structure with a predominance of large-angle intergranular boundaries.

## *4. Conclusion*

Implementation and bringing to the industrial use of the proposed combined processes will allow to obtain a method of continuous extrusion of high-quality rod with rectangular and circular cross-section. The economic and energy efficiency of the proposed technology in comparison with the traditional technology

of equal-channel angular pressing is to reduce the number of deformation cycles required to obtain a uniform ultrafine-grained structure by almost 2 times and in a larger proportion of the material produced in one cycle of processing by ensuring the continuity of the process. Thus, at comparable quality, productivity, and hence efficiency of installations for realization of the offered combined processes will be not less than 2 times higher. At the same time, the necessary set of properties is formed in fewer passes, and the proposed installation have no restrictions on the length of the workpiece. This makes it possible to talk about the energy-saving advantages of the proposed technology and the prospects for its commercial application.

## *5. References*


1. Валиев Р.З., Александров И.В. Наноструктурные материалы, полученные интенсивной пластической деформацией. - М.: ЛОГОС, 2000. - 272 с.

2. Патент РК № 23802 Устройство для непрерывного прессования металла. Найзабеков А.Б., Лежнев С.Н., Панин Е.А., 2012. Бюл. 9.

3. Патент РК №25862 Устройство для непрерывного прессования металлов и сплавов. Найзабеков А.Б., Лежнев С.Н., Панин Е.А., 2013. Бюл. 7.

4. Патент РК №25863 Устройство для непрерывного прессования металла. Найзабеков А.Б., Лежнев С.Н., Панин Е.А., 2013. Бюл. 7.

5. Патент РК №27262 Устройство для непрерывного прессования металлов и сплавов. Найзабеков А.Б., Лежнев С.Н., Панин Е.А., 2016. Бюл.10.

6. Патент РФ № 2629134 Устройство для непрерывного прессования металлов и сплавов, Мазур И.П., Лежнев С.Н., Найзабеков А.Б., Панин Е.А., Ведищев Р.О., 2017. Бюл. 24

7. Патент РК №27445 Устройство для непрерывного прессования металла. Найзабеков А.Б., Лежнев С.Н., Арбуз А.С., 2016. Бюл. 10.

8. Theoretical and technological bases of obtaining sub ultrafine-grained structural metals and alloys by new combined process "rolling – ECA-pressing»: Monograph / E.A. Panin, A.B. Naizabekov, S.N. Lezhnev et al. – Rudny: RII, 2018. – 144 p.

9. Теоретические и технологические основы получения субультрамелкозернистых конструкционных металлов и сплавов новым совмещенным процессом «винтовая прокатка – РКУ-прессование»: Монография./ Найзабеков А.Б., Лежнев С.Н., Арбуз А.С. и др.// - Рудный: РИИ, 2017. – 193 с.

10. Lopatin N.V., Salishchev G.A., Galkin S.P. Mathematical modeling of radial-shear rolling of the VT6 titanium alloy under conditions of formation of a globular structure // Russian Journal of Non-Ferrous Metals. – 2011. - №52 (5). – P. 442-447.

11. Лопатин Н. В. Улучшение технологической деформируемости сталей 45 и У10А термомеханической обработкой с использованием радиально-сдвиговой прокатки: автореф. … канд. техн. наук. – Уфа, 2007. – С.3-10.

# DESIGN AND ANALYTICAL APPROACH TO UNIFORM MATERIAL STRUCTURE OF INJECTION MOLDING PARTS

Berenika Hausnerová[1,2], Jakub Huba[1]
Faculty of Technology – Tomas Bata University in Zlin, Czech Republic[1]
Centre of Polymer Systems – Tomas Bata University in Zlin, Czech Republic[2]

hausnerova@utb.cz

***Abstract:*** During injection molding of highly filled polymers it is necessary to avoid any inhomogeneities arising from high shear rates/stresses created in molded parts, because they lead to uneven shrinkage after molding, dimensional instabilities and even cracks and voids in the final parts. The testing mold design to intercept so called powder-binder separation has been upgraded to a 3D cube-like model and constructed. Investigation of a tendency to phase separation is however strongly affected by a material and a surface structure of a processing tool. Therefore, flowability of various filled materials in the flow channels designed from different construction materials were tested and compared within this contribution.

**Keywords:** INJECTION MOLDING, HIGHLY FILLED POLYMER MELTS, SURFACE ROUGNESS, FLOWABILITY

## *1. Introduction*

Injection molding of filled polymers is still a challenging engineering task – especially in case of extremely highly filled compounds as those employed in powder injection molding, where any structural inhomogeneity introduced during injection molding step has a detrimental effect of the quality of the final parts.

Recently[1] we put a lot of effort to design a testing mold to intercept so called powder-binder separation occurring during high shear rates and stresses generated during injection molding. It has been developed at the Tomas Bata University in Zlin in cooperation with Fraunhofer IFAM, Bremen and consists of four sections and each section is connected with the 1 mm long gate in the section profile. The inner side length of first three sections and the outer side length of the last section is 10 mm. The mold cavity contains the inner and outer corners, the radical thickness variations, the areas with the weld lines and very thin film part, which is 0.3 mm deep. Later, it has been upgraded to a 3D cube-like model and constructed[2].

On this geometry, the novel evaluation method based on a scanning electron microscopy with an energy dispersive X-ray (SEM/EDX) has been proposed[3]. In the methodology, the quantitative EDX mapping as the measure of separation was carried out. To convert qualitative grayscale maps into quantitative information, it was necessary to assign relative parameter, where 0 % represents purely white area and 100 % completely dark spots. Then, the concentration EDX maps of the powder and/or the binder elements after injection molding have been analyzed mathematically to obtain the single value so called the variability parameter. This variability parameter represents the size of the powder or binder non-uniformity within the tested samples. To avoid inhomogeneities from local concentration imperfections, the EDX maps have been smoothed, when each pixel was considered as an average of (5 x 5) neighboring pixels. The whole process of quantitative analysis is visualized in *Fig. 1*.

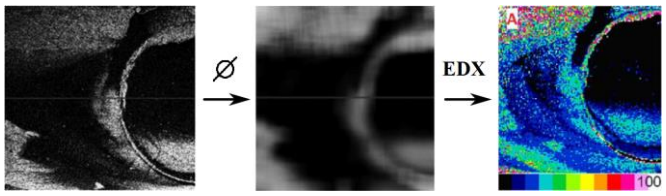


***Fig. 1*** *Evaluation of powder/binder content based on SEM/EDX analysis*[3]

In the next step, the attention was given to both material and processing factors influencing the separation. First, the interactions among the polymers and fillers have been investigated using a unique method combining FTIR and calorimetry applied on the low molecular weight analogues[4,5]. Second, influence of the interactions of feedstocks to a mold surface has been considered[6].

According to the preliminary findings[6], clearly not only the material composition of the processing tools (mold, flow channels) is of importance, but also their surface roughness. However, the complicating factor of its evaluation is a wear accompanying the molding, which makes the processing conditions unstable. The wear affects the roughness profile of mold cavities, and subsequently influences surface energy, and phase separation. Wear is also associated to a lifetime of molds and a cost of final products.

In this paper we present the results of the flowability of various natural fiber reinforcing materials (called NFR) in a flow channels designed from different construction materials.

## *2. Experimental*

### *2.1 Materials*

As testing materials the compounds with different filler type and content have been used. For thermoplastic matrices the most versatile polyolefin systems have been chosen, namely polypropylene (PP) and high-density polyethylene (HDPE). HDPE has been mixed with a disintegrated slate powder with fraction size lower than 0.4 mm and wood fibers, while PP compound contains talc powder.

### *2.2 Processing Tools*

For the flowability tests of these NFR materials, the common mold designs with different coating have been used. Mold substrate was constructed from carbon tool steel 1.1730. This substrate material has been hardened and afterward immediately tempered to obtain hardness of 50 HRC. Subsequently, surface of the cavity has been coated with three different coatings: titanium diboride ($TiB_2$), titanium carbonitride (TiCN) and amorphous hydrogenated carbon coating (a:C-H). Surface of the a:C-H coating has been grinded. Two variations of surface quality have been obtained - grinded and polished - for cavities with $TiB_2$ and TiCN coatings.

***Table 1****: Properties of the coatings*

| | $TiB_2$ | TiCN | a:C-H |
|---|---|---|---|
| Microhardness HV 0.025 | 2500-3200 | 3000-4000 | 2000-4000 |
| Thickness [μm] | 2-3 | 1-20 | 1-3 |
| Coefficient of friction | 0.4-0.5 | 0.5-0.6 | 0.05-0.15 |

Each coated mold insert with spiral cavity had a flat counterpart with the same coating and surface quality (*Fig. 2*). The width of flow domain was 6 mm and 1.3 mm in depth.



***Fig. 2*** *Coated spiral cavity insert and counterpart*

The tests of the flowability have been done with injection molding machine Arburg 370 C. All compounds were processed with the same molding parameters, which are depicted in *Table 2*.

***Table 2:*** *Process parameters of injection molding*

| Molding Parameter | Value |
|---|---|
| Injection pressure [bar] | 1500 |
| Holding pressure [bar] | 1200 |
| Holding time [s] | 4 |
| Cycle time [s] | 20 |
| Melt temperature [°C] | 190 |
| Mold temperature [°C] | 30 |

## 3. Results

Flowability of the tested NFR feedstocks varies with different coating systems. From *Fig. 3* it can be seen that in case of $TiB_2$ coating, higher roughness of the mold surface negatively affects the flowability of all feedstocks. On the other hand, in terms of the flowability for TiCN surface, higher roughness of the grinded surface results in a better flow performance of the tested feedstocks.

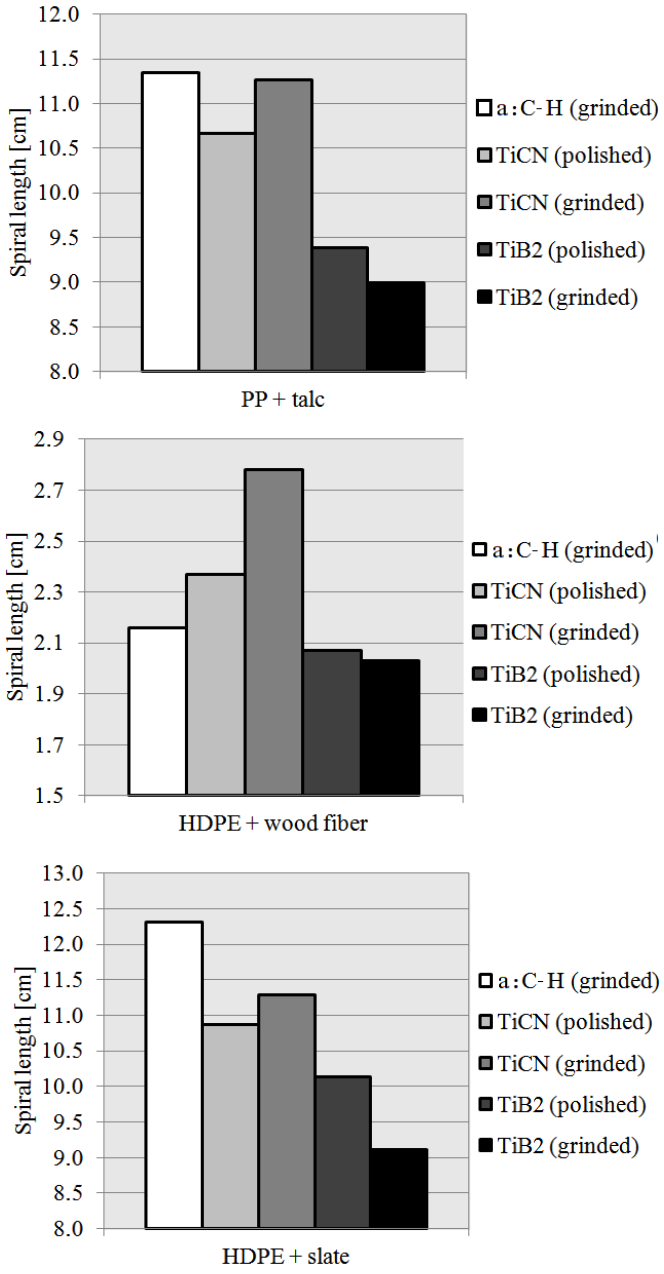


***Fig. 3*** *Flowability results of different compounds and coatings*

As highly filled materials are injected into the mold, jetting flow may occur (*Fig. 4*). According to the spiral length of the wood fiber compound, the viscosity of system is much higher in comparison to mineral filled feedstocks. Jetting might be also problem of slip-stick effect due to its occurrence in polished cavities of TiCN and $TiB_2$ coatings.



***Fig. 4*** *Jetting phenomenon in polished cavities*

These findings should be taken into account, when simulating the molding; only then we can expect the enhancement in the efficiency of the processing of NFR materials.

## 4. Acknowledgment

This work has been financially supported through EU project entitled Smart Coating Systems for Process Control and Increased Wear Resistance in Processing of Natural Fibre Reinforced Polymers (CORNET SmartNFR, call 01_15_007 Cooperation – Clusters – Call I – Collective Research, registration number of the project CZ.01.1.02/0.0/0.0/15_007/0001161).

## 5. References

1. JIRANEK, L., HAUSNEROVA, B., HARTWIG, T., Community Design 001704974, Office for Harmonization in the Internal Market, Alicante, (6 May 2010)

2. HAUSNEROVA, B., HUBA, J., Injected structure for quantitative evaluation of phase separation of composite based on polymeric matrix highly filled with metallic or ceramic powder. IPC: Czech Republic. Utility model, CZ 2014-30495 U1

3. HAUSNEROVA, B., SANETRNIK, D., PONIZIL, P. Surface structure analysis of injection molded highly filled polymer melts, *Polymer Composites*, 34, 1553–1558 (2013)

4. BLEYAN, D., HAUSNEROVA, B., SVOBODA, P.: The development of powder injection moulding binders: A quantification of individual components' interactions. *Powder Technology* 286, 84-89 (2015)

5. BLEYAN, D., SVOBODA, P., HAUSNEROVA, B.: Specific Interactions of Low Molecular Weight Analogues of Carnauba Wax and Glycol Binders of Ceramic Injection Moulding Feedstocks. *Ceramic International* 41, 3975-3982 (2015)

6. BLEYAN, D., HAUSNEROVA, B., KASPARKOVA, V., PATA, V., Surface Adhesion between Ceramic Injection Molding Feedstocks and Processing Tools. *Ceramics International* 42, 460-465 (2016)

# TO THE PROBLEMS OF FLUORESCENCE EXCITATION SPECTRUMS

## ОБ СПЕКТРАХ ВОЗБУЖДЕНИИ ФЛУЮРЕСЦЕНЦИИ

Prof. Gomidze N.[1], M.Sc. of Radio-Physics Shainidze J.[2], M.Sc. of Radio-Physics Shengelia G.[3] PhD. Student of Physics Turmanidze R[4],

Faculty of Physics, Mathematics and Computer Sciences[1234] Batumi Shota Rustaveli State University, Georgia

**Abstract:** *The present paper is dedicated to constructing a phase fluorometer on a phase screen model. The numerical correlation method are applied to evaluate fluorescent signals. The phase shift between the reference signal and the fluorescence signal are studied as the function of statistic moments of random phase screen.*
***KEYWORDS**: FLUORESCENCE, SPECTRUM, PHASE SCREEN, LASER, RANDOM*

### *1. Introduction*

Fluorescence spectroscopy represents the effective method of studying dynamic processes in solutions. This method greatly applied in biology, medicine, material studies and nanotechnology, and of course, in ecology. The parameters of fluorescence spectroscopy, like: radiation spectrum, life duration, quantum yield, fluorescence anisotropy – represent the sensitive functions of the processes, which depend on the life duration of excited condition. The molecules can participate in these processes which are in 10 nm distance from fluorofore at the moment of excitation.

All the molecular system is characterized with the own fluorescence in more or less intensity. Polysaturated, condensed and of course, aromatic and polyaromatic compounds are well fluorescencing. Hetero atomic or electron-domain systems should be particularly mentioned. Special organic and non-organic substances are fluorescencing perfectly, which are used in making displays, monitors, photodiodes and lasers. Natural compounds are fluorescencing in comparatively less quality. From natural admixtures which are fluorescencing well, should be mentioned natural paints, some amino acids (Tryptophan and Tyrosine) and the protein containing them, cofactors (NADH), vitamins (riboflavin). The own fluorescence is the basis of discovering and identifying natural admixtures and oil products.

It is well-known that ***impulsive*** and ***phase-modulated (harmonic)*** methods of fluorescence analyses of liquid media, each method has its advantages in certain direction. For instance, in impulsive method the sample is radiated with short light impulses and measured the influence of fluorescence intensity upon time. In modern spectroscopy, the source of radiation is impulsive lasers of Picoseconds. In periodically repeated impulses, the fluorescence attenuation is registered via either ***stroboscopic method*** or ***photon counting method***.

### *2. Problem discussion*

There are two direct methods of measuring the damping velocity of the fluorescence, so there are phase and impulsive fluorimeters. It is noteworthy that the impulsive fluorimeters - represent simple tools to define life expectancy of fluorescence. The sample is lit with the impulsive light source. The duration of the impulse is lower than the fluorescence life expectancy. Damping of fluorescence is registered on the oscillograph or on the personal computer via the electronics consisting of or analog-digital converters. The principle of measurement is similar to the principle of phosphorescence and slow fluorescence measurement (with several milliseconds of life expectancy).

However, of course, on the frequencies that correspond to the angular damping velocity of fluorescence, it is impossible to create exciting light impulses. For this purpose, two methods are used. In one of the methods, the photomultiplier works in impulsive mode, the time of impulsive mode of which is lower than the life expectancy of fluorescence. The impulsive source and the photomultiplier are turned on with a frequency of several thousand rounds in a second, but with some delay. Fluorescence curves are taken by measuring the time of delay between excitation and registration. The enhanced signal from the photomultiplier connects to the phasemeter's first channel with the coaxial cable. The impulse source of light used during this method should have less duration than the fluorence signal fading time, so it is easy to use hydrogen impulse lamps.

In the second method, photomultiplier works in impulsive mode and has high sensitivity. In this case, the lifespan of light impulses is several times higher than the lifespan of fluorescence. Photomultiplier signal is registered through the detector and can be visualized. For normal intensity, which is enough to get a photographic image, it is necessary to repeat this operation several times. ***Birke, King*** and ***Murno*** [1] used the strobing oscillographs and recorded the curves on the self-recorder.

In the grant projects GNSF/ST08/5-451, FR/152/9-240/14 our team has managed to modernize the laser spectrofluorometer. As a light source we used high-sensitivity impulsive nitrogen laser NL-100 (frequency 0-25 Hz) with which strobing of monochromator and sensitive photomultiplier was carried out. In order to reduce the "electronic noise" caused by the relaxation processes, we used a multichannel analyzer that is compatible with computer-compatible electronic devices such as ADC (analog-digital conversion), DAC (digital analog conversion) and electronic circuits [2,3].

Thus, the phase fluorometer allows us to determine the duration of the received signal through the phase screen with a well-known modulation signal. It is important to know the polarization of the source in defining the phase screen regulations (viscosity, temperature, structure):

$$\mathrm{I}=\left(\frac{\partial\mu}{\partial\rho}\right)^2_{\mathrm{T,X}}\cdot\left(\frac{\partial\rho}{\partial\mathrm{p}}\right)^2_{\mathrm{S,X}}\cdot\left(\bar{\Delta}\mathrm{p}\right)^2_{\mathrm{T,X}}+\left(\frac{\partial\mu}{\partial\rho}\right)^2_{\mathrm{T,X}}\cdot\left(\frac{\partial\rho}{\partial\mathrm{s}}\right)_{\mathrm{P,X}}\cdot\left(\bar{\Delta}\mathrm{s}\right)^2+ \quad (1)$$
$$+\left(\frac{\partial\mu}{\partial\mathrm{x}}\right)_{\mathrm{P,T}}\cdot\left(\bar{\Delta}\mathrm{x}\right)^2,$$

where $\mu$ - a refraction index, $\rho$ - density, $\mathrm{p}$ -pressure, $\mathrm{T}$ - temperature, $\mathrm{S}$ -entropy, $\mathrm{x}$ - molar concentration of a solution.

Schematically, the photon radiation and the absorption is expressed with ***Iablonski diagram*** [4]. The energy of electronic transition is equal to the energy difference between the starting energy level and the final level. Therefore, the transition energy:

$$E=h\vartheta, \quad (2)$$

where $h=6.62\cdot10^{-34}\,\mathrm{j}\cdot\mathrm{sec}$ – plank constant, $\vartheta$ -light frequency.

Emission occurs from a population of *n* excited fluorophores with intensity *I:*

$$I=nE. \quad (3)$$

The energy absorbed by a fluorophore is more important than the energy of an emitted photon. For absorption and emission energy we have:

$$E_a=\frac{h\vartheta}{\lambda_a},\quad E_{em}=\frac{h\vartheta}{\lambda_{em}},\quad E_a<E_{em},\quad \lambda_a>\lambda_{em}, \quad (4)$$

where $\lambda_a$ and $\lambda_{em}$ are wavelengths absorption and emission spectra peaks.

Since not all the molecules present at the excited states will participate in the fluorescence process, a quantum yield $\phi_f$ exists:

$$\phi_f = \frac{I_f}{I_a}, \quad (5)$$

where $I_f$ is fluorescence intensity, $I_a$ - intensity of absorption. In fact $\phi_f < 1$ therefore:

$$I_a = I_0 - I_f . \quad (6)$$

Fluorescence excitation in phase fluorometers occurs with a light beam that is modulated by high frequency. Fluorescence phase, i.e., the degree of modulation was compared to the phase of source. In the case of exponentially fading fluorescence, the shift $\Psi$ between the fluorescent radiation and excitation light phases is depicted with the expression: $\omega\tau = tg(\Psi)$, where $\tau$ is fluorescence life expectancy, and $\omega$ is an angular velocity of the modulation. The signal from the source and the fluorescent signal excited on the sample hit the detector that registers the phase shifts among these signals. For example, ***Bailey*** and ***Rolefson*** measured the phase shifts between these two signals, whereas the two output signals coincide with the phase, the detector registered a minimum signal at the output. There are other methods of measuring the ψ phase shifts based on the determination of the quantity of these two signals. It is obvious that the longer is the life expectancy of fluorescence, the smaller is the size of its modulation. The quality of modulation ($m_s$) in the light beam and fluorescence signal modulation quality ($m_f$) is associated with the ψ phase shifts with the ratio of:

$$\frac{m_f}{m_s} = \cos(\Psi) . \quad (7)$$

The phase shifts measured by these two methods coincide with each other with great accuracy in the case of exponentially fading fluorescence.The distinction is observed only in case of non-exponential fading of fluorescence. One of the main drawbacks of the phase fluorometer in principle is the difficulty in the interpretation of the results which arise in case of non-exponential fading of the fluorescence, but Birks, Dyson and Munro have used this method even in case of non-exponential fading of the fluorescence. In the first phase fluorometers, polarizing exciting light and Kerr effect were used for light beam modulation. In this case, the high-frequency field acts on the fluid or crystal electronic-optical effect. Then, for light modulation, the light diffraction was studied on the ultrasonic waves in the fluid that formed the quartz crystal. The light beam with the constant intensity falls onto the diffraction grating. Among the easiest methods a high-frequency pipe is used, in which the modular light is obtained directly. A relatively convenient method is to use a hydrogen lamp that is powered by a modulated signal.

With the method offered by us, the lifespan of fluorescence can be determined indirectly, from the attempts of damping fluorescence. For the first time this method was proposed by ***Eisenthal*** [5], which described the indirect methods of measuring fluorescent radiation ($10^{-11}$ sec). The impulse of polarized laser light with doubled frequency is partially absorbed by the sample, the absorbed light from the special reflective plate is still going back to the sample, but with modified polarization and some delay. The time of delay is determined by the distance between the sample and the reflective plate. The experiment indicates the dependence of the anisotropy of the impulse on the time of delay. The velocity of the disappearance of anisotropy in small viscosity solutions is measured by the rotation of molecules, and in the viscous solutions – by the lifespan of the excited condition.

### 3. *Objectives and Research Methodology*

Signal source quality is one of the most important parameters, including advanced radar systems. The smaller the phase noise, the greater the spatial distinguishability, and the more accurate the measurement results, including from the moving and turbulent objects. In order to measure the phase noise of the signal source in impulsive mode, it is necessary to operate a very complex system that consists of a number of components, such as phase detectors, Fourier analyzers, and high-quality sources of the reference signal. To ensure accuracy, signal sources have a very high quality. If the quality of the source signal is not provided, then the correlation theory can be used, which is based on correlation of two different source signals. In our case, we get these two sources by directing the reference signal through the cuvette (fig.1).

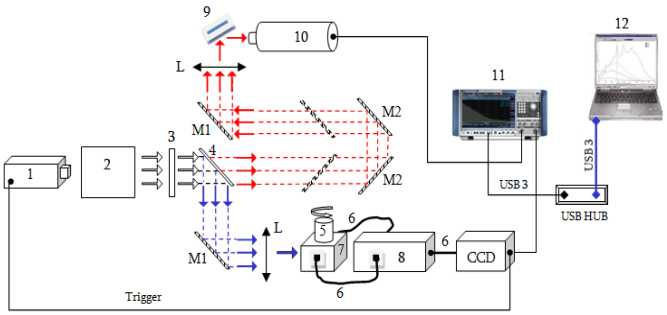


***Fig. 1.*** *Principal scheme of phase fluorometer. 1- light souser, 2 – optical modulator; 3- optical filter, 4- light spliter; 5 – cuvete with rotate system; 6 – optical fiber; 7 – cuvete holder; 8 – correlator of coherence beams; 9 - scattering plate; 10 - photomultiplier; 11 – phase meter; 12 - computer; M1 – stationary minor; M2 - moving mirror; L - converging lens; CCD - monochromator.*

By 90 degree from the base signal, by using optical fiber waveguide we receive partially coherent waves. Extinguishing the noise of the source and the components of the survey system can be realized by averaging the noise in two different measurement tracts. Of course this complicates the measuring system, but it makes it possible to achieve significant improvements in the sensitivity of the detected signal. Using the intercorrelation theory increasing the sensitivity to phase noise can be expressed with the following expression: $\Delta L = 5\log(n)$, where $n$ is the number of correlations. For instance, the averaged increase of the number of correlation 10 times provides the reduction of phase noise in measuring system by 5 dB. At the same time, phase noise is a pivotal parameter not only for radar use but also for tasks that takes into account especially precise measurements. In technology, high-precision measurements of phase noise are used to measure high-sensitive generator parameters such as thermostatic quartz generators, generators with dielectric resonator, synthesizers and so on.

The iterative methods have been developed and widely applied in the tasks of synthesis of diffractive optical elements [6]. The main advantage of these methods is that Iteratical algorithms are more accurate than other algorithms. On the other hand, the realization of the algorithm of synthesis of optical elements on the computer requires significant computing costs. The disadvantage of these algorithms is the use of approximation to describe the laser beam distribution. Within the framework of the project, the algorithm will be developed, which will be realized on the optical-electronic scheme. The main characteristic of this algorithm is that it operates at the hardware level and through it we can manage the high-sensitive nitrogen laser NL-100 and monochromator. The monochromator gives a picture in the Fourier plane. This scheme allows to use the laser with any initial distribution of intensity. The algorithm will allow us to select the phase function to allocate laser intensity in order to minimize the errors when forming a diffractive picture of the output signal, and therefore we assume that its use can increase the functioning of the phase spectrofluorometer.

The Einstein-Fokker-Kolmogorov's equation enables us to calculate the angular and linear inclination from the source direction [7]. So, while propagating waves in the chaotic inhomogeneous media, the absorption of the energy of electromagnetic waves significantly influences on the statistical characteristics of the scattered radiation. The absorption may cause the deformation of the power of radiation spectrum while discussing the asymmetric

problem [8]. The salvation of such type problems has scientific and practical importance. Nowadays, there is not a universal analytical method for solving such problems and therefore, we can get the information on the scattered radiation by applying the figural methods or from the experiment itself.

It turned out that partial spatial coherence of the source reduces the scintillation noise. The function of Gaussian partial coherent source is studied in the work [9]. In conditions of the weak and strong turbulence the analytical expression of correlation function of the space-part coherent intensity was obtained in the work [10], where the general principle of Hugens-Frannel and the general solution of Relay-Zommerfeld were used. In the work [11] Ritov's method is used, in conditions of weak turbidity atmosphere.

Let's say, on the $z=0$ plane the primary $s_0$ field statistics are given, i.e. its moments (coherence function) are given. It is necessary to find out how these functions are changing away from the $z=0$ plane, if on the way the field is transformed (for example, the wave is going through a diaphragm, lens or other).

Formally this task is solved easily: If it is known how the determined (totally coherent) wave changes, then it is enough to make an ensemble averaging of the determined solution of $s_0$ field. But this method, as a rule, reduced to difficultly calculating integrals. For example, when calculating the relative fluctuations of intensities $\sigma = < I^2 - < I^2 >> / < I^2 >$ (the same as the "Scintillation index") it is necessary to calculate the eight-fold integral, which is practically impossible to be calculated even in the case of simplified model. The simplified marginal model implies that a flat wave $e^{ikz}$ falls on the layer, directly on the other side of the screen $s_0 = \exp(ikz + i\Psi)$, where $\Psi(x,y)$ is the random phase. Knowledge of phase statistics on the screen determines the field statistics on $z=0$ flatness. The "system" which "transforms" the field out of the screen is just a free space in the given case. As a result of diffraction, the wave, which passes through the chaotic phase screen, is experiencing fluctuations. However, the intensity of the phase screen is permanent (Fig. 2).

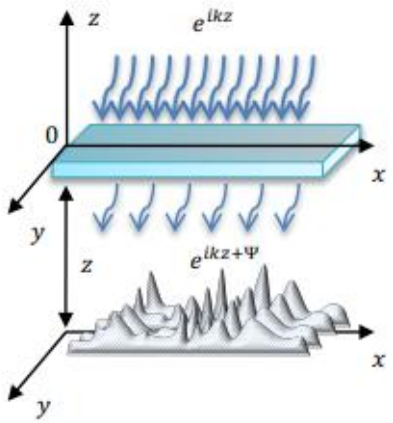


***Fig 2.*** *Distribution of wave $I(x)$ intensity via random phase screen*

Suppose that the statistics of the incident laser signal on the detector is known ( $s(t)$ ). If the probability distribution of the signal on the detector is also given by W (s), then the average value of the signal at the output of the detector is determined by:

$$\langle f(s)\rangle = \int_{-\infty}^{+\infty} f(s)W(s)ds = \lim_{T\to\infty}\frac{1}{T}\int_{-T/2}^{T/2} f\left(s(t)\right)dt,$$

$$W(f) = W(s)\frac{ds}{df}, \qquad (8)$$

where $W(f)$ - is the distribution of the signal at the output of the detector. The signal power spectrum or auto-correlation function cannot provide complete information about the process of scattering, but these values are subject to experimental measurement, therefore, the theoretical and experimental measurement of these parameters may become the basis for creating an adequate theoretical model. From this perspective, the first and second order statistical moments are presented as experimental measurable physical values on the basis of the correlation functions of the scattered signal and intensity:

$$g^{(1)}(\tau) = \frac{\langle s^+(0)s^-(\tau)\rangle}{\langle I\rangle^2}, \quad g^{(2)}(\tau) = \frac{\langle I(0)I(\tau)\rangle}{\langle I\rangle^2}, \qquad (9)$$

Where, $I(t) = s^+(t)s^-(t)$ - represents a magnitude that is recorded by a detector. In the quantum-mechanical point of view, we can say that the detector, which works on photon registration (through photo multiplier and photodiode), records this value. $s^+(t)$ and $s^-(t)$ represents the signal components that correspond to positive and negative frequencies and are determined by the Fourier series:

$$s(t) = \sum_{\omega>0} a_\omega^* e^{-i\omega t} + \sum_{\omega\geq 0} a_\omega e^{-i\omega t} = s^+(t) + s^-(t),$$

$$a_\omega = \frac{1}{T}\int_{-T/2}^{T/2} s(t)e^{-i\omega t} = a_{-\omega}^*. \qquad (10)$$

It is noteworthy that from $g^{(1)}(\tau)$ and $g^{(2)}(\tau)$ statistical moments only the second order statistical moment $g^{(2)}(\tau)$ is to be measured on the detector. That's why, the matter of finding the connection between $g^{(2)}(\tau)$ and $g^{(1)}(\tau)$ statistical moments is an urgent issue. This connection was found for statistically independent random variables on the basis of probability theory and was brought to the expression that is a well-known ratio and which allows the first-range spectral characteristics to be calculated by the simplest spectral characteristics of the second order:

$$g^{(2)}(\tau) = < I(t)I(t+\tau) > = < I >^2 \left(1 + \left|g^{(1)}(\tau)\right|^2\right). \qquad (11)$$

Similar calculations were conducted for a specific task when the scattered field:

$$s^+(t) = s_0 \exp\left[-i\left(\omega_0 t + \varphi_0(t)\right)\right] + f(t)s_1 \exp\left[-i\left(\omega_1 t + \varphi_1(t)\right)\right]$$

and primary source field were radiated from the same point of space and the intensity correlation function was calculated for Lorenz: $g_L^{(1)}(\tau) = \exp(-2\alpha\tau)$ and Gaussian: $g_G^{(1)}(\tau) = \exp(-\beta^2\tau^2)$ forms:

$$g^{(2)}(t;T) = 1 + \frac{sh^2(\alpha\tau)}{(\alpha\tau)^2}\exp(-2\alpha\tau), \quad \tau > T, \qquad (12)$$

$$g^{(2)}(t;T) = 1 + \frac{\exp\left[-\beta^2(\tau^2+T^2)\right]}{\beta^2T^2}sh(2\beta^2\tau T) +$$

$$+ \frac{1}{\beta T^2}\left\{(\tau+T)erf\left[\beta(\tau+T)\right] + \right. \qquad (13)$$

$$\left. + (\tau-T)erf\left[\beta(\tau+T)\right] - 2\tau erf(\beta\tau)\right\}.$$

On Fig. 3 is shown the distribution of the signal at the input and output of the square detector.

Based on the first and second orders of the laser radiation scattered from the random phase screen, can be received:

$$< I(\theta;t) > = \pi^2 W_0^2 \left|E_0\right|^2 \times$$

$$\times \int_0^\infty dr\, r\, J_0(kr\sin\theta)\exp\left\{\left[-\bar{\phi}^2\left(1-\rho(r)\right)\right] - \frac{r^2}{W_0^2}\right\}. \qquad (14)$$

$$\frac{< I^2 >}{< I >^2} = 2 - \frac{2l^2}{W_0^2} + \frac{l^2\bar{\phi}^2}{4W_0^2}\exp\left[\frac{k^2l^2\sin^2\theta}{4\bar{\phi}^2}\right]. \qquad (15)$$

when $l/W_0 \to 0$, $< I^2 > / < I >^2 = 2$, that is characterized to a Gaussian statistics. When $l \ll W_0$ the distribution is significantly different from Gaussian and the existence of $\bar{\phi}^2$ circumstance, which is quite large in terms of access. Finally, when $l \ll W_0$ the second order moment may be more than 2 if $\bar{\phi}^2$ is a big enough

value. Moreover, this effect will increase even more by increasing $\theta$.

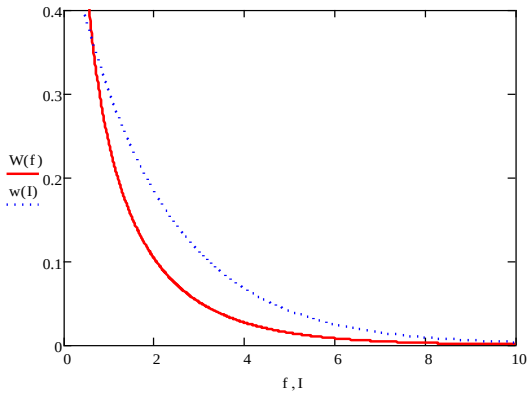


***Fig. 3.*** *Distribution of Gaussian signal at the input and output of square detector.*

| № | Simple | Parameters of Fluorescence excitation spectrum | | | | | | | | |
|---|---|---|---|---|---|---|---|---|---|---|
| | | Excitation by UV light ( 390 nm) | | | Excitation by Red light (660 nm) | | | Excitation by Green light ( 470 nm) | | |
| | | BASE | Power Spectral Density - PSD | Width | BASE | Power Spectral Density - PSD | Width | BASE | Power Spectral Density - PSD | Width |
| 1 | **Sea water** | 1837.4 | 134137.79 | 13.51 | 2069.2 | 1736774.15 | 26.56 | 2001.00 | 2168830.8 | 33.02 |
| 2 | **Vinegar** | 1766.8 | 10888.11 | 33.5 | 2176.4 | 1485608.45 | 25.35 | 2168.6 | 1649046.07 | 33.31 |
| 3 | **Mineral water** | 1887.6 | 17618.48 | 18.62 | 2149.4 | 112147.34 | 28.67 | 1940.00 | 442933.54 | 31.33 |
| 4 | **Milk** | 1968.8 | 77010.83 | 14.23 | 2005 | 1830624.19 | 27.15 | | | |
| 5 | **Distillate** | 1883.2 | 16268.35 | 18.98 | 2138.4 | 26896.18 | 36.51 | 2071.8 | 57543.31 | 38.45 |
| 6 | **Drink water** | 1833 | 13478.5 | 21.17 | 2203.8 | 98305.21 | 28.96 | | | |

*Table 1.*

On Table 1 present some parameters of fluorescence excitation spectrum for simples such as: sea water, vinegar, mineral water, milk, distillate and drink water, when excitation leads by phase modulated light with different wave length (UV light – 390 nm; Red light – 660 nm; Green light – 470 nm). The parameters: Base – is intensity from zero stage still base stage of spectrum; PSD – is power spectral density light under the excitation spectrum; Width – is half width of the spectrum.

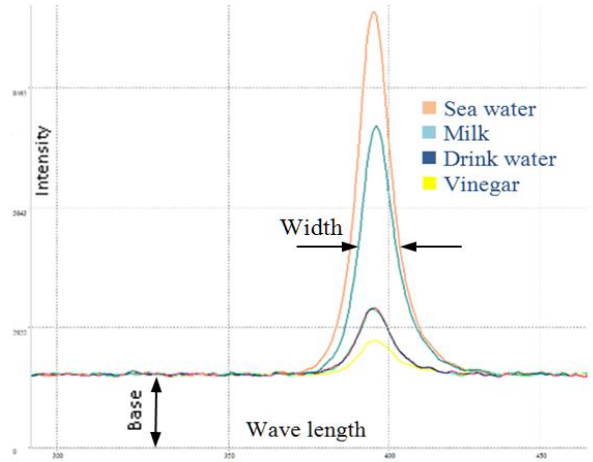


***Fig.4.*** *Excitation fluorescence spectrum of phase modulated UV light ( $\lambda = 390$ nm) of different simples*

Fig. 4. shows excitation fluorescence spectrum of phase modulated UV light via different simples, such as: sea water, milk, drink water and vinegar.

## 4. Conclusion

Measurements and experimental works were made to identify following values: the spectrum intensity of the fluorescence signal radiated from fluorofol, quantum yield, fluorescence decay time. Database was created for Hexane, distillate, drinking water, sea water, for the liquid crystals used in monitors and displays, etc. The environment, in general case, was represented by an optically solid "phase screen". The autocorrelator was managed with "sketch" written in special programming language (which represents a C clone). Signal/noise ratio exceeded 10000:1 value. The first and second order statistical moments of the correlative function of the laser radiation intensity scattered from the optically solid, random "phase screen" for Gaussian and non-Gaussian statistics were obtained.

Unfortunately, technical problems limit the creation of the tools through which it will be possible to verify modulation frequencies. As a rule, the number of modulation frequencies is limited with two or three fixed values. Only in certain favorable conditions, for fixed values of modulation frequencies, we can get fluorescence attenuation components in heterogenic system. Phase-modulated method is faster with milliseconds than photon counting method.

## 5. Acknowledge

Work was spent within the limits of the scientific projects: "Quantitative analysis of fluorescence characteristics of optically solid, random phase screen and spectral analysis of the statistical moments of the correlation function of the intensity of scattered laser radiation" (FR/152/9- 240/14 scientific supervisor Prof. Nugzar Gomidze), financed by SRNSF (Shota Rustaveli National Scientific Found, Georgia).

## *References:*

[1]. Birks J., Munro I. The Fluorescence Lifetimes of Aromatic Mole cules, Progress in Reaction Kinetics, vol. 4, Pergamon Press, Oxford, 196

[2]. Davitadze Z., Gomidze N., Makharadze K. Control Laser Spectrofluorimeter with Microcontrollers. Journal of Advanced Materials Research Vol. 590 (2012), pp. 201-205. www.scientific.net/AMR.590.206

[3]. Gomidze N., Jabnidze I., Makharadze K., Khajishvili M., Shashikadze Z., Surmanidze Z., Surmanidze I. Numerical Analyses of Fluorescence Characteristics of Watery Media via Laser Spectroscopy Method. Journal of Advanced Materials Research Vol. 590 (2012), pp. 206-211. www.scientific.net/AMR.590.201

[4]. Lakovich J. "Principles of fluorescence spectroscopy". Springer Science, 2006. p. 960.

[5]. Eisenthal K.B., Chem. Phys. Letters, 6, 155 (1970)

[6]. Misievich S.K., Skidanova R.V. Journal Computer optics and nanophotonics, pp. 269-281, 2017

[7]. Gomidze N.Kh., Jabnidze I.N., Surmanidze Z.J. Stroboscopic Method of Fluorescence Analyses of Optically Solid Media. 2016 IEEE 7th International Conference on Advanced Optoelectronics and Lasers (CAOL). September 12-15, Odessa, Ukraine, pp. 34-36, 2016.

[8]. Gomidze N.Kh., Makharadze K.A., Jabnidze I.N. Experiments for the Purpose of Studying Space-time Evolution of Various Forms of Pulse Signals in the Collisional Cold Plasma. International Journal of Physical and Mathematical Science,Vol: 11, No:8, pp.318-323, 2017. Scolar.waset.org/1307-6892/10007581.

[9]. Gomidze N.Kh., Khajishvili M.R., Makharadze K.A., Jabnidze I.N. , Surmanidze Z.J. About Statistical Moments of Scattered Laser Radiation from Random Phase Screen. International Journal of Emerging Technology and Advanced Engineering. ISSN 2250-2459 (ISO 9001:2008 Certified), Vol. 6, Issue 4, pp.237-245, 2016. www.ijetae.com.

[10]. Baykal Y., Plonus M. A., Wang S. J. "The scintillations for a weak atmospheric turbulence using a spatially partially coherent source", Radio science, Vol.18, 4, 551-556 (1983).

[11]. Korotkova O., Andrews L.C. "Speckle propagation through atmosphere turbulence: effects of partial coherence of the target", SPIE pr., 2002

# WIND POTENTIAL ANALYSIS FOR HAKKARI CENTRAL REGION

Emrah Harmanci[1], Sedat Yayla[1]
[1] Hakkari University Department of Electrical and Automation
[2] Yüzüncü Yıl University Faculty of Engineering Department of Mechanical Engineering

65080 Central, Van, syayla@yyu.edu.tr, emrahharmanci@hakkari.edu.tr

***Abstract**: In this study wind potential investigated for the region to the east of Turkey's Hakkari centers. The wind speed and direction information used in the study were taken from the measurement station belonging to the General Directorate of Meteorology in Hakkari Center. Data sets containing 5 year wind speed and wind direction between 2013 and 2017 taken from this measurement station were analyzed by the WASP program. The NASA SRTM data library in the WASP interface was used to create digital maps for the region. Regional barriers required for areas where wind potentials are searched and roughness maps were created using Google Maps. As a result of these analyzes, annual average wind speed value of 1.96 m / s and average power density of this region in Hakkari Center is calculated as 12 W / $m^2$. The prevailing wind direction belonging to this region has been identified as Southwest, but it has been found that this dominant wind direction changes with great proximity to the Southeast-Northwest sector interval on the South side.*
**Keywords:** WASP, WIND ENERGY, RENEWABLE ENERGY, WIND POTENTIAL

### *1.Introduction*

Nowadays, use of natural energy resources has become an area where human beings must rapidly turn due to the rapid depletion of fossil-based energy and the world's inability to carry human population in this direction. In this area, large investments are made in the world, and a large part of the energy needs of the metropolis and the industries are provided within this scope. Many recent studies have been carried out to investigate the sources of renewable energy and to determine the potentials of available resources.

Yayla S. (2005), Van Yüzüncü Yıl University used the WASP program to determine the Campus Area Wind Energy Potential. Şahin B. et al. (2005), wind energy in Turkey's eastern Mediterranean coast have used to determine the potential wasp. The average power density was determined to be 500 W / m2 at 25 m from ground level in many parts of this area. Sharma K. and Ahmed R.M. (2016), Suva and Kadavu in the Fiji Islands have tried to determine the wind energy potential. The dominant wind direction for both regions was found in the Southeast. Data analysis showed that the total wind speed in the region is about 3.5e6.35 m / s. Kazet M. Y. et al. (2016), have prepared a wind source map of Cameroon's Ngaoundere region. Various data types have been used for the study on climate, topography and roughness. Annual energy production for the region is calculated to be 5,985 MWh. Nouri A. et al. (2016), they have prepared a comparative methodology between the wind resources of two different regions in Morocco for the study of the wind farm potential. Himri Y. et al. (2010), using WASP, they performed a statistical analysis of wind speeds in Tindouf in Algeria. It was found that the mean wind speeds of the working area changed between 7.19-7.95 m / s and the annual values of k and c on the field changed between 2.85 and 3.23 and 8.0-8.9 m / s respectively. Bilgili M. et al. (2004), using the hourly wind data observed between 1997 and 2001 at the meteorological stations of Antakya and İskenderun regions, they determined the dominant wind direction, mean values, wind speed, wind potential and frequency distributions. The results are classified according to their height above the ground level. Boudia S.M. et al. (2016), calculated the potential of the wind energy over the Algerian region. Based on the Weibull function, annual mean wind speed was 2.42 m / s and annual mean power density was 49 W / m² in the analysis carried out at a height of 10 m in the meteorological station. Pusat Ş. (2017), has tried to determine the wind energy potential at Sakarya University. In the study, it was determined that the wind energy potential of the zone is generally low. Şahin B. and Bilgili M. (2009), have been studied wind characteristics to using WAsP at Belen Hatay in the south of Turkey. They are calculated as 7.0 m / s and 378 W / m2, respectively, with an average wind speed and power potential of 10 m above sea level. This study concludes that existing regions are suitable for wind power plantation and that building a wind farm in this region may be profitable. Hocaoğlu F.O et al.(2008), by using the WASP, Anadolu University in Eskişehir region has simulated the wind turbine using the data of wind speeds and directions measured and recorded from 2 Eylül Campus in 1 hour intervals. As a result of simulations, the possible energy production of the wind turbine considered was calculated as 849,421 MW/h.

## *2.Materials and Methods*

In this study, 11 wasp 275,000 population located to the east with Turkey's Hakkari using proğramı of the central district of the province of wind potential has been determined. The data used in this study to make measurements in this region of the Republic of Turkey, which is taken from the General Directorate of Meteorology observation station. The data taken from the measuring station consist of the values of wind speed and wind direction measured at an altitude of 10m from the ground hourly in the interval of 5 years between 2013-2017.




***Figure 1.** General Directorate of Meteorology Hakkari Metering Station.*

There are mountains over 3000 meters in altitude around the area where the measuring station is located. The altitude at which the measuring station is located is 1727 meters. Figure 1 shows a map of Google Earth. Numerical maps of the region used in the WASP program in the study were obtained from the SRTM Importer located in the WASP interface. The SRTM Importer draws data from the SRTM Database, a library of NASA-developed digital maps of all areas of the world. WASP licensing is sufficient for access to this library. Coordinate information of the station worked was taken from the site of General Directorate of Meteorology. When these geographic coordinates are entered in the Map Center Location section in the SRTM Importer section, numerical maps are obtained for a radius of 3 km around this coordinate. Land roughness information of the obtained maps comes with the map by entering Land Roughness value. However, these adjustments have been made using Google Maps in order to more precisely adjust the roughness information in the working regions. Area roughness and obstacle information are obtained by using images from Google Maps as a base in WASP Map Editor section.

The collected MGM data was edited with "WASP Climate Analyst 3" which is included in the WASP 11 version before the main program is transferred. Here, climate data with specific time series are analyzed and the main program is formulated as observed

climate data (.omwc). Crude data with time series were transferred to Climate Analyst 3 module in "csv" format.

Observed station data obtained from the MGM were entered into the program as 3 columns. In the first column, the time slice of the climate data is specified as year, month, day and hour. In the second and third columns, wind speed and direction information related to the measured time are included. After being transferred to the Wind Climate Analyst program, the data sets can be arranged according to the desired category. Here, speed, direction, time series are organized according to the category is organized.

After entering the data as in Figure 2, the "Observed Wind Climate File" (OMWC) was calculated. OMWC calculations have wind charts, statistical reports and wind speed histograms with parameters a and k for all sectors from 0-330 degrees.

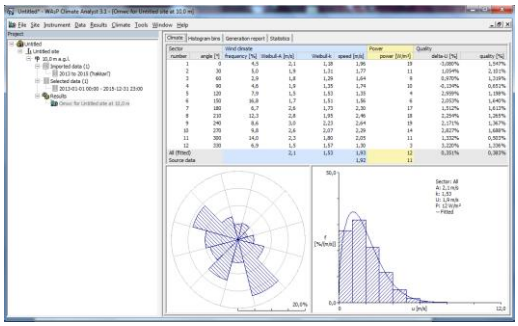

***Figure 2.*** *Creation of OMWC data sets with WAsP.*

The creation of the vector based maps belonging to the region has been done through WASP Map Editor 11. Map Editor allows you to download the topographic maps of the desired region by connecting to the topographic map database of the "SRTM .ver2 Database" created by NASA under the "import" section in the "files" section. In this study, land models belonging to the region were obtained from the SRTM Database by utilizing this feature. In order to obtain the data from the SRTM Database, as shown in Figure 3, the interface opened as DDD from the MGM site was entered as the center of the map and the location was entered in the "Map Center Location" field. Once the projection settings have been made, 2m spacing surface curves are provided with a 30 km area around the selected center. WaSP calculation modules have some limits. For vector maps, the sum of the number of points on the map plus three times the number of lines must not exceed 1,000,000 (Güzel B. 2012).

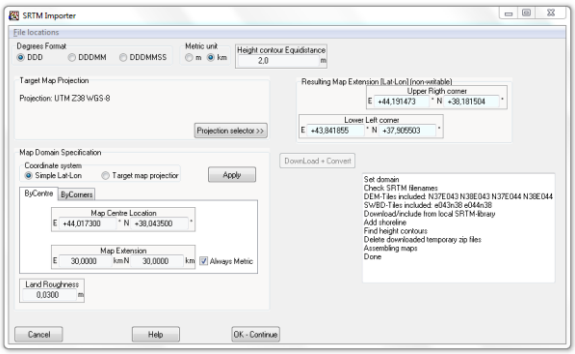


***Figure 3.*** *Topographic data generation from the SRTM Database.*

The surface roughness limits for the maps obtained for the regions were obtained using images obtained from Google Earth. The borders of areas with roughness values in the Google Earth interface are surrounded by road lines, which are then transferred to the WASP Map Editor in ".kmz" format. Roughness values are defined in the line properties and areas with different roughness values are defined in the program.

The vector map and roughness boundaries were merged into a single Map file and then saved in the ".map" format to be transferred to WASP 11. Observed climate data (.omwc) and surface map (.map) files were transferred to WASP 11 program.
When the observed climate data is transferred to the WASP, the UTM coordinate information of the station from which the measured values are received is being sought. Geographic coordinates obtained from stations belonging to the MGM were converted to UTM format, and then the coordinates of the metering station were entered.

After the transfer operations were completed, "Vestas V52 850 kW" was selected from the ready turbine models that came with the WASP program and the wind fields belonging to the region were created. Coordinate information of the wind field in UTM format should be entered when the turbine site is created as it is in the transfer of Observed Climate Data. After these operations are completed, the measurement station and the wind field are formed on the Vector Map.

After these processes are completed, a potential map has been created that allows us to read the potential distribution of the region with the aid of the color scale. The potential distributions of the region in the potential map show the power density of the regions in each sector. This map provides the most advantageous points for establishing a turbine site according to the potential density of the zone.

## *3.Result and Discussion*

In the study, wind atlases and potential maps were created using the WASP program to determine the wind potential of the region. For this, the data from the MGM measurement stations belonging to the studied regions were transferred to the WASP Climate Analyst module to obtain the wind skip and wind gauge graphs. The resulting omwc file was then transferred to WASP11 with surface maps from the SRTM Database and environmental barrier information was added. All zone environmental obstacles have been obtained using Google Maps. The graph of the wind skip obtained by transferring the data from the MGM to the WASP Climate Analyst program is shown in the following figure x. In this graph, mean wind speed value, weibull parameters and wind power values calculated for the square meter area are observed.

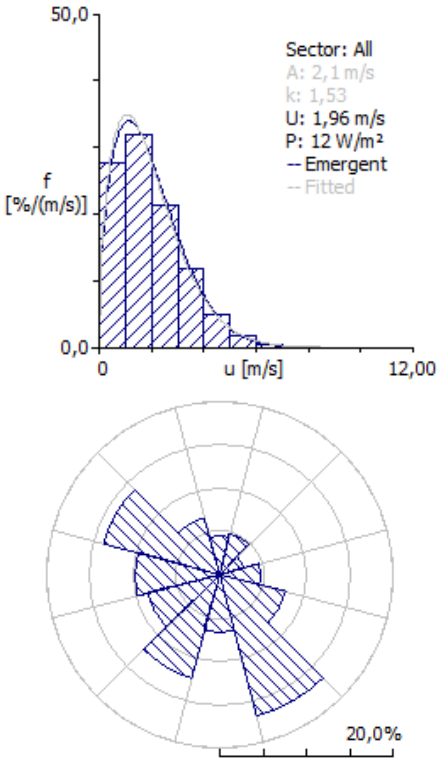

***Figure** Грешка! В документа няма текст със зададения стил.. Observed wind climate data and wind velocity histogram of Hakkari central station.*

The graphics are arranged to determine the wind potential of the 3 km area around the metering station. This does not cover the whole of the region studied. It is to create a system that can analyze the whole region that needs to be done. For the MGM station obtained in the study with data from the MGM and the area within 3 km of the coverage area, the wind is very low as seen from the graphs of potential. At the same time, as seen in the graph of wind gusts, the direction of the wind in the region varies from south to south in the clockwise Southeast and Northwest sectors, with very close violence. This indicates that the region has a turbulent wind blowing structure. The active dominant wind direction in this region can be seen in the wind rose in the graph of Sector 5 at 150 ° in the southeast direction. The average speed value, mean power density, wind speed frequency and wind frequency frequency belonging to this region are shown in the table below.

***Table 1.** Observed climate data for measurement stations.*

| Station | A (m/sn) | k | U(m/sn) | P (W/m$^2$) |
|---|---|---|---|---|
| Hakkari Station | 2,1 | 1,53 | 1,96 | 12 |

The ".omwc" file created after the calculation of the observed climate data in the Wasp Climate Analyst program has been transferred to the WASP 11 program. In the WASP 11 program, environmental obstacles, turbine selection and potential mapping of the region have also been carried out. The environmental barrier was created using Google Maps.

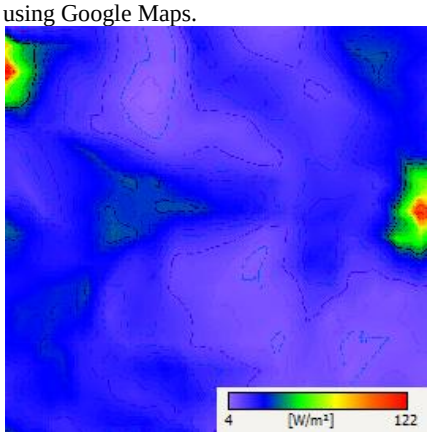


***Figure 5.** Wind potential distribution maps of MGM Hakkari Central Station.*

Turbine selections were calculated in accordance with the calculated wind force power density and the selections were concluded accordingly. Finally, wind simulation is performed on the vector maps obtained from SRTM Databese under WASP Map Editor, and wind potential maps of the regions shown in the following figure x are created. In these maps, the area around the station can be observed with the aid of the color scale. As can be seen from the maps, some areas in the eastern and southeastern regions of the Hakkari metering station are estimated to have wind potentials of around 152 W / m2.

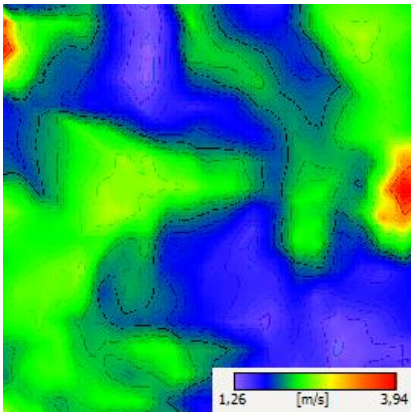


***Figure 5.** Wind speed distribution maps of MGM Hakkari Central Station.*

When the obtained potential maps and wind rose graphs are examined, the results obtained from the wind potential and wind roses are obtained for the Hakkari Central Station, which is shown in Table 2. According to this, it is seen that the area where Hakkari Central Station is located is in a medium level in terms of wind potential. When the theoretical results obtained in the analysis with WASP showed conformity to the Weibull distribution (Yayla S. 2005), it was tried to determine the wind speed potentials at various altitudes for Hakkari Central Station. The mean wind speed for this study and the mean and maximum wind potential results are shown in the table below for 10, 30, 50, 80 and 100 meter heights.

***Table 2.** The results of wind gulness and potential atlas of Hakkari Central Station.*

| Station | Mean Wind Speed (m/s) | Wind Potential (W/m$^2$) | | Dominant Wind Directions |
|---|---|---|---|---|
| | | Mean | Maximum | |
| Hakkari Center 10m | 2.07 | 19 | 122 | Southeast |
| Hakkari Center 30m | 3.00 | 50 | 177 | |
| Hakkari Center 50m | 3.39 | 64 | 197 | |
| Hakkari Center 80m | 3.88 | 90 | 241 | |
| Hakkari Center 100m | 4.11 | 105 | 262 | |

The wind parameters obtained in the sectors according to the selected turbine are shown in Table 4 below. According to this, it is understood that the most successful sector in terms of annual wind production is the ninth sector with 240°.

Table 2. The results of wind gulness and potential atlas of Hakkari Central Station.

| Sektor | Angle | Frequency | Weibull-A [m/s] | Weibull-k | Speed [m/s] |
|---|---|---|---|---|---|
| 1 | 0 | 4.02 | 3.3 | 1.44 | 2.96 |
| 2 | 30 | 5.56 | 4.2 | 1.55 | 3.78 |
| 3 | 60 | 5.67 | 3.7 | 1.56 | 3.35 |
| 4 | 90 | 6.86 | 2.6 | 1.60 | 2.36 |
| 5 | 120 | 7.35 | 1.8 | 1.88 | 1.62 |
| 6 | 150 | 9.21 | 1.9 | 1.82 | 1.65 |
| 7 | 180 | 7.87 | 2.1 | 1.79 | 1.91 |
| 8 | 210 | 12.29 | 5.0 | 2.19 | 4.41 |
| 9 | 240 | 14.04 | 6.4 | 2.48 | 5.64 |
| 10 | 270 | 13.87 | 5.3 | 2.28 | 4.70 |
| 11 | 300 | 8.89 | 3.8 | 2.18 | 3.36 |
| 12 | 330 | 4.38 | 3.3 | 1.75 | 2.96 |

## *4. Results*

As a result of this work, it has been determined that this measuring station in the center of Hakkari and the area of 3 km radius around it are not suitable for wind farm installation. As can be seen from the wind turbine belonging to the region, the dominant wind direction is determined as Southeast. The wind speed in the region is 1.96 m / s and the power density is 12 W / m2. The area is very mountainous and there is a pitched area between the mountains and peaks that cut the wind speed of the metering station. The potential to be investigated in the higher parts of the hilly and mountainous areas surrounding the center of the Hakkari Center, which is outside the coverage area of this measurement station that needs to be done, and where the wind speed is not exposed to high obstacles. Since there is no metering station in these regions, the wind could not be calculated for the center of the potential center of the province. In order to be able to determine the general potential of the zone at every point, it is necessary to be able to determine the wind speed and direction at the points to be determined before being dependent on the measurement stations.

## *5. Acknowledgement*

This study was supported by the project of FYL-2017-6004 by Yüzüncü Yıl University Scientific Research Projects Coordinator.

## *6. Resources*

Bilgili, M., Şahin, B., Şimşek, E., 2010. Ege Bölgesindeki Toprak Sıcaklıklarının Yapay Sinir Ağları Yöntemi İle Belirlenmesi, Isı Bilimi Ve Tekniği Dergisi 30(1): 121-132.

Boudia, S.M., Berrached, S., Bouri, S., 2016. On the use of wind energy at Tlemcen, North-western region of Algeria, Energy Procedia 93: 141-145.

Güzel B., 2012. Açik Deniz Rüzgar Enerjisi, Fizibilite Adimlari Ile Bozcaada Ve Gökçeada Örnek Çalişmasi (Yüksek Lisans Tezi), İTÜ, Enerji Enstitüsü, Sarıyer, İstanbul.

Himri, Y., Himri, S., Stambouli, A.B., 2010. Wind power resource in the south-western region of Algeria, Renewable and Sustainable Energy Reviews 14: 554–556.

Hocaoğlu F.O., Kurban M., Filik, Ü.B., 2008. WAsP Yazılımı İle Rüzgar Potansiyeli Analizi Ve Uygulama, Anadolu Üniversitesi İki Eylül Kampüsü Mühendislik-Mimarlık Fakültesi 26555, Eskişehir.

Kazet, M.Y., Mouangue, R., Kuitche, A., Ndjaka, J.M., 2016. Wind energy resource assessment in Ngaoundere locality, Energy Procedia 93: 74 – 81.

Nouri, A., Babram, M.A., Elwarraki, E., Enzili, M., 2016. Moroccan wind farm potential feasibility. Case study, Energy Conversion and Management 122: 39–51

Pusat, Ş., 2017. Sakarya Üniversitesi için rüzgâr enerjisi potansiyel belirleme çalışması, Pamukkale Universitesi Mühendislik Bilim Dergisi 23 (4): 352-357.

Sahin, B., Bilgili, M., Akilli, H., 2005. The wind power potential of the eastern Mediterranean region of Turkey, Journal of Wind Engineering and Industrial Aerodynamics 93: 171–183.

Sahin, B., Bilgili, M., 2009. Wind Characteristics and Energy Potential in Belen-Hatay, Turkey, International Journal of Green Energy, 6: 157–172.

Sharma, K., Ahmed, M.R., 2016. Wind energy resource assessment for the Fiji Islands: Kadavu Island and Suva Peninsula, Renewable Energy 89: 168-180.

Yayla, S., 2005. Van Gölü Kıyısının Rüzgar Enerjisi Potansiyelinin Belirlenmesi (Yüksek Lisans Tezi), YYÜ, Fen Bilimleri Enstitüsü, Merkez, Van.

# PRODUCTION PROCESS OF POWDER PERMEABLE MATERIALS MADE OF SPHERICAL BRONZE POWDERS BY PRESSING

## ПРОЦЕСС ПОЛУЧЕНИЯ ПОРОШКОВЫХ ПРОНИЦАЕМЫХ МАТЕРИАЛОВ ИЗ СФЕРИЧЕСКИХ ПОРОШКОВ БРОНЗЫ МЕТОДОМ ПРЕССОВАНИЯ

Prof., Dr. Eng., Cor. Member of NAS of Belarus Ilyushchanka A.[1, 2],
PhD of Eng., Doc. Kusin R.A.[3], Head of the Lab. Charniak I.N.[2], Res. Kusin A.R. [2], Res. Zhehzdryn D.I.[2]
State research and production powder metallurgy association[1] – Minsk, Republic of Belarus
State Scientific Institution "Powder metallurgy institute" [2] – Minsk, Republic of Belarus
Belarusian state agriculture technical university [3] – Minsk, Republic of Belarus
E-mail: alexil@mail.belpak.by, 19081877@mail.ru, irinacharniak@tut.by, 2312444@mail.ru, varchavskaia@mail.ru

***Abstract:*** *The process of producing powder permeable materials made of spherical bronze powders by tin-phosphorous pressing method has been investigated. A technique for producing experimental samples based on the granulation of powders by a pore-former has been described. The technology is simple to carry out and it does not require complex equipment. Products have a satisfactory set of properties.*

***KEYWORDS****: POWDER PERMEABLE MATERIALS, PORE-FORMER, GRANULATION, PRESSING, PROPERTIES*

## *1. Introduction*

The methods for powder permeable materials molding are divided into two groups: and applying pressure. As a rule, when using spherical powders for the production of porous permeable products, a molding method without applying pressure is used. The simplest method is the sintering of a freely poured powder [1, 2].

Compared with non-spherical powders, products made of spherical powders have a more uniform porosity and high permeability [3, 4]. For the production of permeable materials, spherical powders of tin-phosphorous bronze of grade BrO10F1 are most widely used, which are well sintered by the method of free pouring at relatively low temperatures (790-870 °C) in reducing and neutral atmospheres or in a vacuum. The products from these powders have a high complex of filtering and physical-mechanical properties. A tooling from corrosion-resistant steels of grades X18H10, X18H9, X30 is used for sintering the products. One set of tooling can withstand from 50 to 100 cycles of sintering. However, corrosion-resistant steels are poorly treated and expensive. This significantly affects the cost of porous products.

Therefore, it seems relevant to consider the possibility of producing porous filter materials made of BrO10F1 powder by pressing, secondly, to justify the possibility of producing powder permeable materials from the powders with a fraction of 200-315 μm with properties corresponding to materials produced from powders with larger fractions.

However, molding with applying pressure is mainly used in the manufacture of products made of powders with a non-spherical shape particles, and does not require the introduction of binding materials.

The purpose of this work is to study the process of producing powder filter materials by pressing granular spherical bronze powders of grade BrO10F1 by means of a pore-former.

## *2. Research material.*

It is common knowledge that spherical powders are not pressed without special additives (binders), which can be used as pore-formers and plasticizers [2, 5]. In this paper, the molding capacity of a spherical powder of tin-phosphorous bronze is ensured by granulating the metal powder by a pore-former, i.e. carbamide (urea, $CO(NH_2)_2$). It follows from the works [6-10] that carbamide has a number of advantages: it does not contaminate products with decomposition impurities; it is well soluble in water; it is widely used. It should be noted that carbamide was previously used as a filler. Its use as a binder in the molding of powder permeable materials from spherical powders of tin-phosphorous bronze by the pressing method has not been previously met.

Samples in the form of a disk with a diameter of 30 mm and a thickness of 3 mm were produced by a pressing method to study the process of producing powder permeable materials from spherical bronze powders [11-13]. Bronze powder of grade BrO10F1 of fraction (minus 315+200) μm, carbamide powder $CO(NH_2)_2$ (analytic grade) were used as initial materials. The process of producing the samples included the preparation of a charge, granulation, pressing and sintering.

Granulation was carried out by carbamide dissolution in distilled water, mixing the resulting solution with fine-dispersed bronze, drying the charge in CNEF 4.5.4.5/34-1 drying oven at a temperature of 60-80 °C with constant stirring. The formed granules were scattered on a device of grain composition 029 with separation of the required fractions of the obtained charge (bronze powder granulated with a pore-former carbamide).

After pressing, the samples were sintered for 1 hour in an endogas atmosphere in a laboratory electric furnace with preliminary removal of carbamide by withstanding at a temperature of 250 °C for 0.5 hour. The porosity in accordance with GOST 18898-89, the coefficient of permeability in accordance with GOST 25283-93, the pore sizes in accordance with GOST 26849-86 and the ultimate shear stress, calculated by dividing the shear force by the area of the sheared surface, were determined in the produced samples.

## *2. Experiment results and discussion*

It is obvious that the main technological factors influencing the properties of the produced powder permeable materials during the preparation of the charge are the size of the initial bronze powder $D_p$ and the volume ratio of carbamide (pore-former) and bronze powders $V_{por}/V_{br}$. As noted above, a fraction of the bronze powder (minus 315+200) μm was chosen for the study. The charge was prepared in five compositions: $V_{por}/V_{br}$: 0.1; 0.3; 0.6; 0.9; 1.2, since at a ratio of less than 0.1, the pore-former does not have a significant effect on the structure of powder permeable material, and at a ratio more than 1.2, the strength of the produced powder permeable materials is significantly reduced. When molding, i.e. static pressing in a mold, the key factor is the pressing pressure *p*. A study of the morphology of the surface of particles of bronze powder and granules of granular bronze powder by a carbamide pore-former was carried out using MIRA scanning electron microscope with EDX X-act X-ray microanalyzer, Tescan, Czech Republic. The microscope is shown in Figure 1.



***Fig. 1*** *MIRA scanning electron microscope with EDX X-act X-ray microanalyzer, Tescan, Czech Republic*

Photographs of the morphology of the powder surface and granules are shown in Figures 2 and 3.

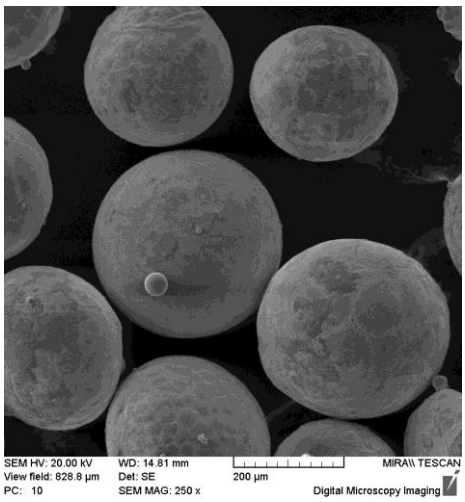


***Fig. 2*** *Photographs of morphology of the surface of bronze powder of brand BrO10F1 of fraction (minus 315+200) µm*

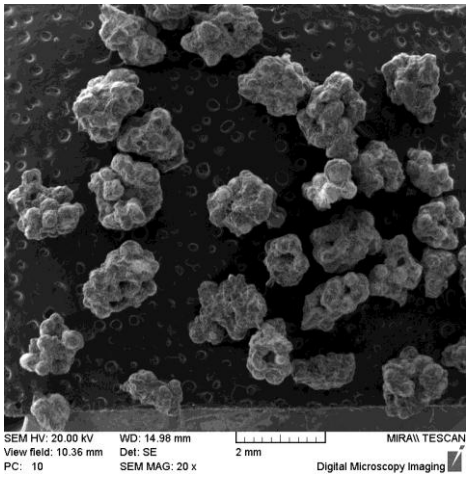


a)

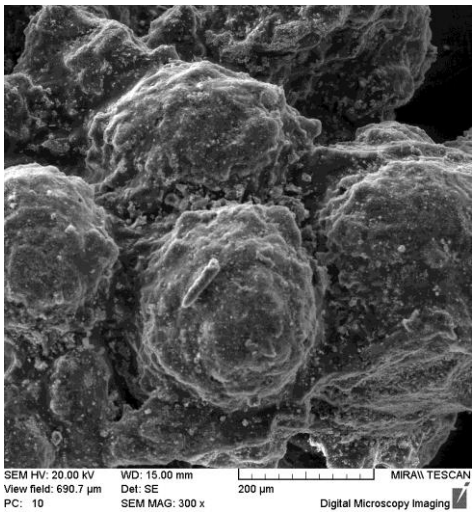


b)

*a) with increasing × 20; b) with increasing ×300*

***Fig. 3*** *Photographs of the morphology of the surface of particles of bronze powder granulated by a carbamide*

The pressing pressure, on the one hand, was chosen from the condition of achieving the strength of the compact, ensuring its safety during the preparatory work related to sintering (moving, placing in the boat, etc.); on the other hand, the porosity and coefficient of permeability are significantly decreased at high pressures making it unreasonable to use the resulting product as powder permeable material. Proceeding from this, the pressing pressure was chosen to be 50, 90, 130 MPa.

Figures 4-7 show the experimental dependences of P, k, $d_{pore}$, $\sigma_{av}$ on the ratio of urea volume to the volume of bronze powder at various pressing pressures.

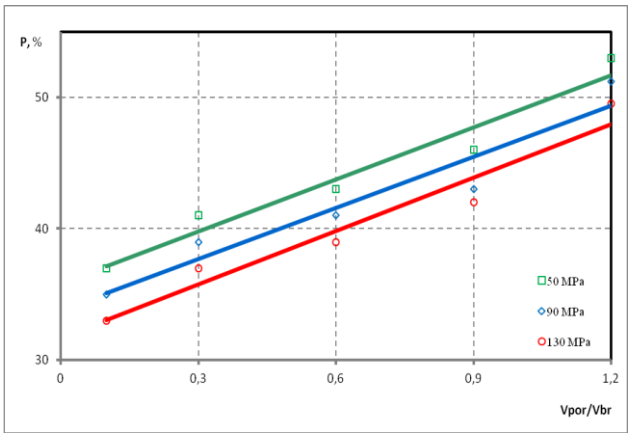


***Fig. 4*** *Dependence of the porosity on the volume ratio of the pore-former and the metal powder*

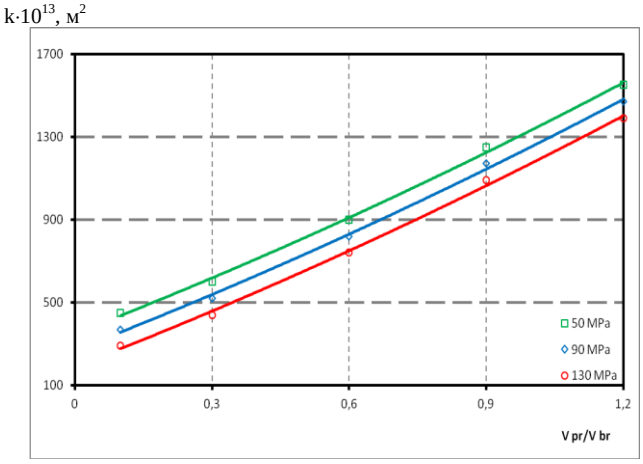


***Fig. 5*** *Dependence of the coefficient of permeability on the volume ratio of the pore-former and the metallic powder*

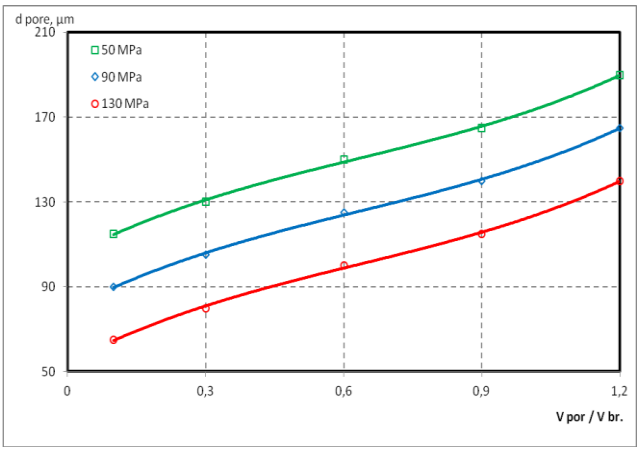


***Fig. 6*** *Dependence of the average pore size on the volume ratio of the blowing agent and the metal powder*

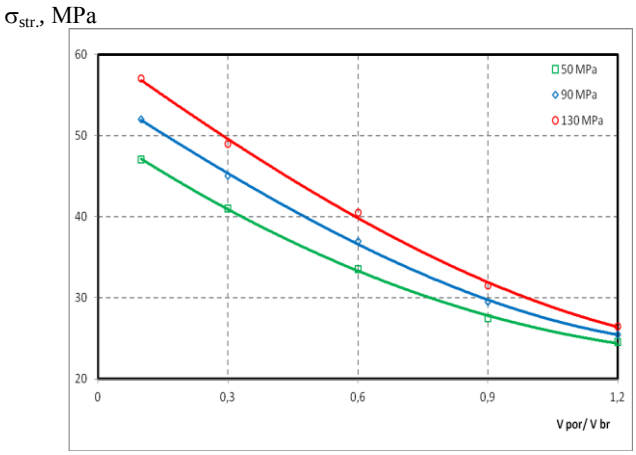


***Fig. 7*** *Dependence of the ultimate shear strength on the volume ratio of the pore-former and the metal powder*

The analysis of the obtained data in Figures 1-4 makes it possible to conclude that the use of the pore-former allows to significantly regulate the range of the main properties of powder permeable material: porosity from 0.32 to 0.52; average pore size from 60 to 197 μm; coefficient of permeability from $250\times10^{-13}$ to $1450\times10^{-13}$ $m^2$. It is obvious that the use of other fractions more extends this range.

Analysis of the photographs of the sample fractures (Figure 8) made by MIRA scanning electron microscope (Figure 1) has showed that the samples of powder permeable material made by pressing from the tin-phosphorous bronze powder of the fraction from 315 to 200 μm with different contents of the carbamide pore-former have a well developed biporous pore structure (Figure 8).

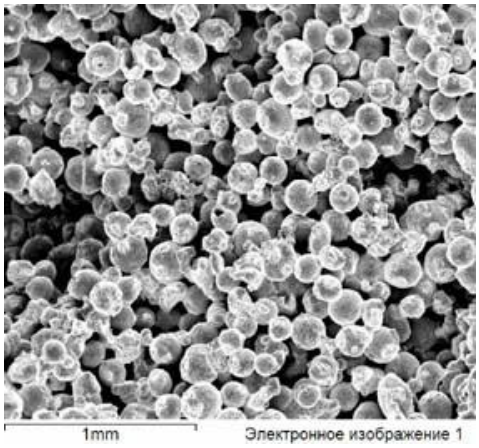


a)

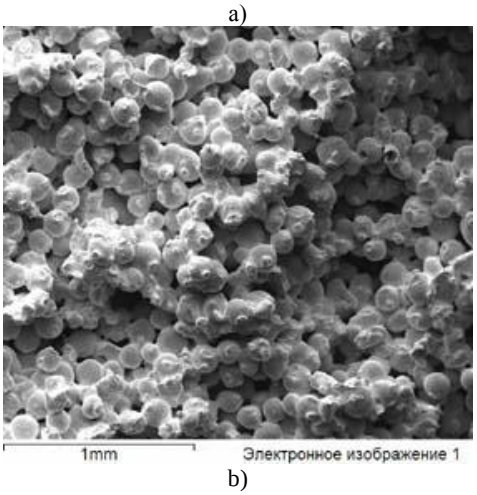


b)

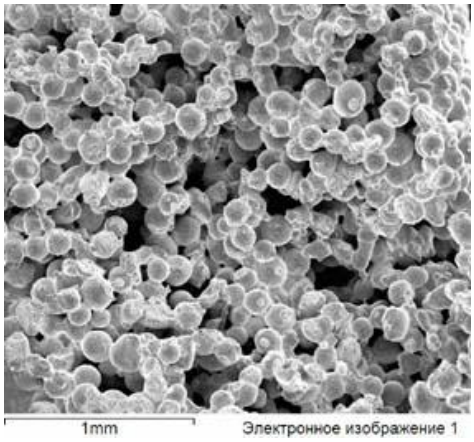


c)

a) $V_{por}/V_{br}$ = 0,3; b) $V_{por}/V_{br}$ = 0,6; c) $V_{por}/V_{br}$ = 1,2

***Fig. 8*** *Microstructure of the samples of powder filter material made of tin-phosphorous bronze powder of a fraction from 315 to 200 μm with different contents of carbamide pore-former at a pressing pressure of 90 MPa*

The most promising is the use of the developed method for mass pressing of small asymmetric products or long tubular filtering products by radial isostatic pressing. The latter is very difficult to produce by other methods, especially with a small diameter: rolling of plates in this case is impossible, and sintering in the mold is economically impractical and is related to unacceptable technological complications.

## *3. Conclusion*

As a result of the research, the process of manufacturing powder permeable materials was developed by pressing a granular spherical bronze powder of grade BrO10F1.

It is established that the pressing of a granular powder of spherical bronze makes it possible to produce powder permeable materials with a wide range of regulated properties.

## *4. References*

[1] Jones, V. Fundamentals of Powder Metallurgy, Moscow: Mechanical Engineering, (1965), pp. 31-48. (V. Jones). (in Russia).

[2] Vityaz, P. Filtering materials: properties, fields of application, manufacturing technology, Minsk: SRI PM with PP, (1999), p. 304 (P. Vityaz, V. Kaptsevich, R. Kusin). (in Russia).

[3] Belov, S. Porous materials in mechanical engineering, Moscow: Mechanical engineering, (1981), p. 248 (S. Belov). (in Russia).

[4] Fedorchenko, I. Powder metallurgy, Materials, technology, properties, fields of application, Reference book, Kiev, Naukova Dumka, (1985), p. 625 (I. Fedorchenko, I. Franzevich, etc.) (in Russia).

[5] Balshin, M. Scientific fundamentals of powder metallurgy and fiber metallurgy, Moscow, Metallurgizdat, (1972), p. 335 (M. Balshin). (in Russia).

[6] Kusin A. Optimization of the process of producing porous powder materials at the pressing of metal powders with pore-formers, New materials, equipment and technologies in industry, Materials of the Republican Sc.-Techn. Conf. of Post-graduate students, Undergraduates and Students, Mogilev, GUVPO Belarussian-Russian University, (2004), p. 46. (A. Kusin) (in Russia).

[7] Kostornov, A. Compaction features of metal powder mixtures with a pore-former, Powder Metallurgy, (1983), V.6, pp. 10-14. (A. Kostornov, L. Lunin, N. Fedorova, L. Chernyshev) (in Russia).

[8] Lunin, N. Effect of joint milling and mixing of a pore-former with a metal powder on the structure of a porous material, Powder Metallurgy, (1983), V. 4, pp. 15-18. (N. Lunin, V. Sheremet, A. Kostornov, N. Slaptsova). (in Russia).

[9] Bokan, G. Influence of a pore-former on the properties of porous powder materials made of corrosion-resistant steel powder, Powder Metallurgy, (1999), Issue 22, pp. 112-115. (G. Bokan, I. Valkovich, M. Kaptsevich, and etc.). (in Russia).

[10] Nekrasov, B. Fundamentals of General Chemistry, Vol. 1, 3rd ed., corrected, Moscow, Chemistry, (1974), p. 656 (B. Nekrasov). (in Russia).

[11] Kusin R. Powder of filtering materials gained from porogene granulated spherical powder of tin-phosphorus bronze by molding with the application of pressure, Powder Metallurgy, Republican interdepartmental collection of scientific works, Editorial Board: P. Vityaz (Ch. Ed.) and colleagues, Minsk, Belaruskaya Navuka, (2007), Issue 30, pp. 167-169. (R. Kusin and etc). (in Russian).

[12] Kusin R. Perspective methods for creating gradient permeable structures, Porous filtering materials: technologies and products thereof: Records of the IV International Symposium, Minsk, 30-31 October, 2011, Nat. Acad. of Sciences of Belarus. Editorial Board: P. Vityaz (Ch. Ed.) and colleagues. Minsk: Belaruskaya Navuka, (2011) pp. 81-91. (R. Kusin). (in Russian).

[13] Vityaz, P. Modern Processes of Producing Two-Layer Filtering Materials, Powder Metallurgy and Metal Ceramics, January 2014, V. 52, Issue 9-10, pp 514-522. (P. Vityaz and etc.).

# INVESTIGATION OF HARDENING PROCESSES OF CORROSION-RESISTANT COATINGS DEPOSITED BY A FLUX-CORED WIRE WITH NITRIDE-BORIDE ALLOYING

# ИССЛЕДОВАНИЕ ПРОЦЕССОВ УПРОЧНЕНИЯ КОРРОЗИОННО-СТОЙКИХ ПОКРЫТИЙ, НАПЛАВЛЕННЫХ ПОРОШКОВОЙ ПРОВОЛОКОЙ С НИТРИДНО-БОРИДНЫМ ЛЕГИРОВАНИЕМ

Prof. Dr. Econ. Kuznetsova O.[1], Prof. Dr. Eng. Eremin E.[2], Cand. Eng. Makarov V.[3],
graduate student Losev A.[4], graduate student Borodihin S.[5]
Faculty of Humanities Education [1], Machine-building institute [2,4,5], Faculty of Transport, Oil and Gas [3] – Omsk State Technical University, Russia

**Abstract:** *This study explores the metal of a coating deposited by a high-chromium flux-cored wire alloyed with a BN-$TiB_2$-$ZrB_2$ complex. We investigated the changes in the durometric properties and fine structure of the coating after tempering and subsequent quenching. It is shown that the hardening of the metal of such a coating after quenching consists in the formation of a complex composite structure with an iron-chromium martensitic matrix, a large amount of eutectic and particles of hardening complexes, which leads to an increase in hardness and wear resistance. It has been established that phase transformations in the metal of such a coating are caused by the formation of an eutectic component based on chromium and iron borides, a framework structure and a large number of dispersed titanium nitride particles up to 2.5 μm in size.*

***KEYWORDS**: SURFACING, FLUX-CORED WIRE, CHROMIUM STEEL, BORIDE COMPOUNDS, HEAT TREATMENT, MARTENSITE, HARDNESS, STRUCTURE, WEAR RESISTANCE.*

## *1. Introduction*

Different methods of coating application are important for increasing the group of characteristics of parts of machine-building production, determining their service life and reliability in operation. One of such methods of coating application, widely used at present, is the surfacing of working surfaces of parts with flux-cored wires.

Thus, for the surfacing of parts for various purposes in petrochemical production widely used flux-cored wires containing from 13 up to 25% chromium [1]. Using them makes it possible to obtain coatings with high corrosion resistance. However, such coatings have low abrasion resistance when working in friction conditions. At the same time, the introduction of various alloying elements into the flux-cored wires makes it possible to increase the hardness and wear resistance of the deposited coatings.

It is common knowledge that high and stable mechanical and operational properties of steels can be obtained by combining solid-solution hardening and hardening by second-phase particles (carbides, nitrides, borides, intermetallics) in an iron-based matrix. One of such effective methods of hardening the metal is alloying it with boron [2-4]. To achieve this, boron compounds such as ferroboron, boron carbide, chromium diboride, titanium diboride should be used when surfacing. Previous studies made by authors have established a positive effect of titanium and zirconium diborides on the wear resistance of chromium-nickel martensitic-aging steels surfaced with flux-cored wires [5-7].

A wide application for alloying austenitic and austenitic-ferritic corrosion-resistant steels has found nitrogen [8-10]. Nitrogen improves the ability of deformation hardening, significantly increases the wear resistance of steel and its ability to resist the spread of cracks. Nitrogen has also found application for alloying steels with a martensitic structure. Such a steel is stronger than the steel with carbon and it has a higher wear resistance values than, for example, the well-known Hadfield steel [8]. It should be noted that nitrogen is usually introduced into the melt by the use of nitrided chromium or ferrochrome.

The use of boron nitride for these purposes, which is an electronic carbon analogue due to the similarity of a number of properties, is also of great interest [11].

The authors have shown the perspective of surfacing with a flux-cored wire doped with a BN-$TiB_2$-$ZrB_2$ complex [7]. However, the carried out researches refer only to the metal coatings in the state after surfacing. At the same time, the hardness of such coatings is quite high, which makes it difficult to machine them. Therefore, it is required to conduct the tempering of the deposited metal, and then, after mechanical treatment, its quenching.

The hardening processes of this coating and its final properties have not been studied.

Thus, the aim of the work is to explore the changes in the durometric properties and fine structure of such a coating after tempering and subsequent hardening.

## *2. Objects and methods of research*

As the research object we chose the metal obtained by surfacing with a flux-cored wire containing 15% Cr, 0.5% BN, 1.25% $TiB_2$, 0.5% $ZrB_2$. The metal was studied after thermal treatment under the conditions established earlier: tempering at 800 °C for 2 hours and quenching at 1020 °C.

Surfacing was carried out on plates of St3 steel with a size of 200×50×10 mm with an experimental flux-cored wire of 2.4 mm diameter in argon in three layers. Surfacing mode: current strength 230 A; voltage 24 V; the rate of surfacing is 20 m / hr.

Metallographic studies of the deposited metal were carried out on an optical microscope AXIO Observer A1m (Carl Zeiss). The microstructure was detected by chemical etching in a reagent of the following composition: $CuSO_4$ – 4 g; HCl – 20 ml; $H_2O$ – 20 ml.

Durometric studies were carried out on metal samples after surfacing and thermal treatment with a hardness tester TK-2 by the method of Rockwell and microhardness tester Shimadzu HMV-2 by the Vickers method.

Electron microscopy examination was carried out with a raster-type electron microscope JEOL JSM-6610-LV with add-on device Inca-350 of energy-dispersive analysis (EDA).

Investigations of the fine structure of the metal were carried out on foils using a transmission electron microscope EMV-100L at an accelerating voltage of 100 kV.

## *3. Results of the experiments and discussion*

The metal of the coating obtained with a flux-cored wire having 0,5% BN, 1,25% $TiB_2$, 0,5% $ZrB_2$ in the state after surfacing has a hardness of 52-57 HRC starting from the second layer. The microhardness of the structural components of such a metal is 617-648 HV for the matrix, 764-847 HV for the eutectic and 1128-1247 HV for the strengthening phases [7].

It has been established that the microhardness of the structural components of such a surfaced metal after tempering of the coating under investigation has changed significantly (Fig. 1, Tab. 1).

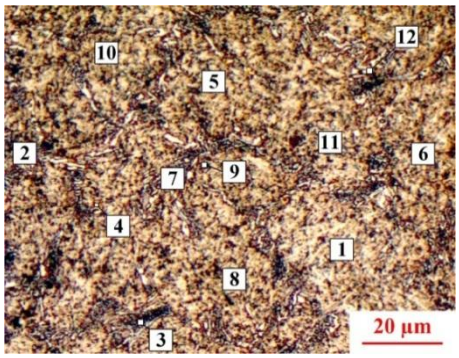


***Figure 1.*** *The microstructure of the coating metal and the measurement ranges of the structural constituents of the metal with borides after tempering*

*Table 1. Microhardness HV 0,01* and HV 0,05 of structural components of the metal with borides after tempering*

| Puncture № | HV |
|---|---|
| 1 | 357 |
| 2 | 608 |
| 3 | 629 |
| 4* | 783 |
| 5 | 386 |
| 6 | 366 |
| 7 | 603 |
| 8 | 408 |
| 9* | 593 |
| 10 | 371 |
| 11 | 384 |
| 12 | 675 |

As it can be seen, the microhardness of the structural constituents of the metal with borides after tempering has significantly decreased to 357-408 HV for the matrix, to 593-629 HV for the eutectics and to 675-783 HV for the strengthening phases.

After quenching, the deposited coating metal has a complex composite structure with a martensitic matrix, a large amount of eutectic and reinforcing phase particles. The hardness of such a metal reaches a maximum value of 54 HRC (Tab. 2).

***Table 2.*** *Hardness distribution over the cross-section of the coating metal with borides after quenching*

| Basic metal | Fusion zone | Hardness distribution over deposited metal layers, HRC | | | |
|---|---|---|---|---|---|
| | | 1 | 2 | 3 | 4 |
| 10 | 16,5 | 52 | 54 | 53 | 51 |
| 9 | 15,5 | 51 | 53 | 54 | 52 |

Dyurometric studies showed significant differences in the microhardness of the structural constituents of the coating metal after quenching (Fig. 2, Tab. 3).

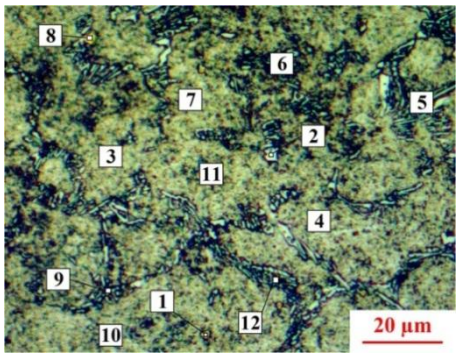


***Figure 2.*** *The measurement ranges and the microhardness values of the structural constituents of the metal with borides after quenching*

***Table 3.*** *Microhardness HV 0,01* and HV 0,05 of structural components of the metal with borides after quenching*

| Puncture № | HV |
|---|---|
| 1* | 1015 |
| 2* | 558 |
| 3 | 617 |
| 4 | 636 |
| 5 | 756 |
| 6 | 688 |
| 7 | 612 |
| 8* | 1045 |
| 9* | 882 |
| 10 | 656 |
| 11 | 624 |
| 12 | 841 |

The microhardness of the structural constituents of the metal deposited by the flux-cored wire with borides has increased significantly after quenching to 558-688 HV for the matrix, 756-882 HV for the eutectic and 1015-1045 HV for the hardening phases.

Electron microscopic studies of the structure make it possible to establish the laws of hardening of such a metal after its quenching. The results of transmission electron microscopy of the fine structure of the metal after quenching are shown in Fig. 3. Such a metal is a supersaturated α-solid solution with a developed and closed eutectic. Its structure characterizes by a large number, a special morphology and chemical composition of the eutectic and intermediate phases. In addition to the martensitic matrix, eutectics and strengthening phases take place. At high magnifications, the σ phase is detected (Fig. 3, b).



(a)

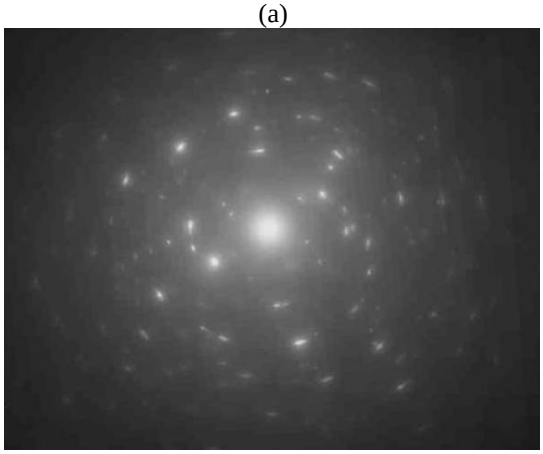

(b)

***Figure 3.*** *The microstructure of the coating metal deposited by the flux-cored wire with borides after quenching obtained by TEM: (a) fine structure (x 18000); (b) microdiffraction*

The results of scanning electron microscopy of the metal with borides are shown in fig. 4.

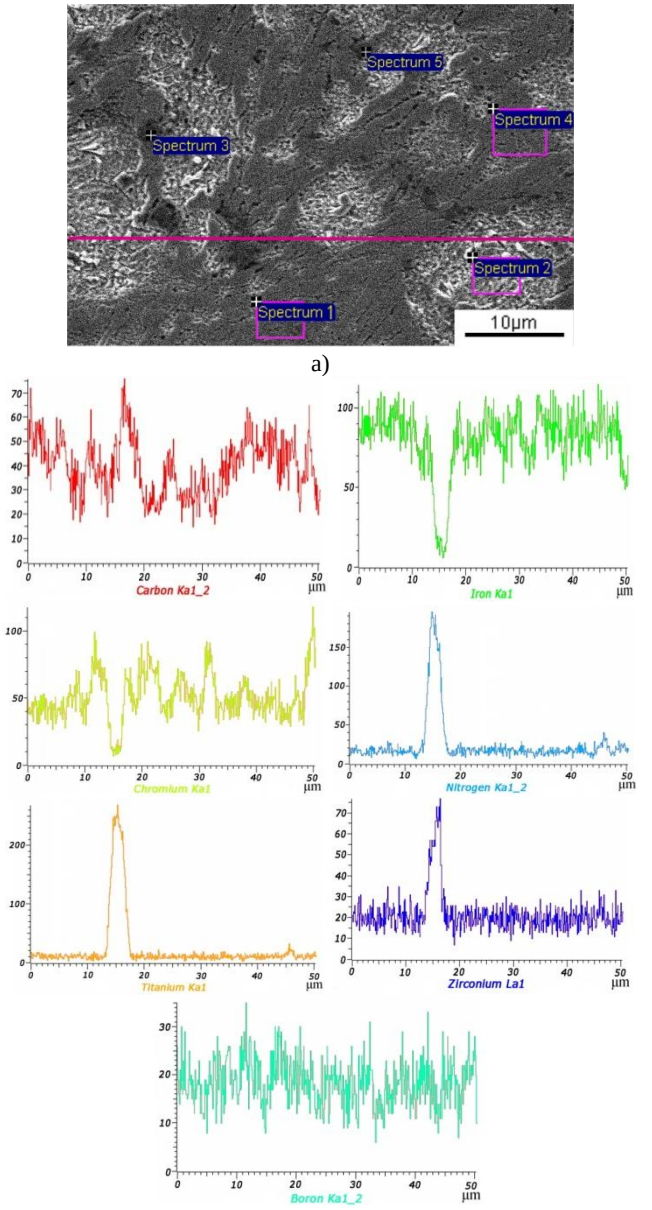


***Figure 4.*** *Scanning electron microscopy of the metal with borides: a) image of the microstructure with the scanning areas location; b) distribution of elements along the scan line*

From energy dispersive analysis data reflecting the quantitative distribution of elements along the cut of a straight line in the form of concentration spectrograms (Fig. 4, b) and spectra of the local point analysis (Table. 4) follows that the metal structure of represents the iron-chromium martensitic matrix with an eutectic component, formed on the basis of boride $(Fe, Cr)_2B$ having a skeletal character.

*Table 4. Chemical composition of coatings deposited with flux cored wire with borides*

| Spectrum | B,% | N, % | C, % | Cr, % | Fe, % | Ti, % | Zr, % |
|---|---|---|---|---|---|---|---|
| 1 | 18.55 | 0 | 13.22 | 17.26 | 50.97 | 0 | 0 |
| 2 | 0 | 0 | 17.55 | 12.21 | 70.24 | 0 | 0 |
| 3 | 0 | 14.65 | 18.39 | 8.86 | 36.24 | 18.59 | 3.27 |
| 4 | 16.08 | 0 | 11.81 | 18.51 | 53.60 | 0 | 0 |
| 5 | 0 | 13.18 | 15.45 | 6.35 | 49.82 | 14.56 | 0.64 |

This boride eutectic is characterized by 900-1050 HV micro-hardness and a large number of dispersed carbonitrides inclusions of the type (Fe, Ti, Cr, Zr)CN from 0.5 μm to 2.5 μm.

The research has shown that adding the high chromium flux-cored wire of the boron nitride, titanium diboride and zirconium diboride allows getting a new deposited composite metal. This metal has high hardness, which is due to the complex hardening owing to the formation of martensite in the carbonitride and carboborite phases matrix. In addition, carboboride eutectic located in the frame between the martensite crystals appears in the deposited metal structure, takes some load of the contact interaction and spreads it out on large surface area. This increases the tearing resistance of the deposited metal operating under abrasion conditions. However, zirconium and titanium form fine dispersed hardly soluble high strength nitrides that increase the wear resistance of the deposited metal, increasing viscosity and reducing fragility.

## *4. Conclusion*

The hardening of the metal of corrosion-resistant coatings deposited with a flux-cored wire alloyed with the $BN\text{-}TiB_2\text{-}ZrB_2$ complex after quenching consists in the formation of a complex composite structure with an iron-chromium martensitic matrix, a large amount of eutectic and particles of hardening complexes, which leads to an increase in hardness and wear resistance.

Phase transformations in the metal of such a coating are caused by the formation of an eutectic component based on chromium and iron borides, a framework structure and a large number of dispersed titanium nitride particles up to 2.5 μm in size.

The obtained results can be recommended for developing the technology for surfacing corrosion-resistant coatings on parts of petrochemical production.

## *5. Acknowledgement*

This research was made possible by a grant from the Russian Foundation for Basic Research (project No. 16-48-550523).

## *6. Literature*

1. (1979) The surfacing materials of the CMEA member countries: catalogue. Kiev, Moscow: VINITI.
2. Lyakishev, N. P., Pliner, Yu. L., Lappo, S. I. (1986) Boron-containing steels and alloys. Moscow: Metallurgiya Publ.
3. Zhong, L., Xiang, C., Yan-xiang L., Kai-hua, H. (2009) High boron iron-based alloy and its modification. In: J. of Iron and Steel Research, International, Issue16 (3), 37–42.
4. Raghavan, V. (2003) B – Cr – Fe – Ti (Boron – Chromium – Iron – Titanium). In: Journal of Phase Equlibria, Issue 24 (5), 459–460.
5. Yeremin Ye. N., Losev, A. S. (2014) Mechanical properties and thermal stability a maraging steel with borides, deposited with a flux-cored wire. In: Welding International, Issue 28 (6), 465–468.
6. Eremin, E. N. (2013) Using boride compounds in flux-cored wires for depositing maraging steel. In: Welding International, Issue 27 (2), 144–146.
7. Eremin E. N., Losev A. S., Borodikhin S. A., Ivlev K. Ye. (2017) Effect of the boride-nitride hardening on the structure and properties of chromium steel deposited with a flux-cored wire. In: Oil and Gas Engineering (OGE-2017) AIP Conf. Proc., Issue 1876, 020071-1–020071-6.
8. Kostina M. V., Bannikh O. A., Blinov V. M. (2000) Chrome-plated corrosion-resistant steel, alloyed with nitrogen, a new class of structural steels. In: J. Technology of metals, Issue 10, 2–12.
9. Schino A. Di, Barteri M., Kenny J. V. (2003) Grain size dependence of mechanical, corrosion and tribological properties of high nitrogen stainless steels. In: Journal of Materials Science, Volume 38, Issue 15, 3257–3262.
10. Spadele M. O. (2005) New nitrogen-containing austenitic stainless steels with high strength and ductility. In: Metallurgy and heat treatment of metals Volume 11 (605), 9–13.
11. Kurdyumov A. V., A. N. Pilyankevich, (1979) Phase transformations in carbon and boron nitride. Kiev: Naukova Dumka Publ.

# REGULARITIES OF ELECTRON-BEAM TECHNOLOGY INFLUENCE ON OPERATING CHARACTERISTICS OF OPTICAL ELEMENTS WITH NANO-DIMENSIONAL OXIDE COATINGS

## ЗАКОНОМЕРНОСТИ ВЛИЯНИЯ ЭЛЕКТРОННО-ЛУЧЕВОЙ ТЕХНОЛОГИИ НА ЭКСПЛУАТАЦИОННЫЕ ХАРАКТЕРИСТИКИ ОПТИЧЕСКИХ ЭЛЕМЕНТОВ С НАНОРАЗМЕРНЫМИ ОКСИДНЫМИ ПОКРЫТИЯМИ

DScTech, Yatcenko I. V.
Department of Electrical Systems – Cherkassy State Technological University, Ukraine
E-mail: irina.yatsenko.79@ukr.net

***Summary:*** *It is determined, that electron-beam processing of elements from optical glasses with nanosized coatings from metal oxides leads to improvement of their physical and mechanical properties, that influence operational characteristics of elements: negative microdefects on the surface are excluded, its microporosity decreases by 5... 10%, as well as microroughness from 30... 35 nm to 9... 15 nm; the microhardness of the surface increases from 2,3…3,5 GPa to 23,7…24,9 GPa, thus the influence of the coating thickness on its value decreases by 30...40%; wear resistance increases by 7... 12% and service life of optical elements increases by 20... 30%. Mathematical model has been developed, allowing to pre-define critical modes of electron-beam processing of elements, control of which allows to prevent their possible destructions and increase the probability of nonfailure work at operation.*
**KEY WORDS:** OPTO-ELECTRONIC INSTRUMENT MAKING, OPTICAL ELEMENTS, ELECTRON BEAM

## *1. Introduction*

In order to increase durability, reduction of radiation and convective components of thermal losses, nanosized oxide coatings representing compositions of oxides $Bi_2O_3$, $TiO_2$, ZnO, $SiO_2$, $Al_2O_3$ are applied onto the optical elements of precision instrumentation [1 – 6].

One of the widely used methods of obtaining such coatings is the method of thermal vacuum deposition of materials, which allows to obtain nanosized (< 100 nm) coatings in the form of separate layers. In this case, the obtained coatings are heterogeneous, contain hidden microdefects (cracks, chips, etc.), the surface contains significant microunevenesses and low microhardness, etc. All this leads to a decrease in the functional characteristics of these coatings: their wear resistance decreases; reflection coefficient decreases in the low infrared area and in the area of visible radiation; dispersion coefficient increases, etc.

The wide use of traditional methods of preparation and processing of surfaces of optical elements with oxide coatings (mechanical, chemical, chemical-mechanical) [2 – 4] has shown the impossibility of obtaining simultaneously clean and flawless surface, as well as flawless layers, that leads to deterioration of technical and operational characteristics of optic-electronic devices.

Fundamental researches conducted in the field of development of new high-intensity technologies for processing various materials [7 – 10], including optical materials, showed that the most promising sources of energy for such technologies are the focused streams of charged particles (electrons, ions), laser radiation, etc. However, the use of, for example, ion and laser surface processing of elements has revealed a number of obstacles that limit the possibility of their wide use in precision instrumentation: the disturbance of the surface microgeometry; formation of local high-temperature zones with large temperature gradients, leading to the emergence of critical termotensions in materials and their destruction, etc. As practice has shown [3, 7 – 17], the most convenient, environmentally friendly and the steerable way of elements processing is the electron-beam method, allowing to receive surfaces of high purity with minimal roughness, and also with the increased microhardness and thickness of hardened layers in tens of microns.

However, the wide use of electron-beam technology in precision instrumentation is hampered by the lack of data as to the regularity of the effects of electron-beam treatment regimes, the control of which allows to improve the performance characteristics of optical elements with oxide coatings (roughness and microhardness of the surface, the degree of its purity and porosity of surface layers, wear resistance, lifetime etc.).

**Therefore, the purpose of this work** is experimental and theoretical study of the influence regularities of electron-beam processing modes of optical elements with nanosized oxide coatings on their operational characteristics.

## *2. Results and discussion*

As a result of carried out researches on samples from optical glass K8 (the plates $6 \cdot 10^{-2}$ m were used, they were $3 \cdot 10^{-2}$ m wide and $4 \cdot 10^{-3}$ m thick) it was found that after electron-beam processing of oxide coatings there were no negative microdefects, and the microroughness decreases from 30... 35 nm to 9... 15 nm (Fig. 1, 2).

The studies of surface microhardness of optical elements with oxide coatings showed its increase after electron-beam treatment: from 17,5...21,5 GPa to 23,7...24,9 GPa for coating $Al_2O_3$; from 9,3...13,1 GPa to 14,7...15,9 GPa for coating $ZrO_2$; from 2,3...3,5 GPa to 6,3...7,1 GPa for coating $TiO_2$ (Fig. 3). Thus, for coatings processed by an electron beam, influence of their thickness on the size of surface microhardness weakens by 30... 40%.

It is also determined that after electron-beam processing of oxide coatings on optical elements, their lifetime is increased by 20... 30%. Thus, the porosity of the surface decreases by 5... 10% and wear resistance rises by 7... 12%.

As a result of conducted experimental researches it was also determined, that at critical values of technological parameters of electron-beam installation (electron beam current $I_л$ (mA), accelerating voltage $V_y$ (kV) and distance to processed coating surface $l$ (m)) destructions occur both along the thickness of the optical plate and on the border of oxide coating – the main material of the plate (optical glass K8, BK10, etc.).

Therefore, the preliminary definition and control of the ranges of the critical values of these parameters allows to prevent possible destructions of optical elements and to increase the likelihood of non-failure performance.

Determination of critical modes of electron-beam processing (beam current $I_л^*$, accelerating voltage $V_y^*$ and distance to the processed surface $l^*$) is carried out for double-layered plate based on the maximum density of thermal exposure of the beam ($F_n$, $Wt/m^2$), that allows to find the maximum change ranges of processing modes, within which the plate is not destroyed. The specified $F_n$ values are based on the mathematical processing of experimental data on the sensing of the band electron beam (relative error did not exceed 5... 8%) [3, 15]:

$$F_n(x)=\sqrt{\frac{k_0(I_л,l)}{\pi}}\cdot\frac{I_л\cdot V_y}{B\cdot erf\left[b(I_л,l)\cdot\sqrt{k_0(I_л,l)}\right]}, \quad (1)$$

$$k_0(I_л,l) = 1{,}237\cdot10^7\text{-}6{,}587\cdot10^5 l\text{-}3{,}725\cdot10^4 I_л + 1{,}518\cdot10^2 I_л l, \quad (2)$$

$$b(I_л,l)\frac{1{,}75}{\sqrt{k_0(I_л,l)}}, \quad (3)$$

where $k_0$ is concentration coefficient (acuteness of thermal impulse), $m^{-2}$; $2b$, $B$ is thickness and width of the band electron beam, respectively, m.

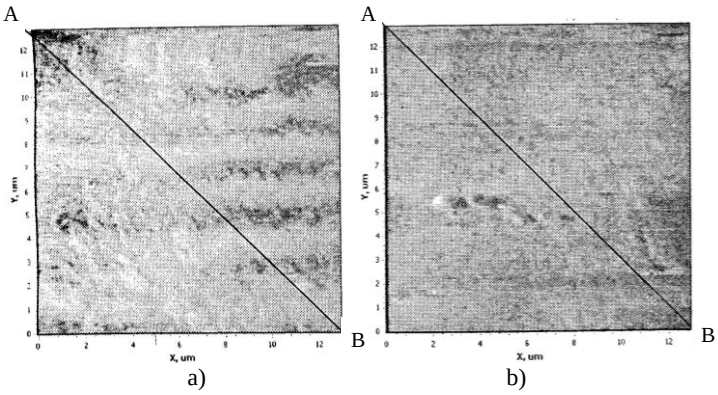


*Fig. 1. Topography of the surface area (13 × 13 microns) of the optical element with coating $TiO_2$ to (a) and after (b) electron-beam processing.*

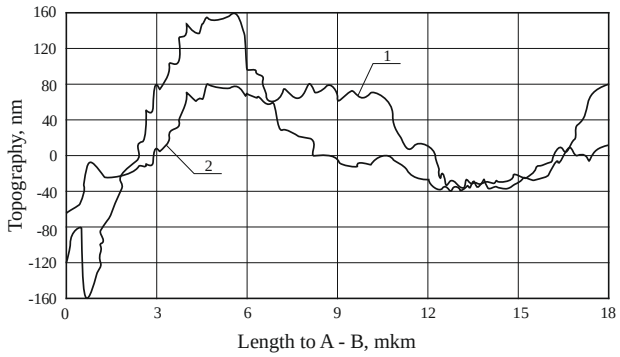


*Fig. 2. Topography along A-B line of the surface area (13 × 13 microns) of the optical element with coating $TiO_2$ to (1) and after (2) electron-beam processing.*

Thereat, it was determined that for performance change ranges of the determined parameters ($I_л$ = 50…300 mA, $l$ = 0,04...0,08 m, $B$ = $6\cdot10^{-2}$…$8\cdot10^{-2}$ m) the following change processing ranges are realized: $k_0$ = $(0{,}5…5)\cdot10^7$ $m^{-2}$; $2b$ = $(0{,}5…1{,}5)\cdot10^{-3}$ m; $F_n$ = $10^6$…$10^9$ Wt/$m^2$.

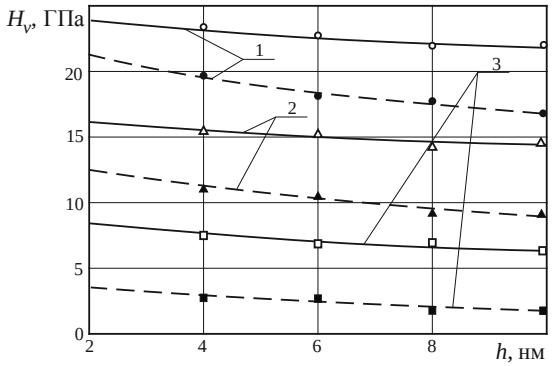


*Fig. 3. Dependences of surface microhardness of optical elements with oxide coatings $Al_2O_3$ (1), $ZrO_2$ (2) and $TiO_2$ (3) from their thickness: ——— – after electron beam treatment; – – – – to electron-beam treatment;* Δ, ○, □, ▲, ■, ● *– experimental data.*

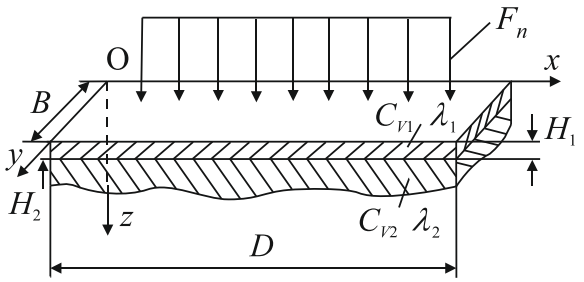


*Fig. 4. Heating scheme of an optical plate with an oxide coating with an electronic beam with thermal impact density $F_n$: B, D – plate thickness and length, m; $C_{V1}$, $\lambda_1$, $H_1$, $C_{V2}$, $\lambda_2$, $H_2$ – volumetric heat capacity (J/$m^3$·K), thermal conductivity coefficient (Wt/m·K) and length (m) in correspondence with oxide coatings (1) and optical material of the plate (2).*

Mathematical model of the heating process of the double-layered plate. The considered plate, which is processed by the scanning electron beam, that realizes the uniform heat effect $F_n$ (fig. 4) on the whole surface. Thus, the plate consists of two layers of heterogeneous materials (one is an optical material, and the other is oxide or other material (aluminum, titanium, etc.)). Between the layers there is an ideal thermal contact, radiation and convective heat losses, in the first approximation, not taken into account, but fulfilled are the conditions: $\delta_1 = 2\cdot\left(a_{01}^2\cdot\tau\right)^{1/2} \sim H_1$ and $\delta_2 = 2\cdot\left(a_{02}^2\cdot\tau\right)^{1/2} << H_2$ [2] ($\delta_1$, $\delta_2$ – penetration depth of the thermal wave inside the coating and plates, m; $\tau$ – time of thermal influence of the electron beam, s; $a_{01}^2$, $a_{02}^2$ – coefficients of diffusivity of coating and plate, $m^2$/s), that is, the plate is considered as half boarder environment, on the underside of which the conditions of heat exchange aren't taken into account.

Equations of the mathematical heating model of the double plate have the form of [18]:

$$C_{V1}(T_1)\cdot\frac{\partial T_1}{\partial t}=\frac{\partial}{\partial z}\left[\lambda_1(T_1)\cdot\frac{\partial T_1}{\partial z}\right],\ t>0,\ 0<z<H_1, \quad (4)$$

$$C_{V2}(T_2)\cdot\frac{\partial T_2}{\partial t}=\frac{\partial}{\partial z}\left[\lambda_2(T_2)\cdot\frac{\partial T_2}{\partial z}\right],\ t>0,\ H_1<z<+\infty, \quad (5)$$

$$T_1\big|_{t=0}=T_2\big|_{t=0}=T_0, \quad (6)$$

$$-\lambda_1(T_1)\cdot\frac{\partial T_1}{\partial z}\bigg|_{z=0}=F_n, \quad (7)$$

$$T_1\big|_{z=H_1}=T_2\big|_{z=H_1}, \quad (8)$$

$$\lambda_1(T_1)\cdot\frac{\partial T_1}{\partial z}\bigg|_{z=H_1}=\lambda_2(T_2)\cdot\frac{\partial T_2}{\partial z}\bigg|_{z=H_1}, \quad (9)$$

$$T_2\to T_0,\quad \left(\frac{\partial T_2}{\partial z}\right)\to 0 \text{ at } z\to+\infty. \quad (10)$$

Taking dependencies into account [2, 3]

$$C_{Vi}=C_{Vi0}\cdot T_i^{\nu},\quad \lambda_i=\lambda_{i0}\cdot T_i^{\nu}\ \ (i=1,2) \quad (11)$$

and replacing of variables

$$\theta_i(z,t)=T_i^{\nu+1}-T_0^{\nu+1}, \quad (12)$$

we get linear system of equations:

$$\frac{\partial\theta_1}{\partial t}=a_{01}^2\cdot\frac{\partial^2\theta_1}{\partial z^2}, \quad (13)$$

$$\frac{\partial\theta_2}{\partial t} = a_{02}^2 \cdot \frac{\partial^2\theta_2}{\partial z^2}\,, \qquad (14)$$

$$\theta_1\big|_{t=0} = \theta_2\big|_{t=0}\,, \qquad (15)$$

$$-\frac{\partial\theta_1}{\partial z}\bigg|_{z=0} = \bar{q}_{n0}\,, \qquad (16)$$

$$\theta_1\big|_{z=H_1} = \theta_2\big|_{z=H_1}\,, \qquad (17)$$

$$\lambda_{01}\cdot\frac{\partial\theta_1}{\partial z}\bigg|_{z=H_1} = \lambda_{02}\cdot\frac{\partial\theta_2}{\partial z}\bigg|_{z=H_1}\,, \qquad (18)$$

$$\theta_2 \to 0\,,\ \frac{\partial\theta_2}{\partial z} \to 0 \ \text{ at } \ z \to +\infty\,, \qquad (19)$$

where $$a_{0i}^2 = \frac{\lambda_{0i}}{C_{V0i}}\,, \qquad \bar{q}_{n0} = \frac{\nu+1}{\lambda_{01}}\cdot F_n\,. \qquad (20)$$

To solve the obtained linearized problem (13) – (19) we use the direct and inverse Laplace transform by $t$ variable [18] and, considering (12), we get the solution of the initial problem:

$$T_1(z,t) = \left\{ T_0^{\nu+1} + \frac{4(\nu+1)\cdot F_n\cdot a_{10}\cdot\sqrt{t}}{\lambda_{10}}\cdot \right.$$

$$\left.\cdot\left[\sum_{n=0}^{\infty} b^n\cdot i\cdot erfc\left(\frac{2H_1 n + z}{2a_{10}\cdot\sqrt{t}}\right) - \sum_{n=0}^{\infty} b^n\cdot i\cdot erfc\left(\frac{2H_1 n - z}{2a_{10}\cdot\sqrt{t}}\right)\right]\right\}^{\frac{1}{\nu+1}}, \qquad (21)$$

$$T_2(z,t) = \left\{ T_0^{\nu+1} + \frac{4(\nu+1)\cdot F_n\cdot a_{10}\cdot\sqrt{t}}{\lambda_{10}\cdot(1+d_0)}\cdot \right.$$

$$\left.\cdot\sum_{n=0}^{\infty} b^n\cdot i\cdot erfc\left(\frac{H_1 n}{a_{10}\cdot\sqrt{t}} + \frac{z}{2a_{20}\cdot\sqrt{t}}\right)\right\}^{\frac{1}{\nu+1}}, \qquad (22)$$

where $$i\cdot erfcu = \int_u^{\infty} erfc\,\xi d\xi = \frac{1}{\sqrt{\pi}}\cdot e^{-u^2} - u\cdot erfcu \qquad (23)$$

and $$erfcu = 1 - erfu\,, \qquad (24)$$

$$erfu = \frac{2}{\sqrt{\pi}}\int_0^u \cdot e^{-\xi^2} d\xi \quad - \qquad (25)$$

special functions [2].

Determination of thermoelastic stresses in the double-layered plate at the electron beam impact. To find the thermoelastic stresses in the considered plate $\sigma_i(z,t)$ ($i$ = 1, 2 – the numbers of coating and plate, respectively) we use the standard ratios for calculating stresses in flat layers [2, 18]:

$$\sigma_i(z,t) = \frac{\alpha_{Ti}\cdot E_i}{1-\nu_i}\cdot\left[-T_i(z,t) + \frac{2}{H_1^2}\cdot(2H_1 - 3z)\cdot\right.$$

$$\left.\cdot\int_0^{H_1} T_i(z,t)dz - \frac{6}{H_1^3}\cdot(H_1 - 2z)\cdot\int_0^{H_1} T_i(z,t)\cdot z dz\right], \qquad (26)$$

where $\alpha_{Ti}$, $E_i$, $\nu_i$ ($i$ = 1, 2) – thermal coefficient of linear expansion ($K^{-1}$), Jung Module (Pa) and Poisson coefficient respectively.

The results of calculations of thermoelastic stresses $\sigma_1(z,t)$ at the thickness of oxide coating with the use of known physical and mechanical properties of glass K8 and oxide $Al_2O_3$ [2, 3], as well as standard software are presented on Fig. 5.

From the results of calculations, it follows that the maximum values of thermoelastic stresses can be reached near the surface of the plate, that is, in the oxide coating. It is determined, that they essentially depend on technological parameters of electron-beam installation: increase of current from 200 mA up to 300 mA and accelerating voltage from 6 kV to 8 kV, and also reduction of distance from the processed surface from $8\cdot10^{-2}$ m до $4\cdot10^{-2}$ m lead to growth of thermoelastic stresses in 1,5…2,1 times; at the same time their maximum varies from $0{,}7\cdot10^8$ N/m$^2$ to $1{,}5\cdot10^8$ N/m$^2$ and is achieved in the middle of the coating.

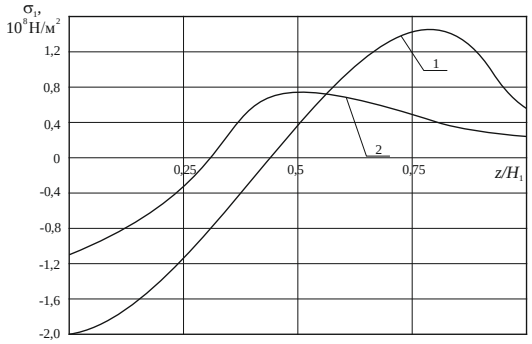


***Fig. 5.*** *Distribution of thermoelastic stresses on the thickness of plates of optical glass K8 with oxide coating $Al_2O_3$ at their electron beam processing for different times of the beam influence ($T_0$ = 300 K, $H_1$ = 10 μm): 1 – $I_л$ = 300 mA, $V_y$ = 8 kV, $l = 4\cdot10^{-2}$ m, t = 0,2 s; 2 – $I_л$ = 200 mA, $V_y$ = 6 kV, $l = 8\cdot10^{-2}$ m, t = 0,2 s.*

In addition, while comparing the obtained values $|\sigma_1|$ with the critical values $\sigma_1^*$ [3], it is possible to determine the critical values of the controlled parameters $I_л^*$, $V_y^*$ and $l^*$, the excess of which leads to the destruction of the oxide coatings processed by the electron beam.

In conclusion, it should be noted that the conducted theoretic-experimental researches have allowed to establish the following optimal modes of electron-beam technology, within the boundaries of which there is an improvement of physical and mechanical properties and performance characteristics of optical elements with nanosized coatings from metal oxides: $F_n$ = $7\cdot10^6$…$8\cdot10^8$ Wt/m$^2$.

Thus, in light of modern advanced technologies used in optoelectronic instrumentation, electron-beam processing of optical elements with nanosized coatings of metal oxides is potentially applicable for high quality processing of flat and curved elements, obtaining functional microprofiles on their surfaces by means of electronic beams, that can be used as an element base in microoptics, integral and fiber optics, optoelectronics, functional electronics and other areas of precision instrumentation. In addition, the undeniable preferences of electron-beam technology is its ecological purity and the ability to obtain on a common board of optical material in a single technological cycle microelements with improved operational characteristics, the use of which in optical parts of optic-electronic devices contributes to their nonfailure work during operation.

## *3. Conclusions*

1. It is determined, that for optimized modes of electron-beam processing of (density of thermal influence of electron beam $F_n$ = $7\cdot10^6$…$8\cdot10^8$Wt/м$^2$) optical elements with wear-resistant and heat-insulating nanosized (< 100 nm) coatings made of metal oxides ($SnO_2$, $Bi_2O_3$, $TiO_2$, ZnO, $SiO_2$, $Al_2O_3$, etc.) there is an improvement of their physical and mechanical properties and operational characteristics:

– no negative microdefects are observed on the surface, its porosity decreases by 5... 10%, thereat microroughness decreases from 30... 35 nm to 9... 15 nm;

– the surface microhardness increases from 2,3…3,5 GPa to 23,7…24,9 GPa, and the effect of the coating thickness on the size of the surface microhardness is reduced by 30...40%;

– durability of optical elements increases by 7...12%, and also service life increases by 20... 30%.

2. For the first time mathematical model has been developed for determining the critical modes of electron-beam processing of optical elements with nanosized oxide coatings (beam current $I_л^*$, accelerating voltage $V_y^*$ and distance to the processed surface $l^*$), that allows to prevent possible destruction of elements and to increase the probability of their nonfailure work during operation by controlling ranges of their changes.

## *4. References*


1. Burak A. V., Gordienko V. I., Denisenko A. Y. Modernizatsiya nochnyh tankovyh pritselov (Modernization of night tank sights) Mechanika ta mashinobuduvannya, 2002, 2, P. 210 – 213.
2. Vashchenko V. A., Kotelnikov D. I., Lega Y. G., Krasnov D. M., Yatsenko I. V., Kirichenko O. V. Teplovye protsesy pri elektronnoi obrabotke opticheskih materialov i ekspluatatsii izdelii na ich osnove (Thermal processes in the electronic processing of optical materials and use of products based on them) Kiev: Naukova Dumka, 2006, 368 p.
3. Vashchenko V. A., Yatsenko I. V., Lega Y. G., Kirichenko O. V. Osnovy elektronnoi obrobky vyrobiv z optychnyh materialiv (The basics of electronic processing of optical materials) Kiev: Naukova Dumka, 2011, 562 p.
4. Braginets I. A., Kononenko A. G., Masurenko Y. G., Nizhenskii A. D. Povyshenie tochnosti impulsnyh lazernyh svetodalnomerov (Improved accuracy of pulsed laser rangefinders) Technicheskaya elektrodinamika, 2003, 6, P. 64 – 70.
5. Vilchinskya S. S., Lisitsyn V. M. Opticheskie materialy i tehnologii (Optical materials and technologies) Tomsk: Ed. Tomsk Polytechnic University, 2011, 107 p.
6. Kolobrodov V. G., Gordienko V. I. Otsenka effektivnosti tankovogo pritselnogo kompleksa (Estimation of the effectiveness of the tank sighting complex) Artileriiskoe i strelkovoe vooruzhenie, 2010, 1, P. 32.
7. Bessmertnyi V. S. Plazmennaya obrabotka stekol (Plasma processing of glasses) Steklo i keramika, 2001, 4, P. 6 – 8.
8. Vasin V. A. Sovremennoe vozdeistvie SVC-polya i sfokusirovannogo lazernogo izlucheniya na dielektriki (Modern effects of microwave fields and focused laser radiation on dielectrics) Steklo i keramika, 2000, 10, P. 23 – 26.
9. Golovko L. F., Roman V. V., Valid Nysiraf Pidvyshcennya efektyvnosti lazernoi obrobky keruvannyam rozpodilu potuzhnosti vyprominuvannya na poverhni fokusuvannya (Increase the efficiency of laser processing by controlling the distribution of radiation power on the focusing surface) Ekspress-novyny. Nauka, tehnika, vyrobnytstvo, 1999, 5 – 6, P. 15 – 17.
10. Golovko L. F., Lukyanenko S. O. Lazerni tehnologii ta komputerne modeluvannya (Laser technology and computer simulation) Kyiv: Vistka, 2009, 296 p.
11. Bochok M. P., Budko N. P., Vashchenko V. A., Kanashevich G. V., Kotelnikov D. I. Spetsialni metody obrobky optychnogo skla. Navchalnyi posibnyk (Special methods of optical glass processing. Tutorial) Chernigiv: Chernihiv State Technological University, 2001, 215 p.
12. Yatsenko I. V., Antoniuk V. S., Vashchenko V. A., Tsybulin V. V. Uprezhdenie vozmozhnych razrushenii opticheskich obtekatelei IK-priborov v usloviyach vystrela i poleta (Preventing possible destruction of the optical fairings of infrared devices in the conditions of a shot and flight) Ezhemesyachnyi nauchno-technicheskii i proizvodstvennyi zhurnal "Nanoinzheneriya", 2015, 12(54), P. 26 – 31.
13. Yatsenko I. V., Antoniuk V. S., Vashchenko V. A., Tsybulin V. V. Poperedzhennya mozhlyvyh ruinuvan optychnyh elementiv tochnogo pryladobuduvannya v umovah zovnishnih termodii (Prevention of possible destruction of optical elements of precision instrumentation in conditions of external thermo-influences) Zhurnal nano ta elektronnoi phizyki, 2016, Vol. 8, 1, P. 01027 – 01032.
14. Yatsenko I. V., Antoniuk V. S., Vashchenko V. A., Tsybulin V. V. Vyznachennya krytychnyh znachen parametriv elektronnogo promenu pry poverhnevomu oplavlenni optychnych elementiv tochnogo pryladobuduvannya (Determination of the critical values of the parameters of an electron beam at the surface melting of optical elements of precision instrumentation) Zhurnal nano ta elektronnoi phizyki, 2017, Vol. 9, 1, P. 01010(5).
15. Yatsenko I. V. Doslidzhennya zalezhnostei energetychnych charakterystyk SEP vid yogo kerovanych parametriv pry vplyvi na vyroby mikrooptyky i integralnoi optyky (Investigation of dependencies of power characteristics of TES on its controlled parameters under the influence on products of micro-optics and integral optics) "Trudy Odesskogo politechnicheskogo universiteta", 2009, Issue 2(32), P. 143 – 149.
16. Yatsenko I., Antoniuk V., Kiritchenko O., Vashchenko V. Improvement of technical and operational characteristics of devices with optical elements by preliminary electron beam treatment of their surface. International journal for science and innovations for the industry "Machines. Technologies. Materials", ISSN 1313-0226, YEAR X, ISSUE 6/2016, Bulgaria, P. 47 – 50.
17. Yatsenko I., Antoniuk V., Kiritchenko O., Vashchenko V., Tsybulin V. Improving the reliability instruments of measuring and thermal control of objects of different physical nature by the finish of electron beam processing surfaces of optical elements. International journal for science and innovations for the industry "Machines. Technologies. Materials" ISSN 1313-0226, YEAR XI, ISSUE 1/2017, Bulgaria, P. 20 – 23.
18. Vashchenko V. A., Antoniuk V. S., Tymchik G. S., Yatsenko I. V., Bondarenko M. O., Kirichenko O. V., Rud M. P. Osnovy teploperenesennya v elementah optychnogo pryladobuduvannya (Fundamentals of heat transfer in elements of optical instrumentation) Kyiv: NTUU "KPI", 2012, 412 p.

# INVESTIGATION OF THE EFFECT OF DIAMETERS OF POLYACRYLONITRILE NANO FIBER WITH CARBON NANOTUBE ON MECHANICAL PROPERTIES

Assist.Prof.Dr¨Gürol Ö.[1], Assoc.Prof.Dr¨Kevser D[1]

[1]Selcuk University, Department of Mechanical Engineering, Konya/TURKEY
Email:gonal@selcuk.edu.tr, kdincer@selcuk.edu.tr,

***Abstract****: In this study, pure polyacrylonitrile (PAN) nano fiber (8 wt. %) and PAN nano fiber with multi-walled carbon nanotubes (MWCNT) were prepared. The content of MWCNT was (1, 3 and 5 wt.%). Electrospin device was used in nanofiber production. Nano diameters of the produced nanofibers were examined by Scanning electron microscopy (SEM). The nanofiber samples were cut 0.5 cm wide and 2 cm long. These samples were subjected to a tensile test on the Shimadzu device. The effect of nanofiber diameters on mechanical properties was investigated. All the MWCNT based composite nanofibers presented larger diameters than those of pure PAN nanofibers. The maximum stress value (76.60 kN) was found to be at PAN nanofiber with 1% MWCNT (average nano fiber diameter is 369.45 nm).*

**KEYWORDS**: CARBON NANOTUBE, ELECTROSPINNING, MECHANICAL PROPERTIES, NANOFIBERS

## *1. Introduction*

Until now electrospinning has been considered to be relatively the simplest process for producing materials at nano-scale. However, it has been stipulated that the physic behind it is not easy to understand since the properties of the electrospun nanofibers can be significantly influenced by many parameters. Electrospun nanofibers present unique properties such as a high surface area to volume ratio, lightweight, high porosity, good thermal, mechanical, electrical and flexibility properties. Materials obtained from electrospinning technique can find a wide range of applications, notably in electronic, medicine, environment protection, energy conversion and storage, and so on [1]. Electrospin-produced nanofibers are generally preferred as additives and fillers [2, 3, 4].

The hexagonal ring structure of CNT is used as a strengthening element since it develops mechanical characteristics. CNT not only increases the mechanical properties but also the electrical and thermal conductivity values. For this reason, CNT is added to the polymer in the process of obtaining nanofibers by electrospinning. These materials are always preferred due to their physicochemical properties [5]. Ju et al. [6] reported that thinner nanofibers could be produced with the preference of the electrospin method, and that the CNT-added solution generally had high electrical conductivity when compared to the CNT-free solution. This method is a unique technique for producing nanofibers with CNT added to provide non-woven structure. However, the success of this method depends on the distribution of CNT among the nanofibers.

Nanotubes are categorized as single-walled nanotubes (SWNTs) and multi-walled nanotubes (MWNTs). Individual nanotubes naturally align themselves into "ropes" held together by van der Waals forces, more specifically, pi-stacking. Multi-walled nanotubes (MWNTs) consist of multiple rolled layers (concentric tubes) of graphene. There are two models that can be used to describe the structures of multi-walled nanotubes. In the Russian Doll model, sheets of graphite are arranged in concentric cylinders, e.g., a (0,8) single-walled nanotube (SWNT) within a larger (0,17) single-walled nanotube. In the Parchment model, a single sheet of graphite is rolled in around itself, resembling a scroll of parchment or a rolled newspaper. The interlayer distance in multi-walled nanotubes is close to the distance between graphene layers in graphite, approximately 3.4 Å. The Russian Doll structure is observed more commonly. Its individual shells can be described as SWNTs, which can be metallic or semiconducting. Because of statistical probability and restrictions on the relative diameters of the individual tubes, one of the shells, and thus the whole MWNT, is usually a zero-gap metal [7].

In this study, PAN nano fiber and PAN nano fiber with MWCNT were prepared. The content of multi-walled nanotube is (1, 3 and 5 wt.%). Investigation of the effect of diameters of polyacrylonitrile nano fiber with carbon nanotube on mechanical properties (at Selcuk Universtiy condition).

## *2. Material and Method*

### *2.1. Fabrication of pure PAN nanofibers and PAN nanofibers with MWCNT*

Electrospinning is a unique approach using electrostatic forces to produce fine fibers. Polymer solution or the melt that has to be spun is forced through a syringe pump to form a pendant drop of the polymer at the tip of the capillary. High voltage potential is applied to the polymer solution inside the syringe through an immersed electrode, thereby inducing free charges into the polymer solution. These charged ions move in response to the applied electric field towards the electrode of opposite polarity, thereby transferring tensile forces to the polymer liquid. At the tip of the capillary, the pendant hemispherical polymer drop takes a cone like projection in the presence of an electric field. And, when the applied potential reaches a critical value required to overcome the surface tension of the liquid, a jet of liquid is ejected from the cone tip [8].

The equipment and chemicals used in this study for the preparation of the solutions, production and characterization of nanofibers are listed in the Table 1.

***Table 1.*** *List of materials*

| Equipments or chemicals | Description |
|---|---|
| Polyacronitrile (PAN), 150,000g/mol of (Mw) | From the Sigma Aldrich Co. |
| N, N- Dimethylformamide anhydrous, 99.8% | From the Sigma Aldrich Co. |
| MWCNT, 20 nm %99.9 | From Nanografi |
| Stainless steel needles | With 0.8ml as inner diameter |
| Digital balance | |
| Syringe pump | |
| Magnetic fish | |
| Collector | |
| Magnetic stirrer | |
| High voltage power supply | |
| Masks | |
| Gloves | |
| Scissors | |
| SEM | |
| Tensile test | |
| TEM | |

All the electrospinning solutions were prepared in the same way, the used procedure can be presented as follows (Fig.1):

- Weigh the required amount of chemicals (PAN and DMF) using the digital balance,
- Homogenization of PAN/DMF mixture using magnetic stirrer for 3 hours,
- Once the second step is successfully achieved, weigh the mass of the obtained homogeneous solution using again the digital balance,
- According to the quantity of mass obtained in the third step, calculate the required amount of MWCNT in relation to their respective percentage which must be introduced in the previous PAN/DMF solution,
- Pour the required amount of MWCNT in the PAN/DMF solution,
- Homogenization of the new PAN/DMF/ MWCNT mixture using magnetic stirrer for an hour,
- Once the sixth step is successfully achieved then, withdraw the solution from the magnetic stirrer until it reaches the room temperature,
- The last step is pouring the solution in the syringe.

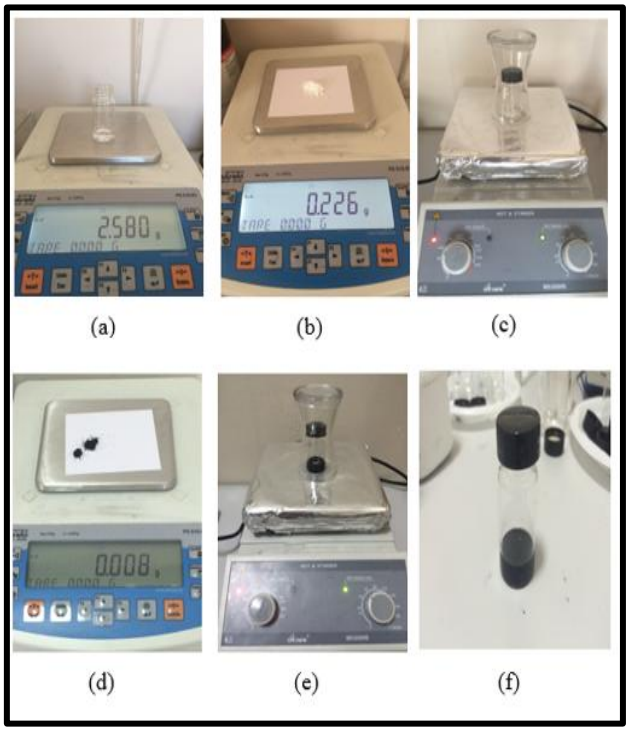


***Fig. 1.*** *Preparation and electrospinning process of 8 wt. % PAN polymer content solution (a) DMF, (b) PAN, (c) solution of PAN and DMF on the magnetic stirrer, (d) MWCNT, (e) solution of PAN and DMF with MWCNT on the magnetic stirrer, (f) solution of PAN and DMF with MWCNT was waiting at the room temperature*

After the homogenization process, in each case the solution was brought to the room temperature. Then, the prepared electrospinning solutions were poured into a 2.5 mL syringe pump with 0.8 mm as inner diameter in order to proceed with the electrospinning setup. The applied voltage was 15 kV. The needle to the collector distance was 12 cm. The solution flow rate maintained at 2 mL/h.Rotating speed was 112.5 rpm. The electrospinning process was carried out (Fig. 2).




***Fig.2*** *Electrospinning experimental setup*

### *2.2. Tensile Tests of PAN Nanofiber and PAN Nanofiber with MWCNT*

The morphology of the fabricated PAN nanofibers and PAN nanofibers with MWCNT was characterized by SEM (Zeiss Evo LS10). In Fig. 3 show the SEM images of the fabricated PAN nanofiber/PAN composite nanofibers with different MWCNT concentration (1, 3 and 5wt.%) performed at 15 kV. The fibers diameter increased from 210.45 nm for pure PAN fibers to 369.45 nm, 330.3 nm and 241.75 nm for MWCNT composite nanofibers containing 1, 3, and 5 wt. % MWCNT, respectively. It is important to note that the average diameter of MWCNT based nanofibers decreased with the increase of MWCNT contents in the electrospinning solution.

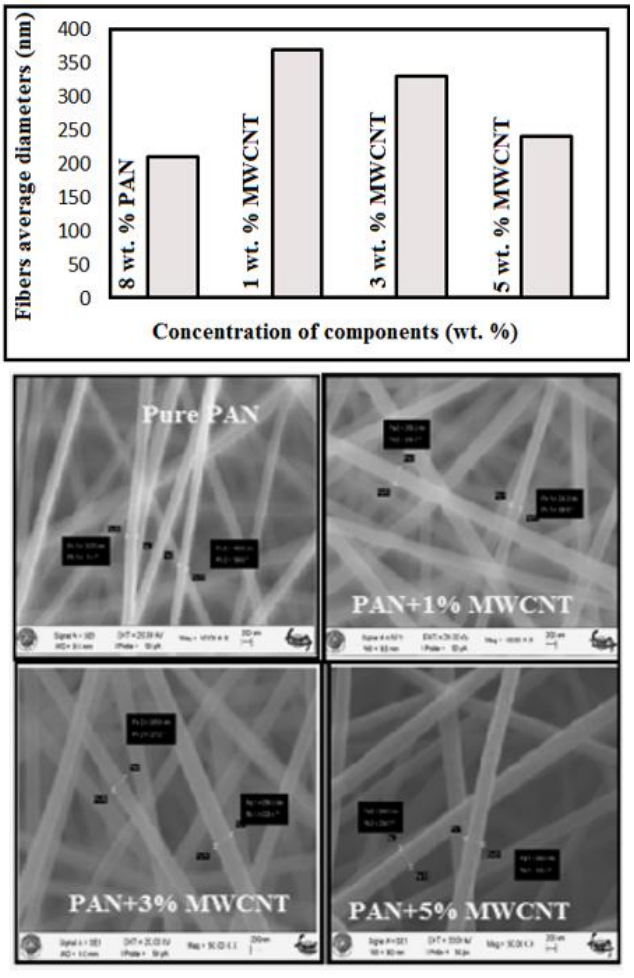


***Fig.3.*** *Comparison of average diameter of the fabricated pure PAN nanofibers and PAN/MWCNT composite nanofibers for concentration of components (wt. %)*

The samples were cut 0.5 cm wide and 2 cm long. These samples were subjected to a tensile test on the Shimadzu device. Tensile tests were performed by Shimadzu AGS-X hydraulic desktop test device at room temperature. Situations before of tensile test of samples at Figs. 4a-7a and situations during of tensile test of samples at Figs. 4b- 7b and situations after of tensile test of samples at Figs. 4c- 7c were presented.

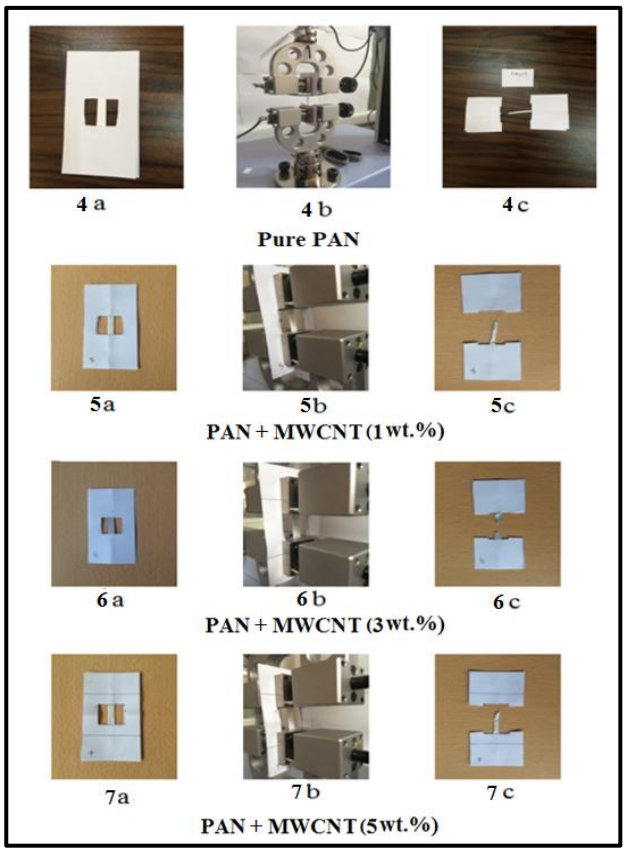


***Fig. 4-7****. The situations of samples in the tensile test*

Fig. 8 reports the variation of stress in terms of the change of the strain of PAN nanofiber and PAN/MWCNT composite nanofibers. Generally speaking, we have found that the stress increased with the nano fibers diameters.

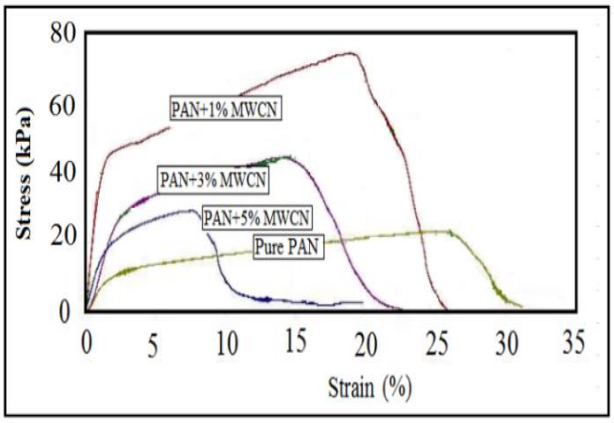


***Fig. 8.*** *Variation of stress in the function of strain (%)*

In Fig. 9., the results on maximum stress are compared for nanofibers diameters. All the MWCNT based composite nanofibers presented larger diameters than those of pure PAN nanofibers.

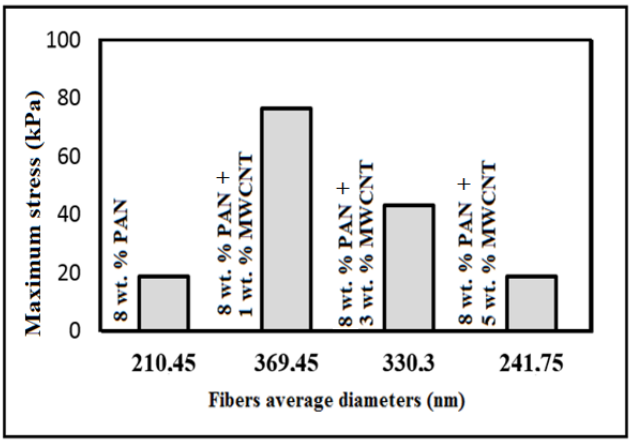


***Fig. 9.*** *Variation of maximum stress in the function of fibers average diameters*

## *2.3. Determination of Thermal Conductivity for PAN Nanofiber and PAN Nanofiber with MWCNT*

The P.A. Hilton H-940 test station was used to determine for the thermal conductivity of the materials (Fig.10). Initially, the system was expected to enter the steady state condition (approximately 20 minutes). After the system entered steady state condition, 2.2 W power was given to the system. Then the temperature values obtained from six different points (1, 2, 3, 7, 8 and 9) were recorded. The samples were placed to the middle of the experimental set shown in Fig. 10b (section h-c) and measurements were made.

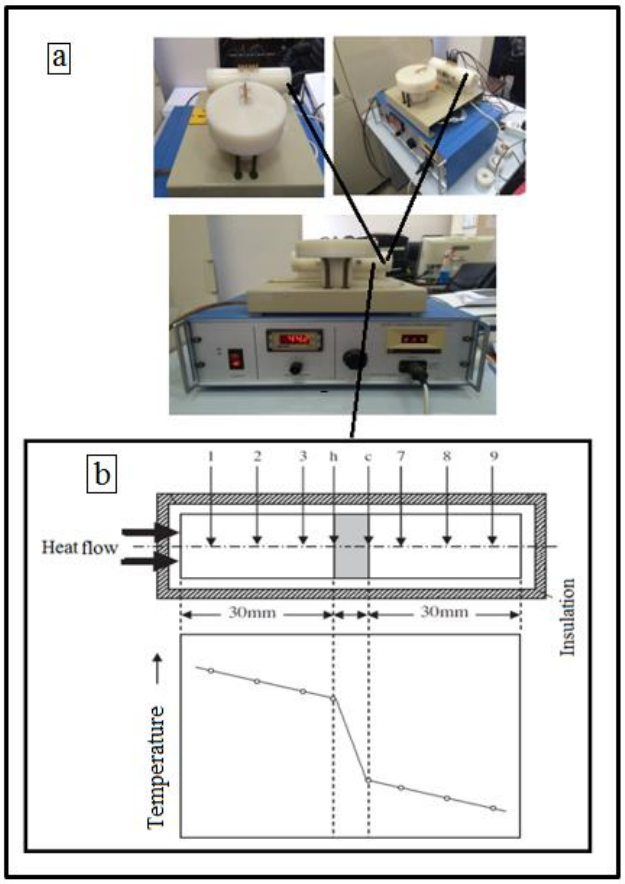


Fig.10. a) The experimental setup for thermal conductivity
b) Schematic diagram for measurement of thermal conductivity [9]

When MWCNT is added to the PAN, the thermal conductivity is increased (Fig.11). According to the PAN sample, it was found that the thermal conductivity increased 135.95 % for 1% MWCNT addition, 137.4729 % for 3% MWCNT addition and 168.70 % for 5% MWCNT addition.

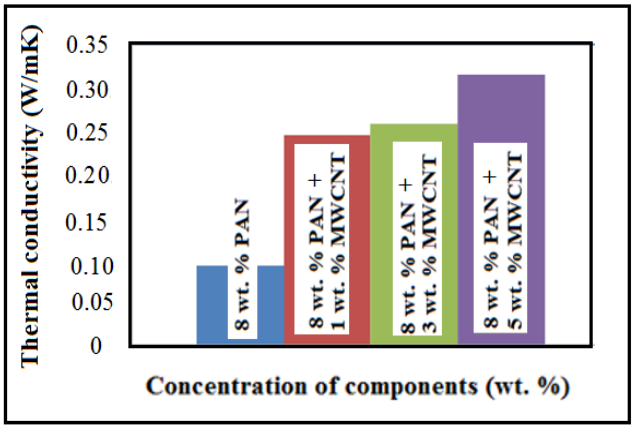


***Fig. 11.*** *Variation of thermal conductivity in the function of concentration of components*

Transmission electron microscopy (TEM) works with the principle of imaging high-energy electrons passing through a sample that is quite thin. As a result of the interaction of electrons with the sample, the resulting image is magnified. In this study, Jeol JEM-2100 (UHR) device was used for TEM images (Fig. 12). Fig. 13 shows TEM image of PAN/ MWCNT.



***Fig. 12.*** *Jeol JEM-2100 (UHR) TEM device [10]*

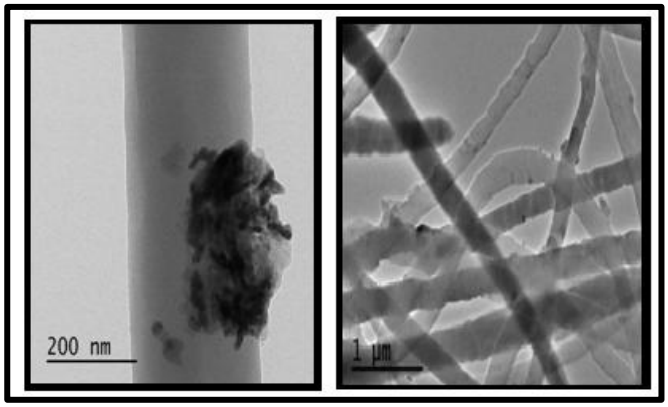


***Fig. 13.*** *TEM image of PAN/MWCNT*

## 3. Conclusions

In this study, the effect of diameters of PAN/(PAN+MWCNT) nano fiber on mechanical properties has been investigated as a function of the incorporated content. Different MWCNT contents (1, 3 and 5 wt. %) were added separately in the electrospinning solutions consisted of PAN and dimethylformamide. Nano diameters of the produced nanofibers were examined by SEM. The average diameter of MWCNT based nanofibers decreased with the increase of MWCNT contents in the electrospinning solution. However, the average nano diameter of PAN nanofiber with MWCNT is higher than the average nano diameter of pure PAN. When all the results were compared to each other, the highest stress value was obtained with 1 wt. % of MWCNT-based PAN fiber and the stress value was 76.60 kN (average fiber diameter = 369.45 nm). In other words, compared to pure PAN nanofiber, an increase of 405.29 % was observed in the stress value of fiber containing 1 wt. % of MWCNT. Taken together, the findings suggested that fibers with low content of MWCN led to higher stress. The study showed that the incorporation of MWCNT in the electrospinning solution led to an increase of thermal conductivity values of the electrospun nanofibers.

## 4. References

[1] Mpukuta, O.M., Investigation of electrical conductivity of nanofibers (PAN) containing nanoparticles (Graphene, Copper, Silica) produced by electrospinning method, Master of Science Thesis, Selcuk University, Department of Mechanical Engineering.

[2] Dersch, R., Steinhart, M., Boudriot, U., Greiner, A. Wendorff, J., 2005, Nanoprocessing of polymers: applications in medicine, sensors, catalysis, photonics, Polymers for Advanced Technologies, 16 (2-3), 276-282.

[3] Kim, G., Lach, R., Michler, G., Pötschke, P. Albrecht, K., 2006, Relationships between phase morphology and deformation mechanisms in polymer nanocomposite nanofibres prepared by an electrospinning process, Nanotechnology, 17 (4), 963.

[4] Heikkilä, P. Harlin, A., 2009, Electrospinning of polyacrylonitrile (PAN) solution: Effect of conductive additive and filler on the process, Express Polymer Letters, 3 (7), 437-445.

[5] Chinnappan, A., Lee, J. K. Y., Jayathilaka, W. Ramakrishna, S., 2018, Fabrication of MWCNT/Cu nanofibers via electrospinning method and analysis of their electrical conductivity by four-probe method, International Journal of Hydrogen Energy, 43 (2), 721-729.

[6] Ju, Y.W., Choi, G.R., Jung, H.R. Lee, W.J., 2008, Electrochemical properties of electrospun PAN/MWCNT carbon nanofibers electrodes coated with polypyrrole, Electrochimica Acta, 53 (19), 5796-5803.

[7] https://en.wikipedia.org/wiki/Carbon_nanotube

[8] Önal, G., Erdal MO, Dincer K. 2017, Investigation of electrical conductivity of polyacrylonitrile (PAN) nanofibers/nano particule (Ag, Cu, CNT and GNR), Nano Hybrids and Composites, Vol. 16.

[9] Zain-ul-Abdein, M., Azeem, S. ve Shah, S. M., 2012, Computational investigation of factors affecting thermal conductivity in a particulate filled composite using finite element method, International Journal of Engineering Science, 56, 86-98.

[10] Anonim, 2018, iltek, https://www.selcuk.edu.tr/ileri_arge/tr: [02.06.2018].

# TUNGSTEN AND MOLYBDENUM CARBIDES OBTAINING BY ELECTROLYSIS OF SALT MELTS

Prof., D.Sc. Malyshev V.[1], Prof., D.Sc. Kushchevska N. [1], Prof., D.Sc. Bagliuk G. [2], Ph.Dr. Shakhnin D.[1], Ph.Dr. Paprotskaya O.[1], M.Sc. Kurovskyi V. [2]
Institute for Engineering & Technology – University "Ukraine", Ukraine [1]
I.M. Frantsevich's Institute for Problems in Materials Science of the National Academy of Sciences of Ukraine, Ukraine [2]

viktor.malyshev.igic@gmail.com

***Abstract:*** *Compositions of the products of the electrolysis of melts based on a eutectic mixture of sodium chloride–lithium fluoride and sodium tungstate, which contains molybdenum (VI) and tungsten (VI) oxides, molybdates, tungstates, and carbonates of lithium or sodium, are investigated. It is shown that, depending on the content of melt components, the products of electrolysis are carbon, molybdenum, tungsten, and their bronzes and carbides. The conditions of the deposition of galvanic coatings of molybdenum and tungsten carbides on carbon, nickel, and copper matrices are determined.*

**Keywords**: IONIC MELTS, MOLYBDENUM, TUNGSTEN, ELECTROMETALLURGY, SYNTHESIS, CARBIDES, POWDERS, COATINGS

## *1. Introduction*

Increased interest in the development of new effective methods for obtaining refractory compounds such as carbides, borides, silicides, alloys, and intermetallic compounds of Groups IV–VIB of the periodic table is dictated by their use in modern technique. A comparative analysis of the synthesis of metal-like refractory compounds showed that high-temperature electrochemical synthesis (HTES) is one of the most promising but still poorly known methods [1–3]. It is based on processes of the electrical separation of metals and nonmetals from ion melts. The absence of information on the theoretical foundations and principles of control over these processes made it impossible to perform HTES in practice.

The goal of this study was to investigate the composition of cathode products of carbon-containing melts based on the eutectic mixture of sodium chloride and lithium fluoride and melts based on sodium tungstate depending on the electrolysis conditions, as well as to fulfill the HTES of galvanic coatings by molybdenum and tungsten carbides [3, 4].

## *2. Experimental*

The steady-state and time-dependent current-voltage characteristics were obtained using a PI-50-1 pulse potentiostat. The steady-state characteristics were recorded using a DPD-4 two-coordinate recorder, while time-dependent ones were recorded using a PO-5122M polarograph. The potentials of equilibria and processes were measured with respect to platinum–oxygen reference electrode [3, 4]. The electrolysis of the NaCl–LiF–$Na_2MoO_4$–$Na_2CO_3$ and NaCl–LiF–$Na_2WO_4$–$Na_2CO_3$ melts was performed in containers made from MPG-7 grade graphite. The melt was prepared from preliminarily dried chemically pure grade NaCl and LiF and analytical grade $Na_2MoO_4$, $Na_2WO_4$, and $Na_2CO_3$. Impurities were removed from the electrolyte by electrolysis with a cathode current density of 10–15 A/dm$^2$ until a continuous precipitate was stably obtained. Cathodes were nickel, copper, and steel plates 1 × 2 cm in size.

The precipitates were investigated by X-ray diffraction and metallographic analysis. Microhardness on a transverse slice was determined using a PMT-3 device with an indenter load of 0.1 kg, the lattice parameters were measured using a DRON-3 diffractometer in $CuK_\alpha$ radiation, and the coating thickness was measured using a 2IGM multi-turn indicator; in some cases it was measured by metallographic analysis.

## *3. Result and discussion*

### *3.1 Halogenide–Oxide Melts*

Electrochemical reactions on electrodes are described in detail in [3, 4]. On the cathode, refractory metal and carbon are isolated:

$MO_4^{2-} + 6e \rightarrow M + 4O^{2-}$ (M is Mo or W),

$CO_3^{2-} + 4e \rightarrow C + 3O^{2-}$

with their subsequent interaction with the formation of oxides.

The composition of cathode products of the systems under study is presented in Table 1. The potential for the electrochemical reduction of molybdenum from the molybdate ion at the background of the NaCl–LiF melt is 0.2 V more positive than the potential for the electrochemical reduction of tungsten from the tungstate ion and almost coincides with the potential for the electrochemical reduction of carbon from the carbonate ion [3, 4]. This circumstance, as well as the existence of molybdenum carbide of the only composition $Mo_2C$, allows us to perform the conditions of crystallization of molybdenum carbide in a form of continuous precipitate. Tungsten and carbon form two carbides, WC and $W_2C$. It is impossible to crystallize WC in a form of a continuous precipitate, because WC forms at a certain excess of free carbon, which inhibits the growth of electrolytic precipitates. Therefore, in order to crystallize tungsten carbide in a form of a continuous precipitate, more careful control over the electrochemical synthesis is necessary, and it should be performed in a mode of obtaining $W_2C$ [5].

***Table 1:*** *Composition of cathode products of electrolysis of the melts NaCl–LiF(3:1 wt. fractions)–$Na_2MoO_4$–$Na_2CO_3$ and NaCl–LiF(3:1 wt. fractions)–$Na_2WO_4$–$Na_2CO_3$.*

| Content of melt components, wt. % | | | Composition and structure of the cathode precipitate |
|---|---|---|---|
| $Na_2MoO_4$ | $Na_2WO_4$ | $Na_2CO_3$ | |
| 1–15 | – | – | Mo coating |
| 15–30 | – | – | Mo–$MoO_2$ precipitate |
| – | 1–20 | – | W coating |
| – | 20–30 | – | W–$WO_2$ precipitate |
| – | – | 1–30 | C powder |
| 5 | – | 0.5–2.0 | Mo–$Mo_2C$ coating |
| 5 | – | 2–4 | $Mo_2C$ coating |
| 5 | – | 5–10 | Unadherent $Mo_2C$–C precipitate |
| – | 5 | 0.1–0.2 | W–$W_2C$ coating |
| – | 5 | 0.2–0.5 | $W_2C$ coating |
| – | 5 | 0.5–1.0 | $W_2C$–WC coating |
| – | 5 | 1.0–5.0 | WC–C powder |

*Note*: T = 1173 K; cathode is C, Ni, Cu; anode is graphite; and $i_c$ = 5.0–7.5 A/dm$^2$.

Experiments at T = 1173 K and cathode current density $i_c$ = 8 A/dm$^2$ showed that continuous molybdenum precipitates are formed at the $Na_2MoO_4$ concentration in the melt of ≤15 wt %. At a higher molybdate content, molybdenum oxides precipitate along with molybdenum. Continuous tungsten precipitates are obtained at the $Na_2WO_4$ concentration in the melt of ≤20 wt %; at its higher concentration, tungsten oxides also co-precipitates. Amorphous carbon powder isolates from the melts containing only carbonate.

To investigate the influence that other parameters (temperature, current density, and electrolysis mode) have on the properties and structure of the Mo, W, $Mo_2C$, and $W_2C$ coatings, we selected the following optimal alloys: NaCl–LiF – 5 wt % $Na_2MoO_4$ ($Na_2WO_4$), NaCl–NaF – 5 wt % $Na_2MoO_4$ – 2 wt % $Na_2CO_3$, and NaCl–LiF – 5 wt % $Na_2WO_4$ – 0.4 wt % $Na_2CO_3$. Continuous precipitates were obtained at T = 1073–1323 K. At lower temperatures, along with metal or carbide, metal oxides are precipitated. Well-adhered continuous pore-free coatings are observed at a current density of 2–15 A/dm$^2$ and deposition rate of 2–20 μm/h. The current yield of carbide coatings is 40–50%; their depth reaches 30 μm. A low current yield in the case of carbide coatings is caused by the violation of the growth front of the precipitate as a result of its passivation with lithium oxide, which is formed during the electrode reaction [3, 4]. Further, carbides are precipitated in the form of powder.

A coarse-crystalline structure of formed coatings was made finer using the reverse of the dc during the electrolysis. The ratio of durations of the cathode and anode pulses ($\tau_c/\tau_a$) varied in the limits of 30–60, the duration of the anode period was 0.5–1.5 s, and its current density was 0.15–0.50 A/dm$^2$. As a result, we succeeded in increasing the thickness of metal coatings to 200 μm and that of carbide coatings to 100 μm. The optimal parameters of the reverse mode were $\tau_c$ = 45 s, $\tau_a$ = 1.5 s, $i_c$ = 8–10 A/dm$^2$, and $i_a$ = 20–30 A/dm$^2$.

### *3.2 Oxide Melts*

In addition to halogenide–oxide carbonate-containing melts for the electrochemical deposition of molybdenum, tungsten, and their carbides, we also used oxide tungstate–molybdate–carbonate melts. The composition of cathode products in the systems under study, depending on the electrolysis conditions, is presented in Tables 2–5.

***Table 2:*** *Composition of cathode products of electrolysis of the $Na_2WO_4$–$Li_2MoO_4$–$Li_2CO_3$ melts.*

| Content of melt components, wt. % | | Composition and structure of the cathode precipitate |
|---|---|---|
| $Li_2MoO_4$ | $Li_2CO_3$ | |
| 1–10 | 1–10 | $Mo_2C$ coating |
| 2.5–5.0 | 5–10 | Unadhered C, Mo, $Mo_2C$ precipitate |
| 5–10 | 2.5–5.0 | Mo coating |
| 10–20 | 2.5–5.0 | Large $MoO_2$ crystals |
| 2.5–5.0 | 10–20 | C powder |
| – | 5–10 | WC powder |
| 5–10 | – | Mo coating |

*Note*: T = 1173 K; cathode is C, Ni, Cu; anode is graphite; and $i_c$ = 0.05–0.075 A/cm$^2$.

***Table 3:*** *Composition of cathode products of electrolysis of the $Na_2WO_4$–$MoO_3$–$Li_2CO_3$ melts*

| Content of melt components, wt. % | | Composition and structure of the cathode precipitate |
|---|---|---|
| $MoO_3$ | $Li_2CO_3$ | |
| 1–10 | 2–20 | $Mo_2C$ coating |
| 2.5–5.0 | 10–20 | Unadhered C, Mo, $Mo_2C$ precipitate |
| 5–10 | 5–10 | Mo coating |
| 10–20 | 5–10 | Large $MoO_2$ crystals |
| 2.5–5.0 | 20–40 | C powder |
| – | 5–15 | WC powder |
| 1–5 | – | Mo coating |
| 5–10 | – | Large $MoO_2$ crystals |

*Note*: T = 1173 K; cathode is C, Ni, Cu; anode is graphite; and $i_c$ = 0.05–0.075 A/cm$^2$.

***Table 4:*** *Composition of the cathode products of electrolysis of the $Na_2WO_4$–$Li_2WO_4$–$Li_2CO_3$ melts*

| Content of melt components, wt. % | | Composition and structure of the cathode precipitate |
|---|---|---|
| $Li_2WO_4$ | $Li_2CO_3$ | |
| – | 1–15 | $W_2C$ coating |
| – | 15–30 | WC coating |
| – | 30–50 | C powder |
| 10–30 | – | W coating |
| 5–10 | 5–10 | $W_2C$ coating |
| 5–10 | 10–20 | WC coating |
| 5–10 | 20–40 | C powder |

*Note*: T = 1173 K; cathode is C, Ni, Cu; anode is graphite; and $i_c$ = 0.05–0.075 A/cm$^2$.

***Table 5:*** *Composition of cathode products of electrolysis of the $Na_2WO_4$–$WO_3$–$Li_2CO_3$ melts*

| Content of melt components, wt. % | | Composition and structure of the cathode precipitate |
|---|---|---|
| $WO_3$ | $Li_2CO_3$ | |
| – | 1–15 | $W_2C$ coating |
| – | 15–30 | WC coating |
| – | 30–50 | C powder |
| 5–15 | – | W coating |
| 5–10 | 10–20 | $W_2C$ coating |
| 5–10 | 20–40 | WC coating |
| 5–10 | 40–60 | C powder |
| – | 1–15 | $W_2C$ coating |

*Note*: T = 1173 K; cathode is C, Ni, Cu; anode is graphite; and $i_c$ = 0.05–0.075 A/cm$^2$.

Coatings of molybdenum carbide are precipitated from electrolyte $Na_2WO_4$–$Li_2MoO_4$–$Li_2CO_3$ with the equality (in the limits of 2.5 mol %) of concentrations of lithium molybdate and lithium carbonate; they should not exceed 10 mol %. At lower molybdate contents in the precipitate, carbon, molybdenum, and molybdenum carbide were found in the precipitate; and at higher contents, molybdenum oxides are observed. At lower carbonate concentrations, molybdenum prevails in the precipitate, and at higher concentrations, mainly free carbon is isolated. Molybdenum oxide is a more available commercial reagent and the source of molybdenum. With its use in this role, the required amount of carbonate is approximately a factor of 2 larger than in the case of the use of lithium molybdate (see Tables 2, 3).

Continuous coatings of molybdenum carbide were obtained at T = 1073–1223 K and $i_c$ > 0.5 A/cm$^2$. At T < 1073 K and current densities higher than 0.5 A/cm$^2$, the precipitates are presented by highly dispersed powders of molybdenum carbide with a specific surface up to 30 m$^2$/h. Well-adhered, uniform, continuous, and absolutely pore-free coatings from electrolyte $Na_2WO_4$ – 5 mol % $MoO_3$ – 10 mol % $Li_2CO_3$ at T = 1173 K are observed at cathode current densities from 0.01 to 0.10 A/cm$^2$. The deposition rate of coatings in the range of ic under study is 5–25 μm/h; the current yield of molybdenum carbide reaches 80%. The maximum thickness of the coatings does not exceed 100 μm.

The use of the reverse mode of the electrolysis allowed us to make the coarse-crystalline structure finer and increase the coating thickness to 200 μm. The optimal parameters are as follows: $\tau_c/\tau_a$ = 20–40, the duration of the anodic period is 0.5–2.0 s, and the current density is 0.15–0.50 A/cm$^2$.

Coatings of tungsten carbide $W_2C$ are precipitated from electrolyte $Na_2WO_4$–$Li_2CO_3$ at $Li_2CO_3$ concentrations <15 mol %. At higher amounts of $Li_2CO_3$, coatings of tungsten carbide WC are obtained. The powder of free carbon is isolated at the $Li_2CO_3$ contents >30 mol %. In the absence of lithium carbide at concentrations of $Li_2WO_4$ >10 mol %, tungsten coatings are deposited (see Table 4).

When using tungsten oxide as the tungsten source, the observed regularities are similar. The distinction is that the region of isolation of sodium–tungsten bronzes is observed at $WO_3$ concentrations > 30 mol % (see Table 5).

The results of investigations of the composition of cathode products of chloride–fluoride molybdenum(tungsten)–carbon-containing molten systems indicate that, in order to deposit the galvanic coatings by the HTES method, the abovementioned electrolytes can be suggested. The regions of the electrochemical deposition of molybdenum, tungsten, their bronzes and carbides, and carbon are determined. The data of Tables 1–5 show that the phase composition of the products of electrolysis and characteristics of cathode precipitates are determined by the concentration of the carbon source in the melt, namely, lithium and sodium carbonates.

## *4. Conclusion*

(i) It is shown that cathode products of the electrolysis of the melts based on the eutectic mixture of sodium chloride and lithium fluoride and the melts based on sodium tungstate, in which molybdenum (VI) or tungsten (VI) oxides are dissolved, are molybdenum, tungsten, their bronzes and carbides, and carbon.

(ii) It is established that the phase composition of the products of electrolysis is determined by the carbonate concentration in the melt.

(iii) The deposition conditions of galvanic coatings of molybdenum and tungsten carbides on carbon, nickel, and copper substrates are determined.

## *5. Literature*


[1] Wilkes J.S., A short history of ionic liquids – from molten salts to neoteric solvents, Green Chem., 4, 2002, 73-80.

[2] Nishikata A., Numata H., Tsuru T., Electrochemistry of molten salt corrosion, Materials Science and Engineering: A, 146, 1991, 15-31.

[3] Malyshev V.V., Kushkov H.B., Shapoval V.I., High-Temperature Electrochemical Synthesis of Carbides, Silicides and Borides of VI-A group metals in ionic melts, J. Appl. Electrochem., 32, 2002, 573-579.

[4] Malyshev V., Gab A., Popescu A-M., Constantin V., Electroreduction of Tungsten Oxide (VI) in Molten Salts with Added Metaphosphate, Chemical Research in Chinese Universities, 29, 2013, 771-775.

[5] Malyshev V., Shakhnin D., Gab A., Gaune-Escard M., Astrelin I., Chaptes 4.9: Galvanic Coatings of Molybdenum and Tungsten Carbides from Oxide Melts: Electrodeposition and Initial Stages of Nucleation, in book: Molten Salts Chemistry and Technology, ed. by M. Gaune-Escard, G.M. Haarberg, Wiley, 2014, 303-317.